NOTE TO USERS

uOttawa

L'Université canadienne
Canada's university

FACULTÉ DES ÉTUDES SUPÉRIEURES ET POSTOCTORALES

uOttawa

L'Université canadienne
Canada's university

FACULTY OF GRADUATE AND POSDOCTORAL STUDIES

Cagri Ayranci

AUTEUR DE LA THÈSE / AUTHOR OF THESIS

M.A.Sc. (Mechanical Engineering)

GRADE / DEGREE

Department of Mechanical Engineering

FACULTÉ, ÉCOLE, DÉPARTEMENT / FACULTY, SCHOOL, DEPARTMENT

Development and Testing of a Long Gage Strain (LGS) Sensor for Concrete Structure Instrumentation

TITRE DE LA THÈSE / TITLE OF THESIS

A. Fahim

DIRECTEUR (DIRECTRICE) DE LA THÈSE / THESIS SUPERVISOR

M. Munro

CO-DIRECTEUR (CO-DIRECTRICE) DE LA THÈSE / THESIS CO-SUPERVISOR

EXAMINATEURS (EXAMINATRICES) DE LA THÈSE / THESIS EXAMINERS

N.J. Gardner

F. Robitaille

Gary W. Slater

Le Doyen de la Faculté des études supérieures et postdoctorales / Dean of the Faculty of Graduate and Postdoctoral Studies

Development and Testing of a Long Gage Strain (LGS) Sensor for Concrete Structure Instrumentation

Cagri Ayranci

A thesis report submitted to the Faculty of Graduate and Postdoctoral Studies in partial fulfillment of the requirements for the degree of

MASTER OF APPLIED SCIENCE

in Mechanical Engineering

Ottawa-Carleton Institute for Mechanical and Aerospace Engineering
University of Ottawa
Ottawa, Canada

March 2005

Your file Votre référence
ISBN: 0-494-11210-7
Our file Notre référence
ISBN: 0-494-11210-7

Abstract

Reinforced Concrete (RC) is the most commonly used structural material in civil engineering applications. RC structures have long term service lives under normal loading conditions; however, overload due to misuse or statistically remote events such as earthquakes may create damages that, if not detected on time, may eventually cause failure. Hence, it is important to monitor RC structures to take necessary precautions and save human lives. A Long Gage Strain (LGS) sensor has been developed to monitor these structures. While it has been developed with concrete applications in mind, the new sensor can be used in a variety of applications, including measuring strains in pipelines, steel structures, and the like. The proposed sensor system has very low cost compared to the commercially available competing systems. Prototypes of the proposed strain sensors have been built and tested to calibrate the sensors and to prove their accuracy, repeatability, and to assess their reliability prior to in-situ concrete experiments. In-situ tests of the proposed sensors embedded into a reinforced concrete beam have been carried out. The steel rebars in the beam are also instrumented with commercial short gage length strain gages in order to compare the strain outputs of the strain gages to that of the proposed strain sensor. Results prove the accuracy, and reliability of the proposed strain sensor.

Acknowledgments

This thesis is a result of countless hours of work, dedication and support. It was a long but enjoyable journey, and I would like the following people know my sincere appreciations for their contributions to the completion of this thesis:

To my primary supervisor, Dr. Atef E. F. Fahim, for sharing his knowledge and experience, and making a difference in my viewpoint of engineering; to my co-supervisor, Dr. Michael B. Munro, for his guidance and time. Dear Dr. Fahim and Dr. Munro, I was very fortunate to work with such great researchers and supervisors. Thank you.

To Léo Denner, Brent Cotter, Michael Burns , James McDermid, and Muslim Majeed for their technical support.

To my mother, Dr. Guler Ayranci; my father, Dr. Erol Ayranci; my brother, Korhan Ayranci; my sister, Inci Ayranci; and my girlfriend, Stéphanie Trottier for their unlimited support. I couldn't have finished this thesis without you.

To Kris Ewen, for helping me get through the long hours spent in the lab by putting a smile on my face.

To Togay Ozbakkaloglu, for his help in the concrete laboratory of Civil Engineering, and his time for my questions.

To the Mechanical Engineering Department of the University of Ottawa, for their financial support through Teaching Assistantship.

AFRODIT

Table of Contents

List of Figures

List of Tables

Acronyms

RC	Reinforced Concrete
LGS Sensor	Long Gage Strain Sensor
UTS	Ultimate Tensile Strength
YS	Yield Strength
CW	Cold Working
ESG	Electrical Strain Gage
LVDT	Linear Variable Differential Transformer
VWG	Vibrating Wire Strain Gage
GRP	Glass Reinforced Polymer
CB	Carbon Black
KA1	Kanthal-1 alloy
FRP	Fiber Reinforced Polymer
AWG	American Wire Gage
R^2	Coefficient of Determination (Correlation Coefficient)

Nomenclature

Symbol	*Definition*
E	Elastic Modulus
σ	Stress
ϵ	Strain
$\epsilon_{x,y,z}$	Strain on x, y, and z axis
ϵ_L	Longitudinal strain
υ	Poisson's Ratio
A_0	Original cross-sectional area
A_d	Deformed cross-sectional area
V	Voltage
V_0	Output voltage
V_s	Source voltage
R	Resistance
I	Current
ρ	Resistivity
L	Length
A	Cross-sectional area
m	mass of an electron
υ_0	Average magnitude of velocity of electrons in their random motion between ions within a conductor
n	Number of conduction electrons available per unit volume
e	Electron charge
λ	Average distance traveled by an electron between collisions, with the ions within the conductor
N_0	Total number of conduction electrons
G	Gage factor

1. INTRODUCTION

Reinforced concrete is the most commonly used structural material in civil engineering applications. Concrete has very high compressive load carrying capacity; however, its capacity to carry tensile loads is low. Consequently, concrete is commonly reinforced with steel rebars so as to carry the tensile forces that develop in structures. In the designs of concrete structures, reinforcements are located in the regions that are more likely to develop tensile forces. Limited use of reinforcements decrease the cost of these structures, because rebars are more expensive compared to concrete. During their life cycles, structures may be subjected to loads close to, or exceeding, those for which they are designed. These loads may cause structures to lose their integrity. They may even create damages that, if not detected on time, may eventually cause failure; therefore, it is very important to be able to monitor structures. Being able to assess the integrity of structures helps to take necessary precautions and save human lives.

1.1 Problem Definition

Reinforced concrete structures are very durable, and if reinforcing rebars are protected against corrosion, they have long term service lives under normal service conditions. In the absence of corrosion, concrete structures are expected to last decades without major repairs, provided that they are not subjected to very high or unexpected loads. Structures are generally designed for a given working load, and provisions for factors of safety are commonly taken into account. These working loads are calculated for the intended use of the structure and the most commonly expected conditions for which the structure is to be subjected. The factors of safety are intended to guard against variability in material characteristics, construction care, probability of abuse, and unexpected conditions to which the structure is subjected. It is unrealistic to expect a designer to account for all misuses of a structure or conditions that the structure may be subjected to, however remote. For a dramatic example one might consider the results of an earthquake where design loads may be exceeded. Overload of structures may result in damage which may or may not be visible. It is very hazardous to continue to use a damaged structure since it is very difficult to predict the magnitude of the damage after such loadings. Reinforced concrete structures are very costly to demolish and re-build; therefore, it is very crucial to have

information about the integrity of these structures using non-destructive methods during their service lives.

The best approach to get information about the integrity of these structures is to monitor the stresses on the members; however, measuring stresses in such structures is not a practical approach, instead it is preferred to measure the strains on the members. Assessing the condition of structures without any need for destructive analyses can be accomplished by measuring the strains applied on a member and converting them to stresses, providing the elastic constants of the materials used in the design are known.

Several strain measuring systems are used in commercial reinforced concrete applications. Each of these have limitations which have affect the widespread use of strain measurements in commercial applications. Among these shortcomings are: very short gage lengths for useful strain measurements, prohibitly expensive equipment costs, and, in addition, all of these systems require very delicate handling while being embedded into the concrete structures.

1.2 Proposed System

The proposed strain measuring system fulfills a need not covered by the majority of the commercially available systems. The majority of strain measuring systems are only suitable for short gage measurements. Measurements of strain in concrete structures require a sensor with a long gage length. The proposed system is developed as an alternative to the few available long gage strain measuring systems that are commercially available. While it has been developed with concrete applications in mind, the new system can be used in a variety of applications, including measuring strains in pipelines, steel structures, and the like.

The proposed system has a very low cost compared to the commercially available competing systems. It is designed and built so as to be able to measure strains at a multitude of locations along the structural element in which it is deployed. The measuring sensor of the proposed system is embedded in a rugged carrier in order to survive the rough handling inherent to concrete construction.

Prototypes of the proposed strain gages have been built and tested to calibrate the strain sensors, to demonstrate their accuracy, repeatability, and to assess their reliability prior to in-situ concrete experiments.

In-situ tests of the proposed system embedded into a reinforced concrete beam have also been carried out. The rebars in the beam were also instrumented with commercial short gage length electrical resistance strain gages in order to compare the strain outputs of the strain gages to that of the proposed strain sensor. Results obtained demonstrate the accuracy, reliability, and the repeatability of the proposed strain sensor.

1.3 Thesis Outline

In Chapter 2 a literature review of stress-strain behavior of common materials, failure modes of reinforced concrete structures, and available strain measuring techniques is presented. The first section of Chapter 3 presents the theoretical background on which the proposed strain measuring system is based. The second section of Chapter 3 presents the design procedure of the system. Chapter 4 reports the results and discussions of the tests conducted for the characterization of the strain measuring alloy used for the system. In Chapter 5, the results and discussions related to the experiments of the prototype of the proposed system are presented. This study is conducted to prove the accuracy of the proposed system and to determine the gage factor of the new strain sensor. Chapter 6 consists of the results and discussions related to the in-situ concrete beam test using the proposed strain sensors. The results of the proposed strain sensors are compared to the results of commercial short-gage strain gages that are embedded on the rebars of the same beam. The thesis ends by conclusions and recommendations for future studies. These are presented in Chapter 7.

Chapter 2: Literature Review

This chapter presents the literature review that has been conducted for the thesis. The first section presents stress-strain behavior of the metals. The second section outlines a review of reinforced concrete structures. The third section explains the importance of strain measurements in these structures. The last section presents the available strain measuring techniques.

2.1 Stress-Strain [adapted partially from [1]]

Although the following chapters are well known, they are presented here for clarity and completeness.

In this section, theoretical information about general stress and strain behaviours of metals are presented. In addition, general mechanical properties of materials and basic definitions related to these properties that are frequently referred in the following chapters are included.

As a broad definition, engineering stress is defined as the quotient of the applied force on a material by the initial non-deformed cross-sectional area normal to the direction of that applied force. True stress, on the other hand, is obtained by dividing the applied stress by the instantaneous cross-sectional area.

Upon application of load, materials deform or elongate, as a response to the imposed stress. Engineering strain is defined based on this phenomenum as the deformation divided by the original length.

If the load that causes the strain on a material is removed, two types of deformation may be observed. The first type is called elastic deformation. A deformation is defined elastic if upon removal of load, complete recovery of the material to its original shape is observed. Elastic deformation is non-permanent. The second type is called plastic deformation. This takes place if the material does not recover to its original dimensions upon removal of load. Plastic deformation is permanent. It should be noted that plastically deformed materials may still show small amounts of recovery but it is not a complete recovery

The materials that can experience large amounts of plastic deformations are defined as ductile materials. On the other hand, some of the materials experience little or no plastic

deformation and fail immediately after a certain amount of elastic deformation. These materials are defined as brittle materials. In Figure 2.1, schematic representation of ductile and brittle materials, and their elastic and plastic deformation zones are presented on a stress-strain curve.

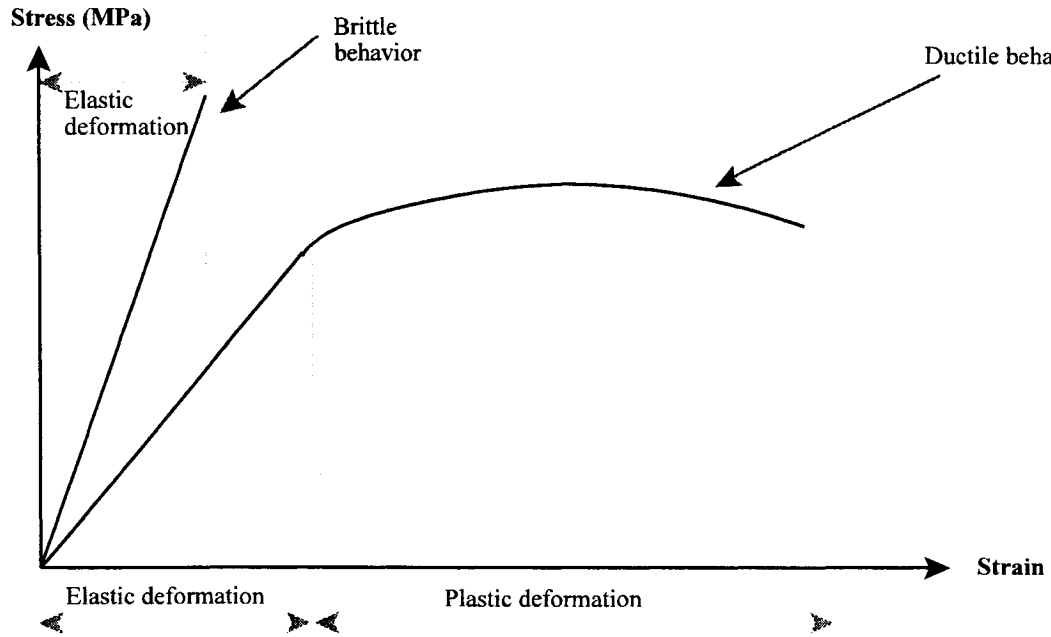

Figure 2.1: Schematic representation of stress strain curves for ductile and brittle materials.

The stress-strain curves of most metals exhibit a linear relationship within the elastic region. The slope of the straight line that is a result of this linear relationship defines the Elastic Modulus (E), or Young's Modulus, of a material. It is mathematically represented using the Hooke's Law as;

$$E = \frac{\sigma}{\varepsilon} \quad \text{.....(2.1)}$$

where σ is the engineering stress and ϵ is the engineering strain.

At the microstructural level, elastic modulus represents the resistance of interatomic bonding forces against deformation.

Another necessary concept that is referred to later in the thesis is Poisson's ratio. When a material is elastically deformed, its original shape is non-permanently changed in all three axis. The strains on different axes, z being the axis of application of the load, are related with a ratio called Poisson's ratio, ν;

$$\nu = -\frac{\varepsilon_x}{\varepsilon_z} = -\frac{\varepsilon_y}{\varepsilon_z} \quad \text{.....(2.2)}$$

For most metals, the Yield Strength (Y.S.) is defined as the engineering stress corresponding to the upper limit of the elastic behavior. In some materials, such as steel, a clearly defined yield point is observed, whereas in other materials a gradual deviation from the linear portion of the graph is observed.

Some materials, on the other hand, have a non-linear elastic region and the yield point of these materials are determined by the amount of strain before going into the plastic region.

For ductile materials, further loading following the yield strength eventually brings the material to a maximum loading point that is called the Ultimate Tensile Strength, UTS. Up to the UTS, materials experience elastic deformation that is followed by a plastic deformation. In both cases the deformation is accepted to be a uniform one; however, a non-uniform thinning (necking) of the cross-section is observed after the UTS. This non-uniform thinning region continue to get thinner as the material elongates and eventually fracture occurs at the necked region.

Strain hardening, or cold working, is the process of increasing the Y.S. and UTS of a ductile material by plastically deforming it. At the micromolecular level, increasing the amount of plastic deformation increases the number of dislocations existing in the material. As the number of dislocations increase, the strength of a material increases, since these dislocations blunt the ability of atomic planes to slide relative to each other. The degree of cold working that a material is subjected to is calculated by;

$$\%CW = \frac{A_0 - A_d}{A_0} \times 100 \quad \text{.....(2.3)}$$

where A_0 and A_d are the original and deformed cross-sectional areas, respectively.

Even though the strength values of an originally ductile material is enhanced by the amount of percent cold working, the ductility of the material is lost and it becomes more brittle.

2.2 Reinforced Concrete

Reinforced concrete is predominantly used in structural applications. The concrete, on its own, has very high compressive load carrying capacity; however, its tensile load carrying capacity is very low. A non-reinforced concrete structure fails rapidly and without warning, under tensile or flexural load. Reinforced concrete structures are composed of many components such as beams, columns, slabs, and the like. All of these components, depending on their design purpose, are subjected to a variety of loads. These loads can be decomposed to compressive or tensile forces applied to different cross-sections of the analyzed component. One example is the design principle of balconies in structures. When a load is applied to the top face of the balcony, the balcony is modeled as a cantilever. The deflection creates compressive forces on the bottom face, and tensile forces on the top face; therefore, balconies are reinforced close to the top face. Since concrete is capable of carrying only compressive forces, reinforcements compensate for the lack of tensile force carrying capacity of concrete. It should be mentioned that the high tensile force carrying ability of steel rebars comes with the disadvantage of high cost; therefore, designers optimize the usage of rebars in structures. Since the comparably very low cost concrete is capable of carrying compressive forces, the rebars are only used to carry tensile forces to decrease the cost of structures.

There are many types of steels that are used as rebar materials. Most steel rebars experience yielding at approximately 0.002 strain at about 450 MPa stress, ultimate tensile strength at approximately 600 MPa. Although, there are many types of concretes used in structures, it is usually assumed that the limiting compressive strain of concrete is 0.003ϵ, the limiting tensile strain of concrete is $100\mu\epsilon$, and the 28-day compressive strength of concrete is 35 MPa for design purposes.

In Figure 2.2 [2], the compressive and tensile forces that develop in a concrete beam are represented. In this representation the beam is simply supported and two point loading is used. If the beam is a non-reinforced beam, a tension-compression couple forms that is due to the internal moments about point A as is shown in Figure 2.2(b). Since concrete can not resist the high tensile forces, this beam is prone to a catastrophic failure without any warning. Use of reinforcing rebars are required to avoid this undesired failure. Reinforcements are embedded into

concrete in such a way that tensile forces in structures are assumed to be almost exclusively carried by reinforcements instead of concrete. The development of tensile forces in the reinforcements due to the flexural load applied to a reinforced concrete beam is represented schematically in Figure 2.2©). In this diagram, the concrete is carrying the compressive forces on the top part of the beam, and the reinforcements are balancing the tensile forces. The beam in this figure is expected to give pre-failure warning in the form of visible cracks on the underside due to the relatively low ductility of the concrete compared to the steel reinforcements.

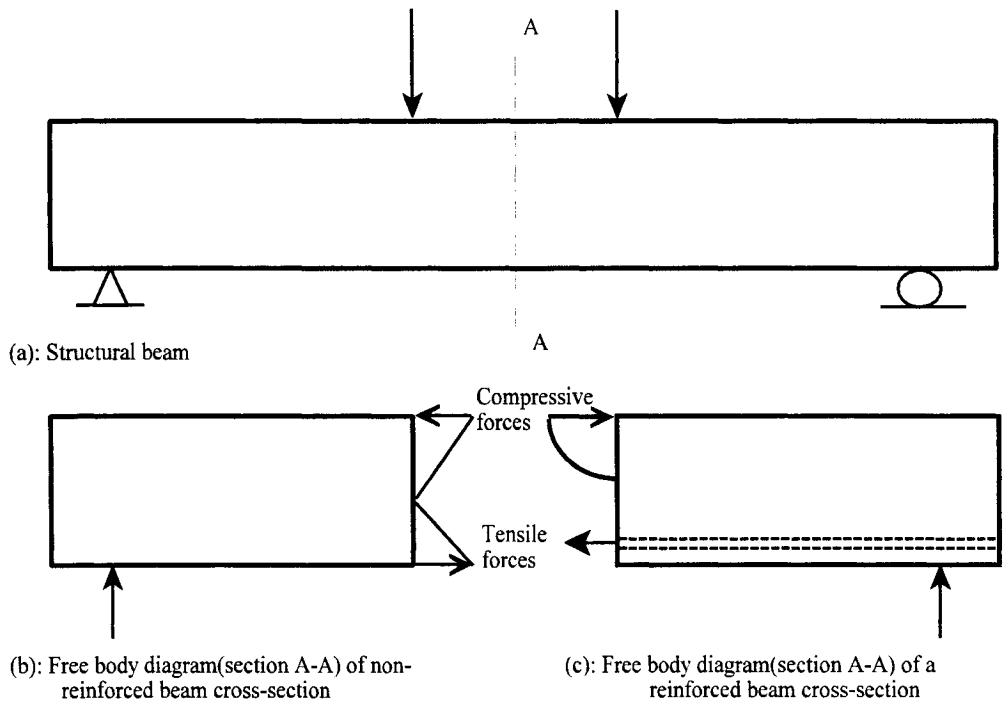

Figure 2.2: Schematic representation of a structural beam [2].

The current reinforced concrete design procedures assume that structures fail in one of three failure modes [2, and 3]. The first mode is "Tension Failure". This failure happens when reinforcement in concrete fails before the concrete crushes. Such a structure is called under-

reinforced. The second mode of failure happens when the concrete reaches its limiting compressive strain before the reinforcement failure, i.e. "Crushing Failure". Such a structure is called over-reinforced. The third mode is when the crushing of concrete and failure of reinforcement occurs simultaneously. This mode of failure is called "Balanced Failure".

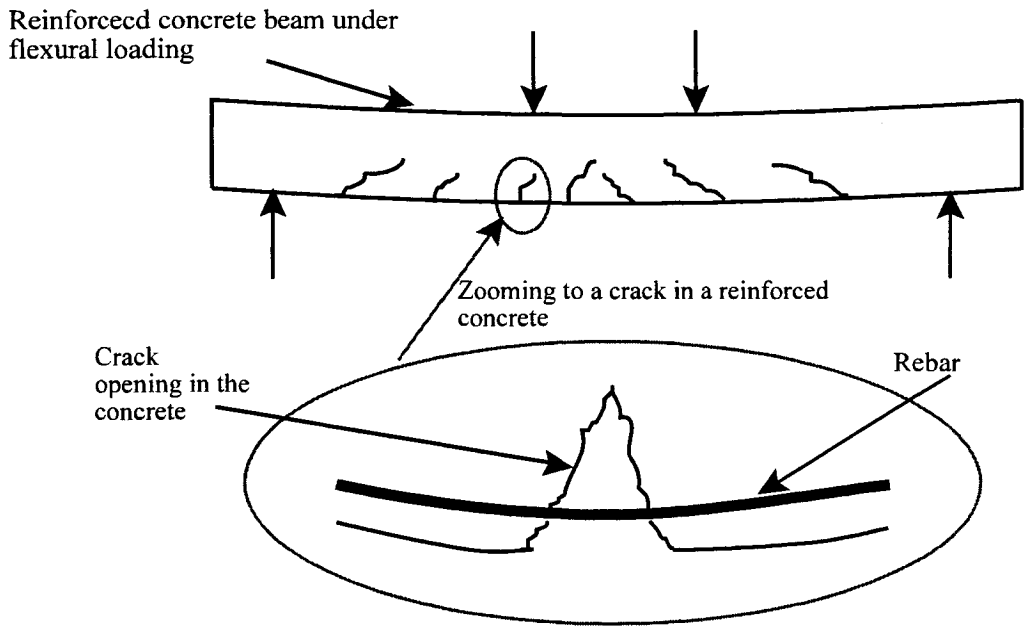

Figure 2.3: Cracks in a reinforced concrete beam under flexural loading.

Under-reinforced structures experience large deflections which result in cracking of the concrete. This is schematically represented in Figure 2.3. Structures with such designs fail in a ductile manner due to the yielding of the rebars. This failure mode is the preferred one since it provides a visible warning prior to structure collapse. On the other hand, both balanced failure and over-reinforced failure occur without pre-warning and in a brittle manner. Schematic representation of ductile and brittle failures, in terms of load versus deflection of structures, are shown in Figure 2.4. Most of today's structures are designed to provide under-reinforced mode of failure in order to benefit from the pre-failure warnings that can save human lives [4, and 5].

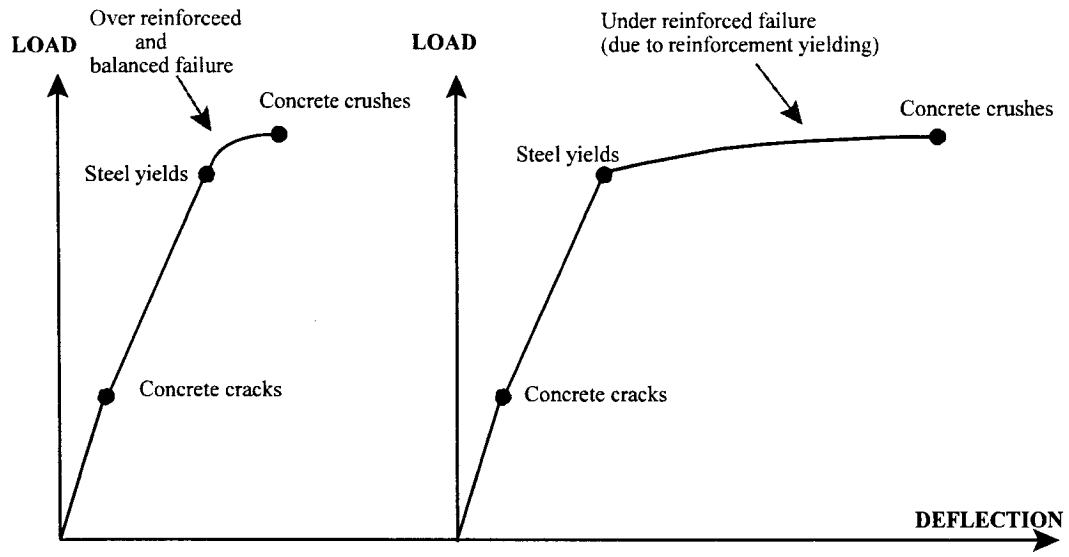

Figure 2.4: schematic representation of different types of failures on load versus deflection graph [2, and 4].

2.3 Strain Measurements in Reinforced Concrete Structures

The importance of designing under-reinforced concrete structures has been outlined in the previous sections. In such structures, after the cracking of the concrete, the tensile force on the particular section is transferred almost entirely to the reinforcements. At a crack, the bonding between the concrete and the reinforcement is lost. The particular section of the reinforcement that is not-bonded to the concrete starts to carry the entire tensile force with no contribution from the concrete. This results in an increase in the local strain as a result of the increased tensile stress. This would eventually cause the yielding of the rebars and finally the structure fails.

The cracks that occurred prior to the yielding of the rebars may or may not be visibly detectable. Although it is possible to visually detect major cracks, some failure points may go undetected. It is also possible that some structures do not allow for visual inspections due to

their design. For this reason, periodical monitoring of strain in structures using appropriate instrumentation is becoming increasingly crucial.

Monitoring the behaviour of structures under different loading conditions during their life spans is called Health Monitoring. The structures that are equipped with instruments that allow one to monitor their integrity are called Passive Smart Structures [6].

As a result of a previous discussion it was concluded that strain is the easiest and one of the most important properties that needs to be monitored in reinforced concrete structures. The general integrity of concrete structures has a direct relationship with the magnitudes of strains that they experience. Strain monitoring can provide early warnings for non-safe structures, and early warnings for necessary evacuations. At the same time, collected strain data can be used to regulate loadings. Such regulations can be used on a bridge or a dam to avoid dangerous loadings. The need to monitor these structures can also be understood by considering the effects of unexpectedly high magnitude loadings, such as during earthquakes. The ability to monitor the strains on damaged structures after earthquakes helps to assess the condition of the structures and save lives of crews that are sent in/on these structures.

2.4 Strain Measuring Techniques

In this section, techniques that are commonly used in commercial strain measuring applications are outlined. For completeness purposes, this is followed by the techniques that are not commercially used but that are listed in the academic literature.

While strains are measured in a variety of ways, the commonly used methods are Electrical (resistance) Strain Gages (ESG), Linear Variable Differential Transformers (LVDT), Vibrating wire strain gages (VWG), and fibre optic strain gages. Other strain measuring systems are the ones that have been developed but are not used in civil engineering health monitoring applications due to their specific limitations.

2.4.1 Commercially Available Strain Measuring Techniques:

2.4.1.1 Electrical Resistance Strain Gages

Electrical resistance strain gages (ESG) are one of the most widely used strain measuring sensors. An ESG is composed of an elastic carrier and a resistor [7]. The resistors are either composed of small diameter wire or etched layers on a metal foil as shown in Figure 2.5. In metal-foil type strain gages, the grid configuration is formed by a photo etching or mechanical cutting [7, and 8].

The resistor is permanently bonded on to the carrier, and the carrier is bonded to the object at the location where the strain is to be measured. Strain induced in the object cause a strain in the resistance wire and a corresponding change in its length and diameter. This in turn causes a change in resistance proportional to the strain.

Due to the physical properties of ESG sensors, very delicate handling is required for accurate results. The carrier or the grid is easily damaged or torn and has to be protected at all times before and after bonding to the structure.

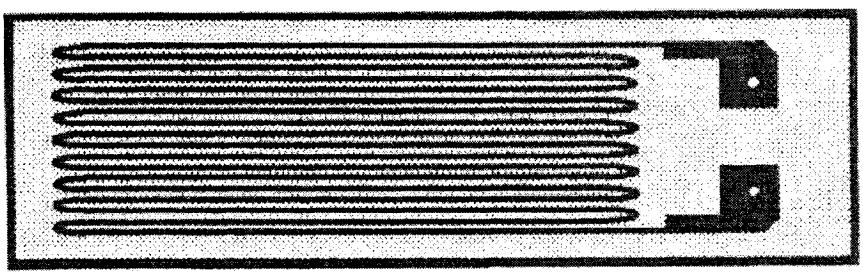

Figure 2.5: Bonded strain gage [adopted from [7]].

Electrical strain gages typically have very short gage lengths. Although a wide variety of gage lengths are available for commercial applications, most commonly used ones have gage lengths varying form 1mm to 10mm. It should be mentioned that as low as 0.2 mm and as high as 100 mm gage lengths are available for special applications. Generally speaking, strain measuring ranges for ESGs are approximately 1200 to 3000 microstrains [9]. As a result of their short gage lengths, the measurements conducted using ESG sensors are limited only to local

strain measurements. Monitoring the overall strain integrity of a structure is impractical with short gage ESG sensors, because it is impossible to predetermine a priori the location of initiation of a crack in order to instrument this location. As described in Section 2.2 and Section 2.3, a crack causes an increase in the loads that are carried by the reinforcements. This is because a crack causes loss of bonding between the concrete and reinforcement, and when this bond is lost the contribution of concrete to carry the load on the element is stopped and the entire load is now transferred to the reinforcements in the structure. If the sensor has a short gage length and the crack does not occur where the sensor is located (i.e. if the sensor is located at a section that does not experience cracking of concrete), the sensor does not measure the critical strain that takes place at the crack.

An extensometer is a commonly used device for measuring strain in various applications. It is composed of a strain gage attached to a cantilever beam. The extensometer is attached to the element of which strain is measured. As the element is loaded the cantilever beam is deflected and this deflection is detected via the ESG sensor which is proportional to the strain of the element. Since an extensometer basically uses an ESG, it is listed under this section and not as a separate section in the thesis.

2.4.1.2 Linear variable differential transformers (LVDTs)

LVDT sensors are displacement measuring devices where the position is deduced from the magnitude of the electromagnetic wave induced into the LVDT secondary coils.

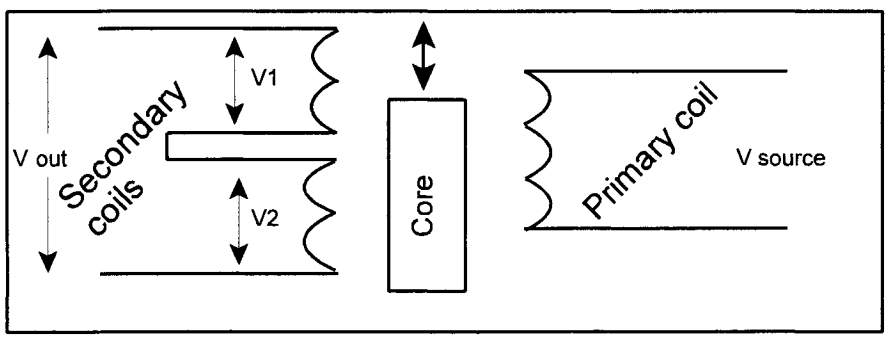

Figure 2.6: Circuit diagram of an LVDT [[7], and [8]].

A circuit diagram of a general LVDT is shown in Figure 2.6. An LVDT has one primary and two secondary coils on an insulated cylinder and a core that couples the primary and secondary coils. The primary coil carries an excitation voltage. This excitation voltage induce ac voltages in the secondary coils. As the core moves through the coil, an output voltage Vo, Vo = V2-V1, is measured as a linear function of the position of the core. This is due to the opposing phases of the flux coupling between the secondary coils. The degree of flux coupling has a linear relationship with the axial position of the core [7, and 8].

LVDT sensors are not used as internal strain measuring devices for structural concrete applications. In case of a flexural loading, the alignment of the core with respect to the coils can not be maintained due to the curved shape of the deflected beam. LVDT's are generally used in laboratory settings to measure the external deflections of concrete elements.

2.4.1.3 Vibrating Wire Strain Gages (VWG)

With reference to Figure 2.7, a vibrating wire strain gage (VWG) is composed of a thin wire of approximately 0.25mm diameter that is stretched over a predetermined distance. An electromagnetic hammer can be actuated to pluck the wire causing it to vibrate [10, 11, and 12]. The frequency of vibration is proxy to the tension in the wire, and hence elongation. They can either be embedded inside the concrete element, or attached to the surface of the element afterwards. As the structure is loaded, the distance between the anchored ends increase or decrease causing a change in the tension of the wire which leads to a change in the natural frequency of vibration of wire. [10, 11, and 12].

Concrete is a non-homogeneous material, and VWG measures the average strain in concrete; therefore, the ratio of maximum aggregate size to gage length of the vibrating wire strain gages is an important aspect that determines the accuracy of the measurements [10].

Vibrating wire strain gages are reported to be very sensitive to temperature as a temperature change of 1°C may cause 20 micro-strain difference in strain measurements [11]. Most of the commercially available VWG sensors are reported to have an approximately 3000 microstrain measuring range with a resolution of approximately 1 microstrain [12, and 13].

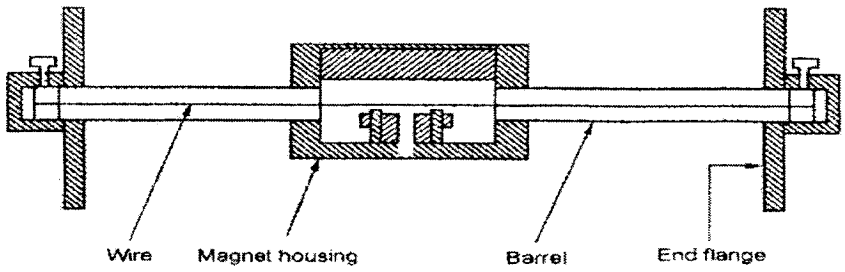

Figure 2.7: Schematic representation of an embedment type VWG [10].

2.4.1.4 Fiber Optic Strain Sensors

Fibre optic cables are commonly used in strain measurements, both in commercial and experimental applications. Despite their advantages, the very high costs of the equipment (average of hundreds of thousand dollars and above) limit their broader use. Generally, fibre optic sensors are grouped into two types; namely, the Fabry Perot Sensors, and the Bragg Grating Sensors.

2.4.1.4.1 Fabry Perot Sensors

Fabry Perot Sensors use a broadband light source. Figure 2.8 shows a schematic representation of a Fabry Perot Sensor. Fabry Perot Sensors are composed of two fibers fused into a capillary tube (200 to 250 micrometer in diameter). The distance between the fused locations defines the gage length of the sensor, and the strain is measured by the phase difference of reflected and transmitted light caused by the change of the air gap length in the capillary tube. They have a gage length of approximately 8 mm. The strain range of this type of fibre optic strain sensors are reported to be approximately ±5000microstrain or 0-10000microstrains [6, and 14].

The Fabry Perot Sensors suffer from the short gage length problem that is described in the previous sections, especially in the section regarding the ESG sensors; therefore, it is crucial to very accurately determine the location that needs to be monitored in order to use these sensors.

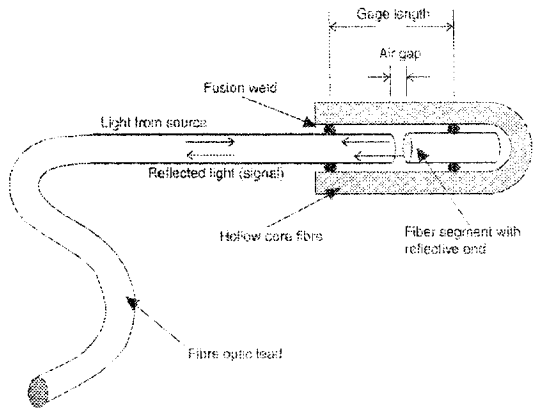

Figure 2.8: Schematic representation of Fabry Perot fiber optic sensor [6].

2.4.1.4.2 Bragg Grating Sensors

With reference to Figure 2.9, Bragg Grating Sensors usually have ±5000 microstrain range. Grating, an optical filter [15], reflects the sent broadband light with a different wavelength. As the length of the fibre changes due to tension or compression, the refractive index of the grating changes and the wavelength of the light that is reflected is used to determine the strain on the sensor [16, and 17]. These types of sensors usually have very short, 1 to 20 mm, gage lengths. The strain measurements conducted with these sensors can be inaccurate if the location of the sensor is not correctly determined. To overcome this problem two new techniques have been reported; the first one is the Multiplexing, or quasi-distributed, fiber Bragg grating sensors and the second one is the long gage fibre optic Bragg grating strain sensors [15, 16, and 18].

The multiplexing technique allows taking multiple strain measurements from different points on the same Bragg grating fiber optic which enables the user to measure more than one point on the structure [15, and 17]. Another solution to the problem is to use long-gage fiber optic Bragg Grating sensors. These sensors can increase the gage lengths up to metres [16, 18,

and 19]. These type of sensors allow measuring the overall average displacement of the structure to which the sensor is attached. Long gage sensors are utilized to determine the curvatures of structures. The horizontal and vertical displacements are then calculated using the curvatures [19].

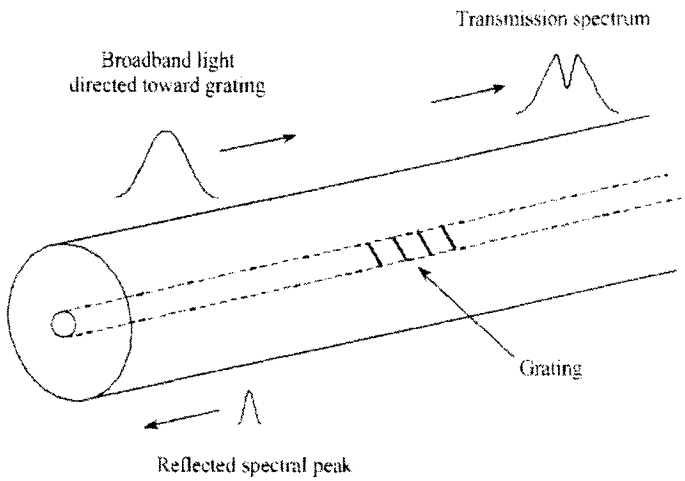

Figure 2.9: Schematic representation of a Fibre Bragg grating sensor [16].

2.4.2 Strain Measuring Techniques Listed in the Academic Literature

Strain measuring methods that are listed in this section are either in the process of development or due to their incompatibilities they are not used in commercial structural concrete applications.

2.4.2.1 Brillouin Scattering Technique

This strain measuring technique utilizes the phenomenon known as Brillouin scattering in a fiber optic cable. Brillouin scattering phenomenon is reported to be caused by fluctuations in the refractive index of the material. Due to the change in the refractive index, some of the light that is sent from the source reflects back to the source but with a shift in the frequency, that is called a Brillouin shift. This shift is found in the literature to have linear relation to the strain. Although not many applications are reported in the literature, the major advantage of this

method is the unlimited number of measurement points using a single optical fibre. Despite its advantages, the disadvantages should be listed as its cost and weak Brillouin signal that needs to be amplified to use the data during measurements [20, 21, 22, and 23]. In addition, this system is still in development and does not have listed commercial applications.

2.4.2.2 Using the In-situ Resistance of Material for Strain Measurements

Some researchers, [24, and 25], proposed using resistance of the material itself for strain measurements. This technique has applications mostly for the longitudinal unidirectional composites and it utilizes one of the basic physical properties of the materials, i.e. piezoresistive effect. The basic principle is to measure the resistance change along a material after application of a certain amount of load (i.e. leads to strain or elongation).

This method is generally used for carbon or glass composites. Although carbon is a conductive material, glass reinforced plastics (GRP) are non-conductive materials. The GRP composites are converted to conductive materials by adding carbon black (CB) fillers into their matrix. This makes it possible to monitor the strain through resistance change.

Use of this method helps to determine when the material fails due to the loss of contribution of broken fibers to resistance measurement. It is not, however, very practical to calibrate the material to determine the strain by using this method.

Since this method does not give repeatable results for every type of material, it can be considered to work with only a few materials and should not be generalized as a common strain measuring technique.

2.4.2.3 Magnetic Wire Strain Gages

Another reported experimental technique for measuring strain is called the Magnetic Wire Strain Gage. This strain gage is composed of a small diameter copper wire coated with a magnetic film that dominates the wire's impedance and is sensitive to strain. It is reported that a wave driving current produces "spikes" in the output waveform, and as the sensor is strained the magnitude of the strain is determined utilizing the decreasing magnitudes of the spikes. It is possible to create a linear array of multiple sensors by multiple deposition of magnetic

material on the same wire. Although possibility of usage for integrity of structures (such as bridges) is mentioned, only results for monitoring the strains during curing of composite structures is reported using this technique [26].

An alternative sensor, the LGS sensor, is introduced in the next chapter.

Chapter 3: Introduction and Design of the Proposed Strain Measuring System

The proposed strain measuring system, Long Gage Strain (LGS) measuring system, is designed as an alternative to those currently used for the health monitoring of structures. The system is inexpensive, has a long and incrementally adjustable gage length, and provides accurate and repeatable results. The system is configured to have multiple strain sensors on a single carrier to monitor the integrity of a long structural element.

In its simplest configuration, the proposed strain gage is created by embedding a high resistance wire with multiple taps into a carrier. As the carrier stretches, the embedded wire stretches. The change in the length and diameter of the wire creates a resistance difference. This difference is measured and converted to strain using a calibration relationship.

Low resistivity copper wire is soldered at equal distances on to the high resistance wire along its length. Figure 3.1 shows a schematic diagram of a strain sensing wire that is segmented into three. This wire is then required to be embedded into the middle of its carrier (as in a pultrusion process). The desired final product is shown in Figure 3.2. Since the carrier is purchased for this study, embedding process is different than the one shown. The details are presented later in the thesis. When embedded into a concrete structure, and as the structure is loaded, different segments of the sensor experience different strains. These strains are in turn measured as a change in resistance of the corresponding segment.

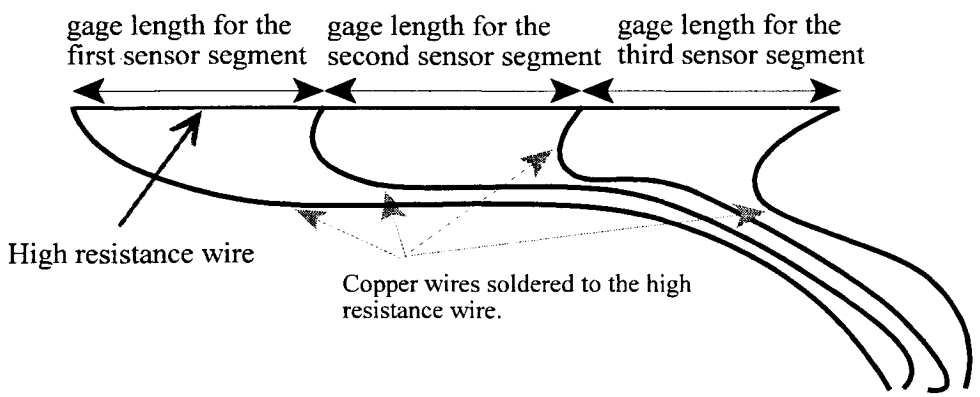

Figure 3.1: Schematic design of the proposed multiple segment strain measuring sensor.

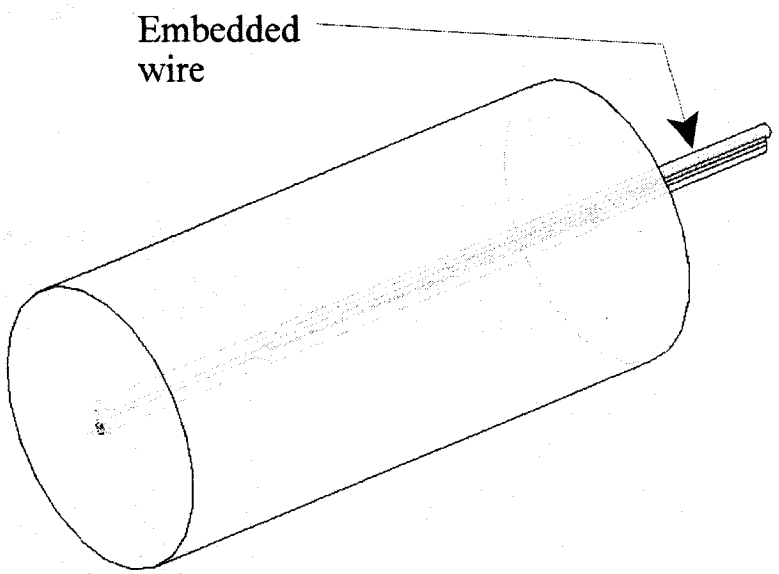

Figure 3.2: Schematic diagram of a carrier and a three segment strain sensor.

In this chapter the theoretical background and the actual design process of the proposed sensor system is presented. The first part of the discussion includes the explanation of important concepts for the proposed strain sensor, and calculation of strain through the resistance change in a wire. This is followed by a brief theory of the measurement of resistance. In the second part, the actual design process of the sensor system is outlined.

3.1 Important Concepts for the Proposed System

Although the following concepts are well known, they are presented here for clarity and completeness purposes.

3.1.1 Resistance

Resistance is the opposition of a material to the electric current passing through the material. [27, and 28]. The electric resistance of a material is defined by Ohm's Law:

$R = V/I$ where R, V, and I are; resistance, applied voltage, and the current passing through the resistor, respectively.

Another formula to define the resistance of a wire is using its length, cross-sectional area, and its resistivity is presented in Equation (3.1) [8];

$$R = \rho \times \frac{L}{A} \quad \text{.....(3.1)}$$

where ρ is the resistivity, L is the length, and A is the cross-sectional area of the specimen being investigated.

The resistivity of a material is defined as the specific resistance of a material that has a 1m length and a $1m^2$ cross section. It is measured at a standard temperature and carry the SI units of ohm-meter. The resistivity of a material is given by the formula [29,30, and 31];

$$\rho = \frac{2mv_o AL}{N_o e^2 \lambda} \quad \text{.....(3.2)}$$

where m is the mass of electrons, N_o is number of total electrons in a volume, v_0 is the average magnitude of the velocity of the electrons, e^2 is the electron charge, λ is average distance traveled, A is the area and L is the length of the atom.

The resistance of a wire changes when it is subjected to changes in its length, cross-section and temperature, i.e. resistance is strain and temperature sensitive. The resistance change as a result of the strain on the material is called the piezoresistive effect.

A change in the dimensions of a wire, i.e applied strain, creates a resistance change in the wire. This is formulated by differentiating Equation 3.1 and dividing by R gives;

$$\frac{dR}{R} = \frac{d\rho}{\rho} + \frac{dL}{L} - \frac{dA}{A} \quad \text{.....(3.3)}$$

The last equation can be simplified to;

$$\frac{dR}{R} = \frac{d\rho}{\rho} + \frac{dL}{L}(1 + 2\nu) \quad \text{.....(3.4)}$$

where ν is Poissons' ratio.

Equation 3.4 can be re-written to define a fundamental constant used in the Electrical Strain Gages (ESG) known as the "gage factor", G. Most metals have gage factors ranging from 2 to 4. This will be investigated further in this chapter.

$$G = \frac{dR/R}{\varepsilon} = \frac{d\rho/\rho}{\varepsilon} + (1 + 2\nu) \quad \text{.....(3.5)}$$

3.1.1.1 Resistance Change of a Wire Due to its Strain

Strain is defined as the ratio of the elongation of a material to its original length upon application of load. In the previous section, the resistance of a wire is derived to be a function of its resistivity, and its dimensions. When a wire is loaded it changes its dimensions, i.e load creates strain on the wire.

The stress-strain behavior of metals were explained in Chapter 2. Upon application of tensile force, metals experience a homogeneous uniform thinning throughout the material which in return creates a uniform resistance change throughout the length. This is accepted to be true when loaded up to the Ultimate Tensile Strength (UTS). Forces that result in stress values that are greater than UTS cause necking, a non-homogeneous thinning of the cross-section, in the material which result in non-uniform thinning and non-uniform resistance change in the material.

The stress applied to a material up to its yield point does not cause permanent deformation and upon its release the material recovers to its original shape and original resistance. Although loads creating stresses between the yield point and UTS create permanent deformation in a material, since the deformation is considered to be homogeneous, the resistance change throughout the material is still uniform. Following this discussion, it is concluded that even a deformed wire, unless it does not exceed the UTS, can be used as a strain indicator as long as proper calibration values are provided.

3.1.2 Calculation of Strain from the Resistance Change in a Wire

Until this section the basic theory of resistance, and resistivity are presented and it is explained that an elongation in a material creates a resistance change. This change can be measured using a Wheatstone bridge. In this section, the relationship between the output voltage of a Wheatstone bridge and resistance is outlined, and the formulae used for this relation are presented [7, and 8].

A Wheatstone bridge is a circuit that is extensively used in resistance measurement applications. It allows highly accurate measurements of small resistance changes (in the miliohm magnitude) for resistance values within 1 ohm to 100000 ohms range. This is not possible to measure with regular resistance measuring devices such as multi-meters. [27].

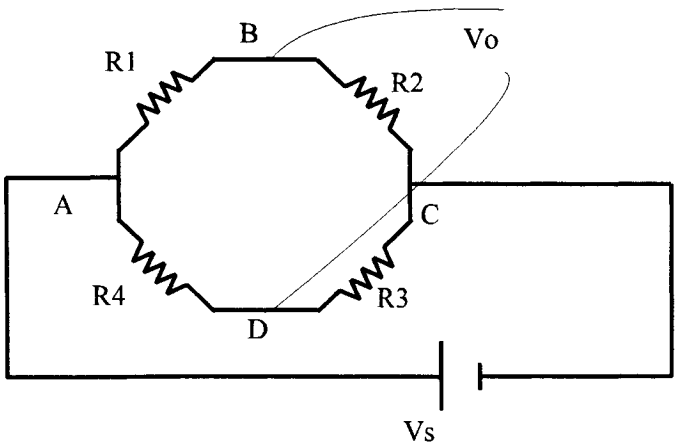

Figure 3.3: Wheatstone Bridge

A schematic representation of a Wheatstone Bridge is shown in Figure 3.3. It is composed of 4 resistive arms (R1, R2, R3, and R4), a voltage source (Vs), and a voltage output indicator (Vo).

The voltage output (Vo) reflects any change in the resistance of one or more of the arms. The top and bottom parts of the bridge act as individual voltage dividers. The voltage output is determined from the differences in the voltage dividers as a function of resistor arms and the voltage source. This is mathematically expressed by using Equation 3.6. [32][The derivation of the equations in this section of the report are included in Appendix-I];

$$V = \frac{(R1 \times R3) - (R2 \times R4)}{(R1 + R2)(R3 + R4)} \times Vs \quad \text{.....(3.6)}$$

The resistance change of a wire with respect to strain is related through the gage factor, G. Consequently, the strain in the wire is found using $\frac{\Delta R/R}{G}$.

In practical applications the gage factor is determined experimental by calibrating the sensor by applying known strains. In theory, the gage factor is related to resistance and resistivity. Taking the derivatives of Equation 3.1 and Equation 3.2, and substituting into Equation 3.5 results in;

$$G = 2 + \frac{\frac{dv_o}{v_o} + \frac{d\lambda}{\lambda} + \frac{dN_o}{N_o}}{\varepsilon_L} \quad \text{.....(3.7)}$$

Equation 3.7 shows that in theory, the gage factor of a sensor is related to electronic variables at the atomic level, and that the gage factor is never constant unless the numerator of the second term of Equation 3.7 is zero or related to strain with a constant. While any change in strain would cause a minute change in gage factor, for all practical purposes engineers accept that gage factor of most materials is constant. It is however very common to find materials that has clearly different average gage factors in the elastic and plastic regions for the same material. This is believed to be a originated from the fact that the electronic variables that affect the numerator of Equation 3.7 acts distinctly different in the plastic and elastic regions. For most of the materials the gage factor of plastic region is lower than the elastic region. In these materials the electronic variables are believed to reach to a steady state due to excessive dislocations and movements occurred in the plastic region, i.e. In the plastic region the resistance change is dominated by geometrical changes. [8, 30, and 31]

Commonly used Wheatstone bridges operate by a zeroing system (Galvanometer), that is the output voltage of the bridge indicates a zero value when the ratio of the opposite arms of the bridge are equal. In this type of systems, the strain on the gage is measured by adjusting the resistance value of the opposite arm of the strain gage.

The proposed system, on the other hand, works with a non-zeroing principle. Since there are more than one strain sensor, and to zero the output voltage by adjusting the resistor is too

time consuming, it is decided to read the bridge output directly and convert the difference in the readings to strain by using the Equation 3.8. This method is believed to be more efficient for multiple strain sensors and for quasi-static strain measuring applications.

An experimentally determined gage factor is used to calculate the strain by using Equation 3.5 and Equation 3.6. The resistance of the strain measuring wire is calculated using;

$$R_{gage} = \frac{\left(\frac{2 \times V_0}{V_s}\right) \times R + R}{1 - \left(\frac{2 \times V_0}{V_s}\right)} \quad \text{.....(3.8)}$$

The differences in two consecutive measurements gives ΔR. This value is substituted into the rearranged form of Equation 3.5 to calculate the strain on the material:

$$\varepsilon = \frac{\Delta R / R}{G} \quad \text{.....(3.9)}$$

3.2 Design Process of the Proposed System

In this section, the criteria used to select the elements of the strain measuring system and its design are presented. These include the selection of sensor wire, determining the wire diameter, choosing the carrier for the strain sensors, and the switch system and the relays.

3.2.1 Selection Process of the Strain Sensing Wire

It is briefly explained in the previous section that the proposed strain measuring system utilizes a bridge that measures the resistance change on a single filament wire as its carrier is stretched. One might initially think that having higher resistance in the gage material increases the strain sensitivity of the gages. In fact, sensitivity of a gage to strain is independent of its initial resistance, because the relative resistance change (ΔR/R) is normalized by the initial resistance. Increasing the strain sensitivity of a system is possible by selecting alloys with high gage factors. Despite this discussion, using a high initial resistance for a strain measurement is still important. Using higher resistance gages increases the signal to noise ratio of the signal, and

at the same time heating is minimal due to the minimal current passing through the material. For the commercially available bonded resistance gages, the resistance can be increased by increasing the number of loops used in the gage for the same length. In the proposed sensor system, a single filament wire is used for strain measurements; therefore, the only way to increase the resistance is to use a high resistivity alloy wire.

Constantan is considered to be the most widely used alloy in commercial electrical strain gages. It is used in static or quasi-static strain measuring applications. Constantan is an alloy with an almost constant gage factor in its elastic and plastic regions, and it is known to be very inexpensive. Other widely used strain measuring alloys are Isoelastic, Armour D, and Karma. Karma has very similar characteristics to Constantan and it is less affected from temperature changes; however, it is very difficult to solder to Karma. Isoelastic is usually used for dynamic strain measuring applications due to its superior fatigue life, but it is very sensitive to temperature fluctuations. Armour-D on the other hand is used for high temperature applications, i.e. above 230 °C.

Another alloy that might be used is Kanthal-A1 (KA1) alloy. This alloy has a similar composition to Armour-D. KA1 has very high resistivity values as well as desirable thermal characteristics that are very close to Constantan. KA1 alloy has one of the highest resistivity values compared to the other alloys. As a result of the search KA1 alloy was selected as the alloy for the strain sensing wire.

The comparison of characteristics of the most popular alloy Constantan and KA1 are presented in Table 3.1. The chemical composition and the mechanical properties of KA1 alloy are tabulated in Table 3.2. Strain measuring companies prefer constantan because of its almost constant gage factor for both elastic and plastic deformations. One of the other reasons for the strain gage companies not using KA1 instead of Constantan is suspected to be the cost of the KA1 wire. KA1 is almost twice as expensive as Constantan.

Table 3.1: Comparison of the characteristic properties of Constantan and KA1.

	Constantan	KA1
Resistivity [x10-8 Ω-m]	48.88	147.47
Temperature coefficient of resistance (TCR)	0.00002	0.00002
Coefficient of linear expansion [x10-6 m/m-°C]	14.9	15

Table 3.2: Chemical composition and mechanical properties of KA1 wire.

Chemical Properties	wt%22 Cr, wt%5.8 Al, balance Fe
Ultimate Tensile Strength (UTS)	760 MPa
Yield Strength (YS)	545 MPa
Modulus of Elasticity @ 20°C	220 GPa
Strain @ Yield Point (Theoretical)	0.00248
Poisson's Ratio	0.3

3.2.2 Selection of the Diameter of the Wire

After determining the alloy of the wire, it is necessary to determine its diameter. If only the strain is considered to create a resistance change on the wire, i.e. the resistance changes due to electrical effects of resistivity is neglected for a moment, the resistance change of a wire is theoretically calculated through dimensional changes calculated from Equation 3-1 upon application of a load. The stress created by the load leads to axial and transverse strain. These strains corresponds to a change in the resistance due to the equation. Figure 3.4 is plotted using the procedure outlined above for different diameters of KA1 wire. This graph is used to initially determine the appropriate diameter for the strain sensor wire.

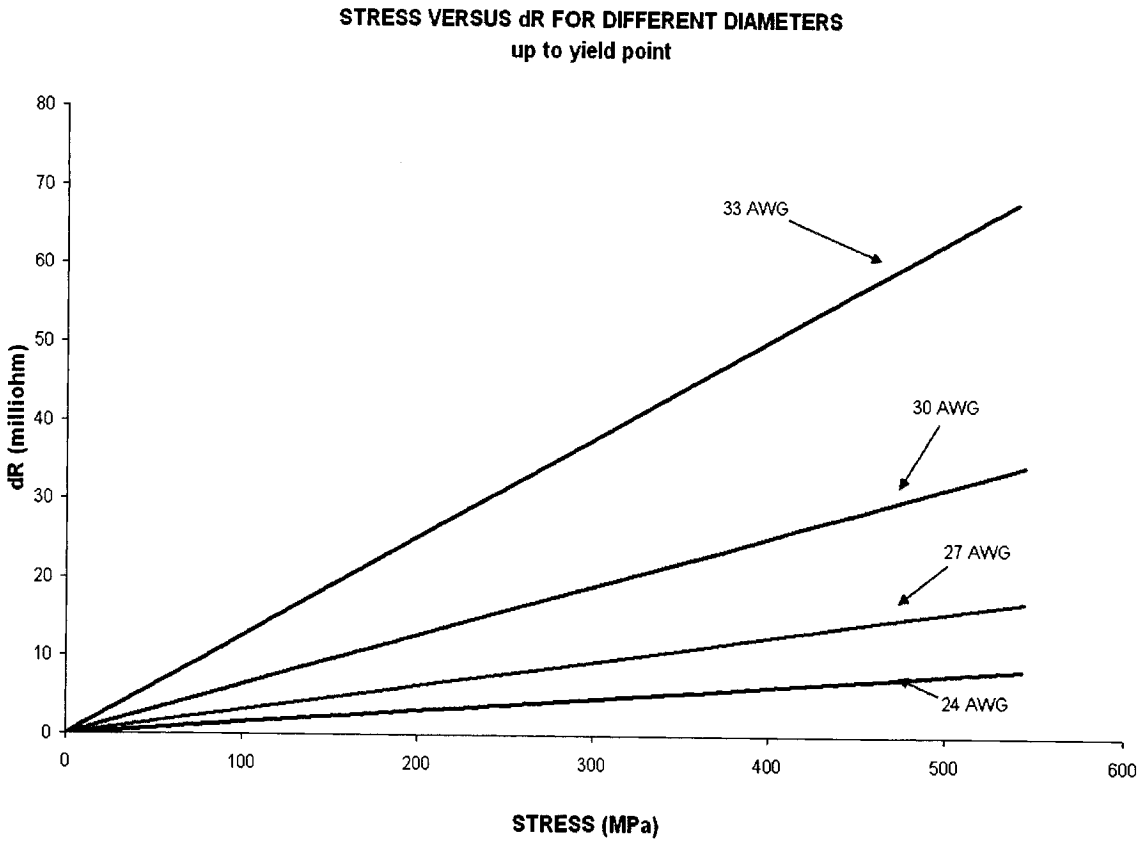

Figure 3.4: Stress versus resistance change for KA1 wires of different diameters (calculated).

The graph is plotted up to the yield point (~545 MPa) of KA1 alloy for 4 different diameters. It is shown that for the same stress, higher change in resistance is observed as the diameter is decreased, i.e. as the AWG number increases from 24 AWG (0.511 mm) to 33 AWG (0.180 mm). This results in a higher signal to noise ratio, thus providing more accurate measurements. Although it is concluded from the graph that smaller diameter wire is preferable, due to possible handling problems during this phase of the study a diameter of 33 AWG is selected.

As mentioned in the beginning of the chapter, Copper wires are used to divide the KA1 wire into equal length multiple segments. The KA1 wire and the copper wires are then embedded into the carrier together. As a result of this configuration, as the carrier is elongated the Copper wires stretch the same amount that the KA1 wires stretch. The contribution of the

copper wires to the system is ignored in the calculations due to their low magnitude of the resistance and the resistivity. The copper wires have a resistance of 0.1 ohm and a resistivity of 1.68 x $10^{-8}\Omega$-m for the specified gage lengths; whereas the KA1 wire has 17.3Ω and 147.47 x 10 $^{-8}\Omega$-m, respectively. Since the resistance of copper is almost 0.5% of the KA1 wire, the resistance change created can be neglected.

3.2.3 The Selection Process of the Carrier

Since the change of resistance in a wire is detected and converted into strain, factors that might interfere with the measurements have to be eliminated for accurate strain readings. For this purpose, the strain measuring wire has to be electrically isolated and at the same time protected from environmental factors, i.e. a durable and a rugged exterior has to be provided to the proposed strain sensors. This is usually done by means of a carrier. Since the proposed system is mainly designed for structural concrete applications, and it is required to carry distributed multiple strain sensors, it is decided to use a circular rod carrier. The carrier is required to have the ability to elongate large amounts without breaking, as illustrated in Figure 2.3. At the same time it has to have matching mechanical characteristics, such as elastic modulus, to that of the KA1 wire in order to have negligible relative strain due to the differences in the Elastic Modulus of the two materials.

For this study a pultruded fiberglass FRP rod is used as a carrier. The light weight, elastic modulus, ultimate tensile strength of the chosen pultruded fiberglass FRP rod were found to well suited for the need. According to the preliminary calculations; at the approximate yielding strain of the KA1 wire, 2480 $\mu\epsilon$, the strain difference between the rebar and the wire would be approximately 0.008 $\mu\epsilon$ which is accepted to be a negligible difference. This calculation is presented in the Appendix-II.

The mechanical properties of the carrier are given in Table 3.3. Since this is a commercial product, further information was not provided by the manufacturer. The process of manufacturing the strain sensor and embedding the KA1 wire into the carrier is discussed later in this thesis.

Table 3.3: Properties of the pultruded fiberglass rod.

Glass Content	65 wt%
Tensile strength	689 MPa (100000 psi)
Tensile modulus	37.92 GPa (5500000 psi)
Compressive Strength	413 MPa (60000 psi)
Diameter	12.7 mm (0.5 inch)
Length	183 cm

3.2.4 Automation of the Measuring System

Figure 3.5 shows multiple strain sensors, composed of KA1 wire, embedded into a carrier. The measurements of resistance changes on the wire is taken by a voltage divider bridge. The three stable arms of the bridge are carbon filled resistors. A 1.5 volt battery is used as a voltage source, and due to the concern of overheating the strain gages, a minimal current is fed to the arms of the bridge (approximately 13 milliamps) by connecting a resistor to the bridge in a series configuration. A battery type voltage supply is chosen over an ac regulated voltage supply, because ac type voltage supply can easily introduce noise to the system which creates disturbances in the bridge output.

The switching between the distributed strain gages is done by relays. The two major criteria used for the selection of the relays are low contact resistance (50 milliohms) and short open/close time (less than 4.5 milliseconds). The locations of the relays are indicated in Figure 3.5, and the opening and closing sequence of the desired relays is accomplished by Labview.

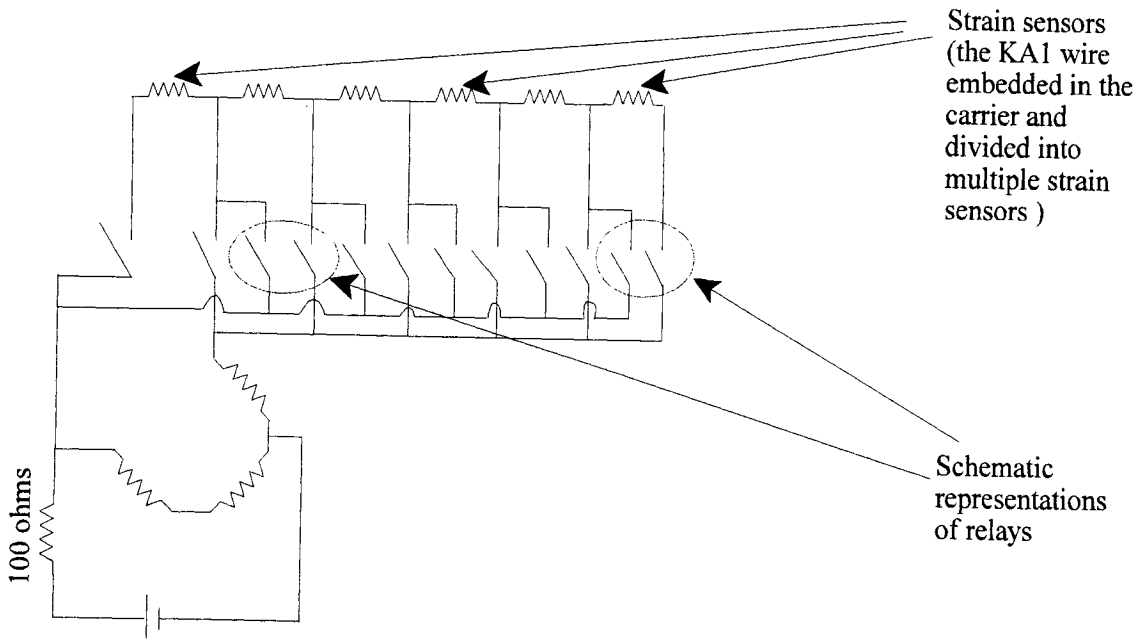

Figure 3.5: Schematic representation of the switch system with the relays.

Chapter 4: Characterization of the KA 1 Wire

In this chapter, the strain measuring alloy used in the proposed strain sensor is investigated, and the test results conducted on the bare KA1 wire are presented. Although the characterization and calibration of the measuring system is conducted and presented in Chapter 5, the preliminary mechanical and electrical measurements presented in this chapter are of fundamental value in calibrating the measuring system. These results are used for the interpretation of the behavior of the prototype sensor that is outlined in Chapter 5.

Firstly, the KA1 wire is subjected to elementary tensile tests. These tests are used to characterize the mechanical behavior of the material, and the data gathered are compared to the supplied mechanical properties of the KA1 wire presented in Table 3.2.

Possible microstructural defects in the specimens, inaccuracies in the test machine, and human originated problems may cause small differences in the test results. The tests were repeated three times to get an average value. The tests were conducted on an Instron Universal tensile test machine. The gage length of the specimens are chosen to be 280 mm to have similar lengths to that of the gage length used in the proposed system. In tensile tests 24 AWG KA1 wire is preferred over 33 AWG KA1 wire because of to its larger diameter. Using larger diameter wire would allow the application of higher loads to obtain the same stress value. Applying higher loads would result in better resolution of the data output of the Instron testing machine.

The tensile tests are conducted using wedge-action mechanical grips. The ends of the wire specimens are fixed between the grips. Aluminum sheet metal is used to transfer the force from the grips to the wire to avoid excessive stress concentration on the wire at the grips. These tests were conducted to verify and compare the data provided by the manufacturer and the material characteristics databases [33]. A test procedure in the ASTM standards for filament wire tests exists (ASTM designation: A 318-56, "Standard Method of Tension Testing of Steel Spring Wire"); however, it requires a loop-winding type test grips which was not available. Since the preliminary tests provided satisfactory results, no further tests were conducted using the ASTM standards. In these tests an extensometer was not used because of the difficulty of attaching it to the 0.51 mm diameter wire.

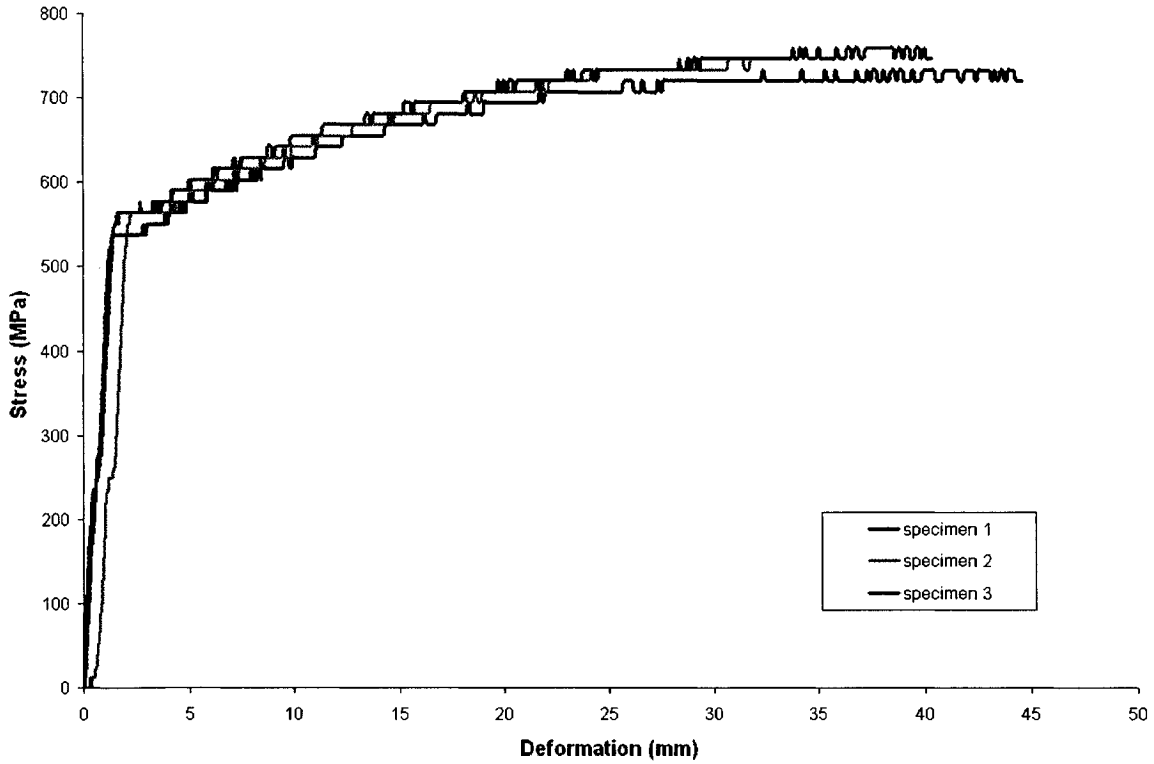

Figure 4.1: Stress versus deformation of KA1 wire.

Figure 4.1 shows the stress versus deformation graph of the three tensile tests performed. From the average of the three tests the yield strength and the ultimate tensile strength of the alloy is determined to be 550 MPa and 747 MPa, respectively. These compare favorably with the values obtained from the manufacturer and the standard materials characteristics data bases (545 MPa for yield strength and 747 MPa for ultimate tensile strength). Due to the inaccuracy in measuring the strain in the elastic region, i.e. not using an extensometer, an elastic modulus of 152 GPa is obtained. This value does not compare well with the 220 GPa at 20°C supplied by the manufacturer. If an extensometer is not used and the displacement of the crosshead of the tensile machine is used for strain calculation, the measurement would include the deflection of the load cell, deflection of the crosshead and deflection of the grips that is added to the deformation of the specimen. Adding to this source of error, some slippage of the wire can also create a source of error. Since the magnitude of the errors are not known, and since the expected

and measured strength values are within 2% of each other, the elastic modulus data provided by the manufacturer is used.

An average of 14% elongation to failure was measured. This value is approximately 20% in the material databases. All the specimens fail at the grips which indicate that the failure is partially due to stress concentrations due to excessive grip forces. This is believed to cause the difference in elongation at break between the expected and measured values.

Figure 4.2 shows the cold working, i.e. strain hardening, effect of KA1 wire for 2 specimens. Initially, the specimens were loaded to approximately 640 MPa and then they were unloaded. The value of 640 MPa is above the yield strength and below the ultimate tensile strength of the alloy. Since the tensile load is above the yield point, the material is plastically deformed. The specimens were then reloaded up to failure. In this case, the specimens followed the same slope in the elastic region; however, due to the cold working effect of the previous loading the yield point was found to be 650 MPa. This corresponds to approximately 15 % increase in the yield strength. As is found for many metals that are deformed to low values of cold working, the UTS value remained unchanged.

The resistance changes of the 33AWG and 24AWG KA1wire when loaded were also tested. The 24 AWG diameter wire tests were conducted on an INSTRON tensile machine; however, the 33AWG diameter wire tests were conducted by manually hanging calibrated weights from the wire and recording the resistance after each load application. The hanging weight approach was used for the thinner wire only, i.e. 33AWG. The 100 kN load cell used in the INSTRON tensile machine did not provide good resolution at the range of 0 to 0.013 kN that corresponds to the elastic portion of the 33 AWG KA1 alloy wire.

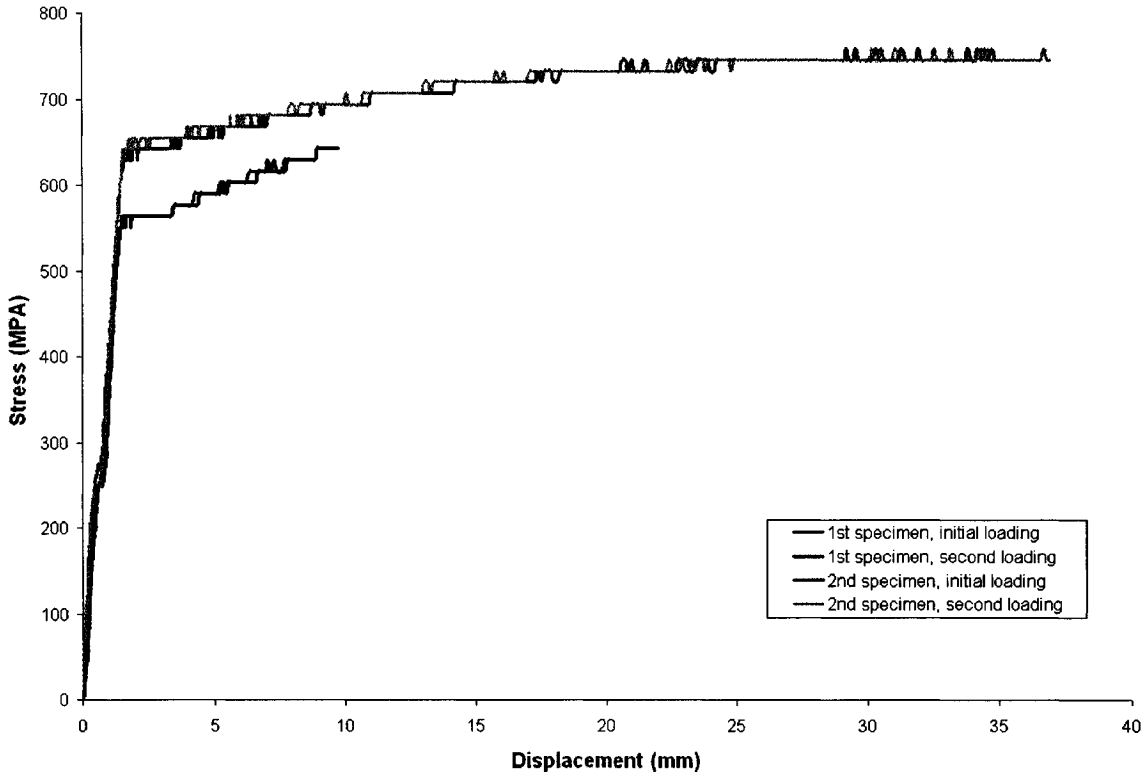

Figure 4.2: Cold working of KA1 wire.

Figure 4.3 shows a plot of the ratio of resistance change to initial resistance ($\Delta R/R$) versus load of 24 AWG KA1 wire. Up to about 100 N, $\Delta R/R$ increases linearly with the load. This load

corresponds to approximately 490 MPa, which is the approximate yield point of the wire. After the yield point, a dramatic increase in the $\Delta R/R$ is observed. This test is repeated for three different specimens and the behavior is observed to be consistent. Two of the specimens used had a length of 280 mm where the third had a length of 420 mm. The longer specimen has higher resistance value compared to the other two specimens, but because the resistance change is normalized all three can examined together.

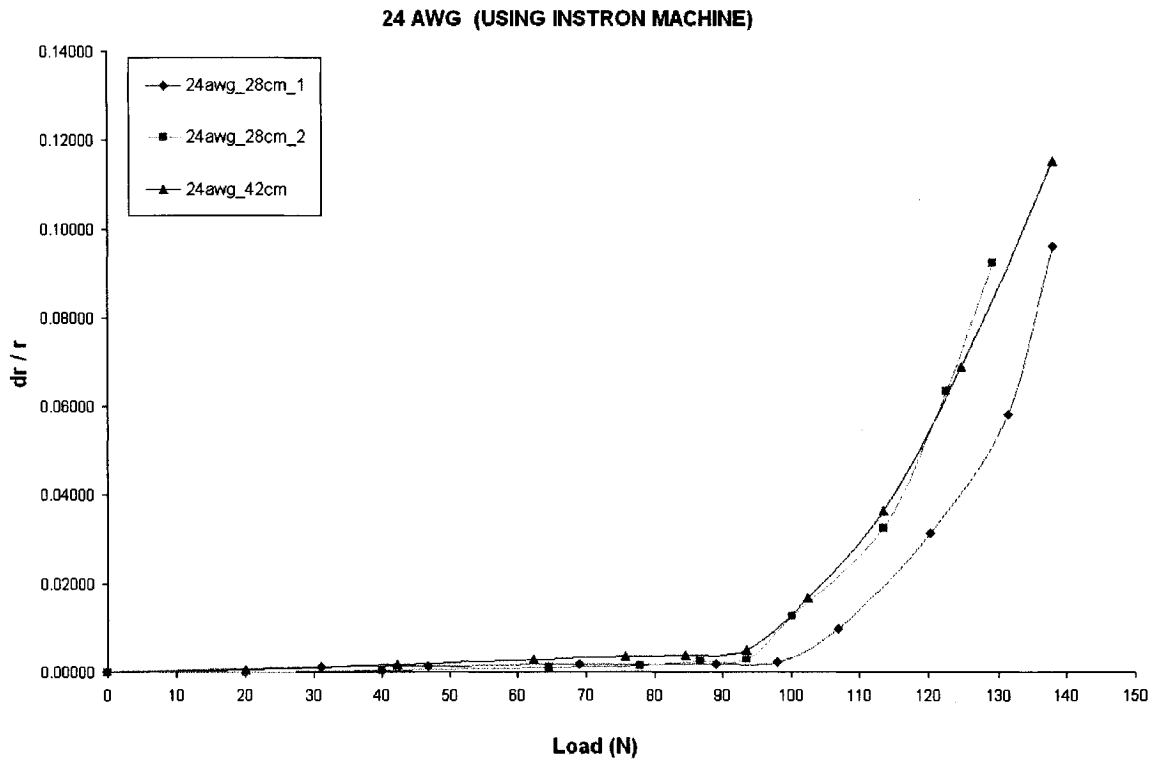

Figure 4.3: dR / R versus Load of 24-AWG KA1 wire specimens.

The results that corresponds to the elastic region of the wire in Figure 4.3 are re-plotted in Figure 4.4. This figure also includes the results of two 33AWG wire specimens with 30 cm gage length. The load that was applied during the tests was converted to theoretical strain by using the elastic modulus of the KA1 for this graph. It is shown in this figure that the curves for the 24AWG-280 mm long specimens fluctuate more than that for the 24AWG-420 mm specimen. On the other hand, the two 33AWG-30 cm specimens show linear increase (with the least fluctuation) of $\Delta R/R$ as the strain increases.

Less fluctuation of the curves is believed to be due to the higher initial resistance values of specimens. As the initial resistance increases, the signal to noise ratio increases and this enables the Wheatstone Bridge to detect the signal with more consistency.

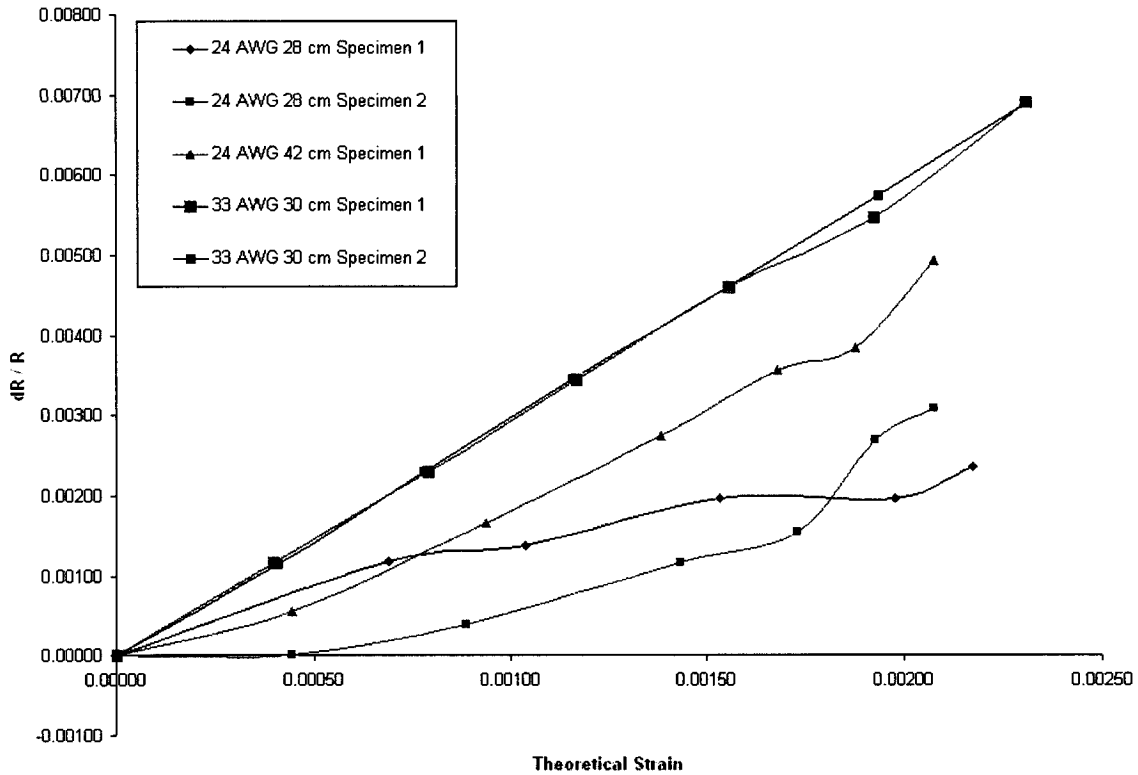

Figure 4.4: dR/R versus theoretical strain of 24 AWG and 33AWG KA1 wire specimens.

The findings of these experiments prove the validity of the discussion about the necessity of choosing a high initial resistance to get higher signal to noise ratio during measurements. The gage factor of the bare KA1 wire is determined from the slope of the two 33AWG-30 cm wires as approximately 2.9.

The results presented in this chapter included determination of the mechanical and electrical properties of the strain measuring wire. Also, as a result of the findings, the diameter of the wire that is used in the proposed system is confirmed. The fabrication and testing of the prototype of the system is covered in the following chapter.

Chapter 5: Fabrication and Testing of the Prototype LGS Sensors:

This chapter is divided into three sections. The first section outlines the fabrication of the LGS sensors. The second section presents their prototype preparation for calibration tests. The last section presents the test results and the related discussions.

5.1 Fabrication of the Prototypes

It had been mentioned earlier that the sensor gage length that will be used for purposes of this work is 30 cm. With reference to Figure 5.1, a length of the 33AWG KA1 wire is segmented into two. This is done by soldering 30AWG copper wire taps that are made available at one extrema of the KA1 wire. The copper wire is pre-insulated along its length. Measuring the change in resistance between the middle tap and each of the other two taps will give an indication of the strain experienced by each of the segments of the strain sensing wire respectively.

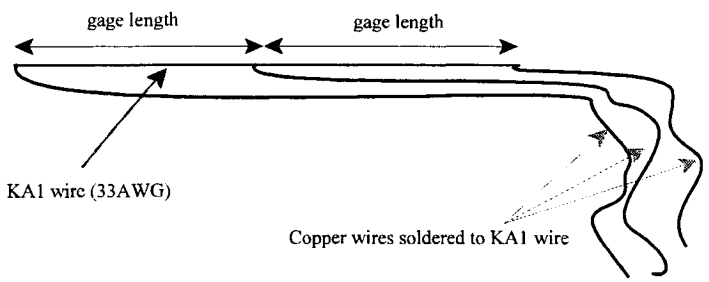

Figure 5.1: Schematic representation of the strain measuring wire.

The strain sensing wire array is then embedded into a fiberglass rod carrier (with 12.7 mm diameter) that has been grooved as shown in Figure 5.2. The groove runs along the length of the rod and has a depth of 1.6mm and a width of 1.6mm. The array is secured in place using epoxy resin.

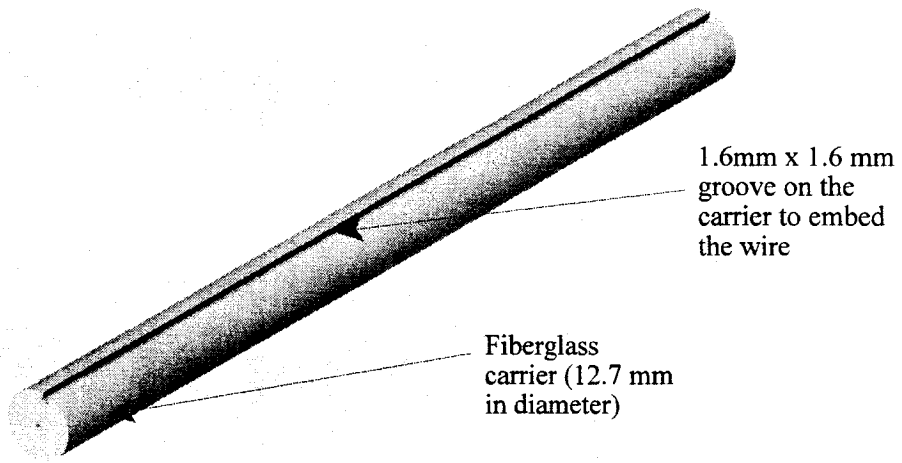

Figure 5.2: Schematic representation of fiberglass carrier and the groove on it.

5.2 Preparation of the Prototypes for the Tests

It has been outlined in Chapter 2 that due to the high compressive and almost negligible tensile load capacity of concrete, it is assumed in the design of concrete structures that the compressive load is carried primarily by the concrete, while the tensile load is carried primarily by the steel. Failure is assumed to occur due to the strain in the steel. Hence it is important to monitor the tensile loadings in concrete. The compression strain in a concrete element can be calculated using the tensile strain measured and the location of the sensor. During the calibration experiments two tensile test specimens, and one compression test specimen was prepared and tested.

With reference to Figure 5.3, the tensile test specimens are composed of a two segment strain sensor and a load transfer zone at each end to a total length of 84 cm. Each sensor segment is 30 cm long. The load transfer zones are 12 cm long. The specimen was manufactured by embedding an 84 cm carrier with the two segment strain sensors into two steel pipes one at each end. The pipes were then filled with high shear strength epoxy resin. The steel pipes have a 4 cm threaded section for mounting onto the Instron machine. The load is transferred from the

testing machine to the pipes through the thread, and then from the pipe to the strain sensing wire through the epoxy resin and the carrier.

The carriers in the pipes are centered during the curing of the epoxy resin to avoid any off-axis tensile loadings that may create bending moments on the specimens during tests.

The surface of the middle length of the specimens were coated with a thick layer of epoxy. This was done to cut two V-notches on these layers of epoxy to mount the extensometer during the tests. This method is preferred to avoid opening notches on the carrier, because this may weaken the fibre composite carrier.

The compression test specimen was prepared following the same procedure as the tensile test specimens; however, only one segment of 30cm gage length was used. This is to reduce the possibility of buckling of the specimen due to length to diameter ratio.

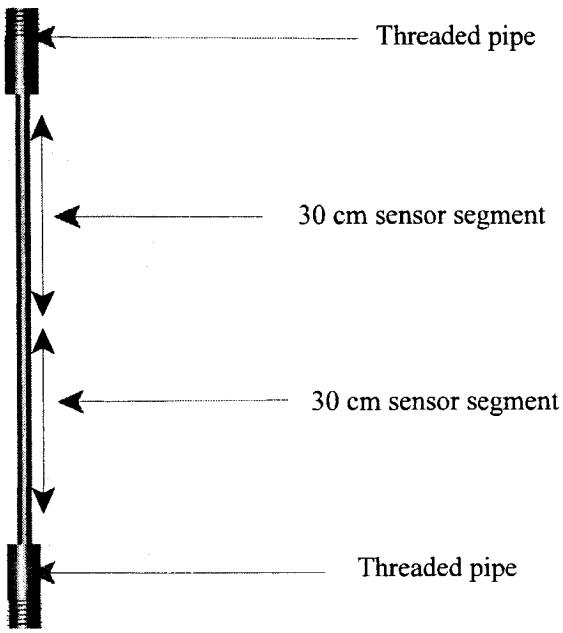

Figure 5.3: Schematic diagram of a tensile test specimen.

5.3 Test Results

The prototypes (specimens) were tested for characterization and calibration purposes. Tensile and compression tests were conducted using a Universal Instron Tensile test machine at the University of Ottawa Composite Materials Laboratory. This type of testing is preferred to achieve pure tension or compression on the specimens.

The measurements for the tensile and compression tests are conducted using Labview. One of the relays that is shown in Figure 3.5 closes forming a circuit with the bridge to monitor the desired sensor on the carrier at the desired instant. The rest of the relays stayed open. This allowed the monitoring of only one sensor at a time among the multiple sensors on the carrier. When a relay closed 250 measurements were taken. The range of these measurements are found to be ±2.5% of the average data. The results that are presented here are the average of these measurements.

After taking the measurements for a desired period of time , the particular relay opened and the next desired relay closed. At every time a relay closed, along with the output of the LGS sensor, the output of the extensometer, and the output of the load cell were recorded simultaneously. This enabled the user to have synchronized data at every measurement point.

The experiments were conducted in a laboratory environment; therefore, the change in temperature during the tests was assumed to be negligible.

5.3.1 Tensile Tests:

During the tensile tests the two specimens were subjected to strains that are within the elastic region of the KA1 wire. Subsequent to the these tests, the specimens were strained beyond the elastic region of the KA1 wire to determine the characteristics of the proposed strain sensor in the plastic region.

5.3.1.a Tensile Tests within the Elastic Range:

The two specimens used for the elastic region tensile tests were loaded twice during a test to observe the repeatability of the sensors. Measurements were taken during the loading and subsequent unloading of the sensors to characterize their responses.

Strain data was collected from the Instron machine controller. The voltage output of the bridge was used to calculate the values of $\Delta R/R$. This was plotted against the strain of the specimen to find the gage factor. The results for the cyclic loading of the first specimen are presented in Figure 5.4 and Figure 5.5 for its first and second sensors, respectively. The results for the second specimen are presented in Figure 5.6 and Figure 5.7 for its first and second sensors, respectively. The gage factors of the sensors were found using the linear least square fit method. Table 5.1 presents the results along with their correlation coefficients (R^2).

Table 5.1: Gage factors of the four sensors.

	Sensor	**Gage Factor (G)**	**R^2**	
Specimen #1	1	2.622	0.994	Figure 5.4
Specimen #1	2	2.561	0.995	Figure 5.5
Specimen #2	1	2.615	0.997	Figure 5.6
Specimen #2	2	2.579	0.996	Figure 5.7

In practical applications, these gage factors can be rounded to one decimal as 2.6 for all of the four sensors. This rounding off would create a maximum of 1.1% difference in the results for the strain sensors (calculated for 2.6 versus 2.63 gage factors) and this can be accepted as a negligible difference. Hence, the value of 2.6 will be used as the gage factor of the sensors for the remainder of the thesis.

The gage factor of 2.6 is slightly smaller than the 2.9 found for the bare KA1 wire and reported in Chapter 4. The slight decrease in the gage factor is not an unexpected finding. In the experiments presented in this chapter the load is applied to the carrier and the resulting strain is transferred to the embedded KA1 wire by the epoxy. Figure 5.8 shows a schematic representation of the transfer process that takes place in the carrier. Figure 5.8(a) shows a sensor with zero load. With reference to this figure, assume the point A on the carrier and the point B on the wire are on the same cross-sectional plane. Figure 5.8(b) shows the sensor undergoing tensile loading. When the sensor shown in Figure 5.8(a) is stretched, the point A travels a ΔL distance longer then the point B as a result of the difference between the elastic modulus of the

carrier and the wire, the thickness of the carrier, and the shear modulus of the epoxy. Due to the effectiveness of this transfer media, a change in the gage factor is observed. In the strain gage industry, this is sometimes explained as the local reinforcing effect of the transfer medium on the strain sensor.

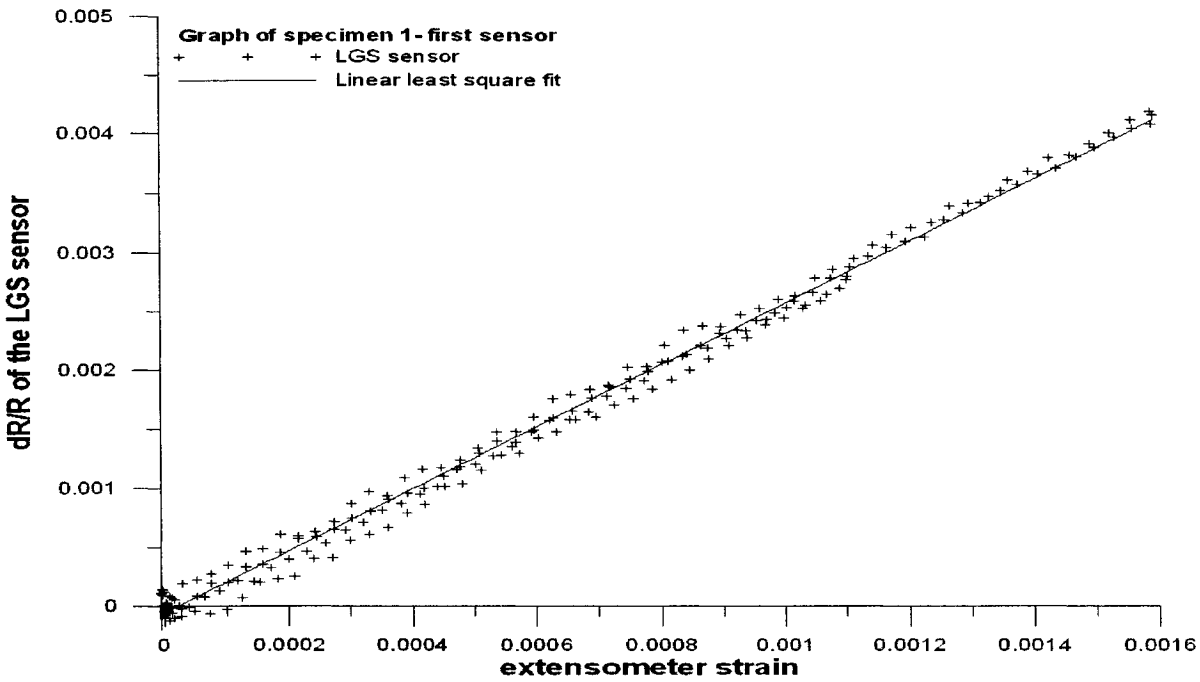

Figure 5.4: dR/R versus strain for first sensor on first specimen.

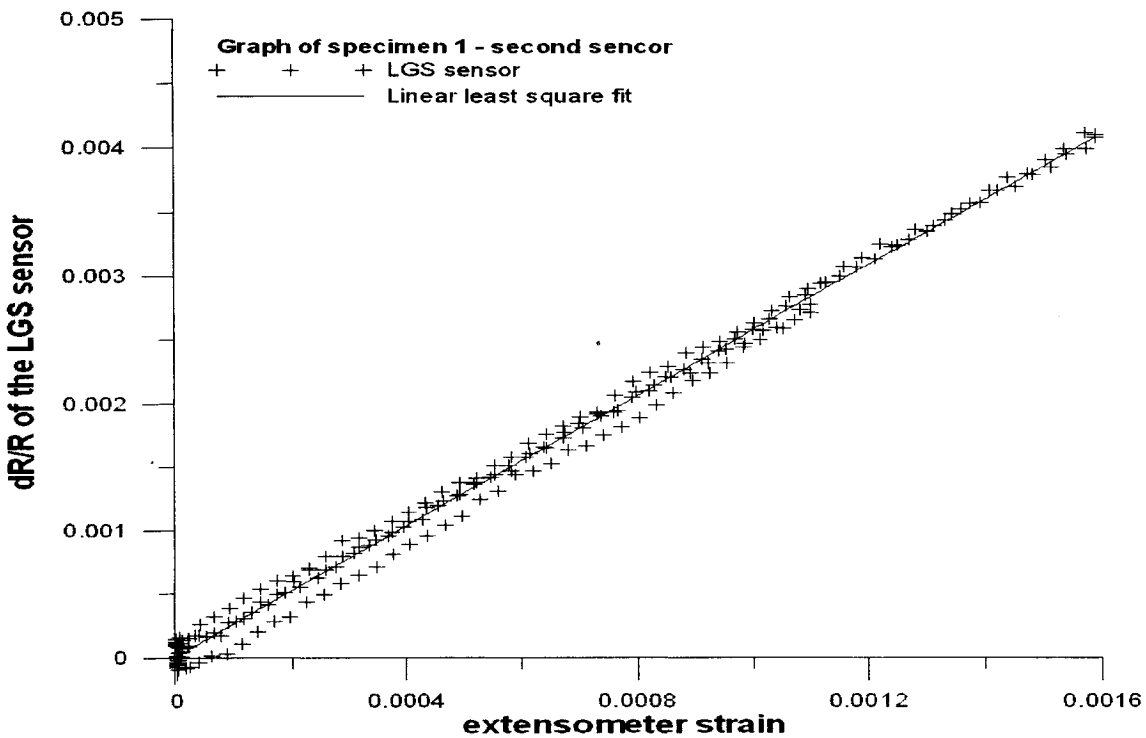

Figure 5.5: dR/R versus strain of second sensor on first specimen.

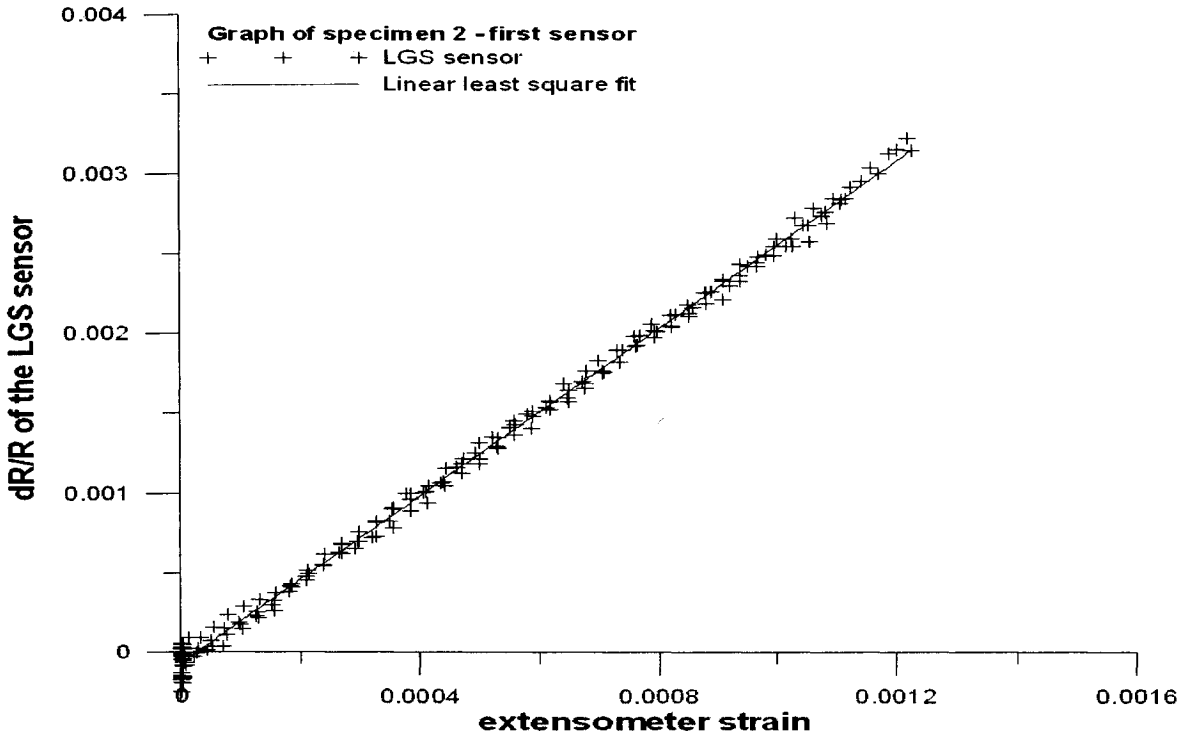

Figure 5.6: dR/R versus strain of first sensor on second specimen.

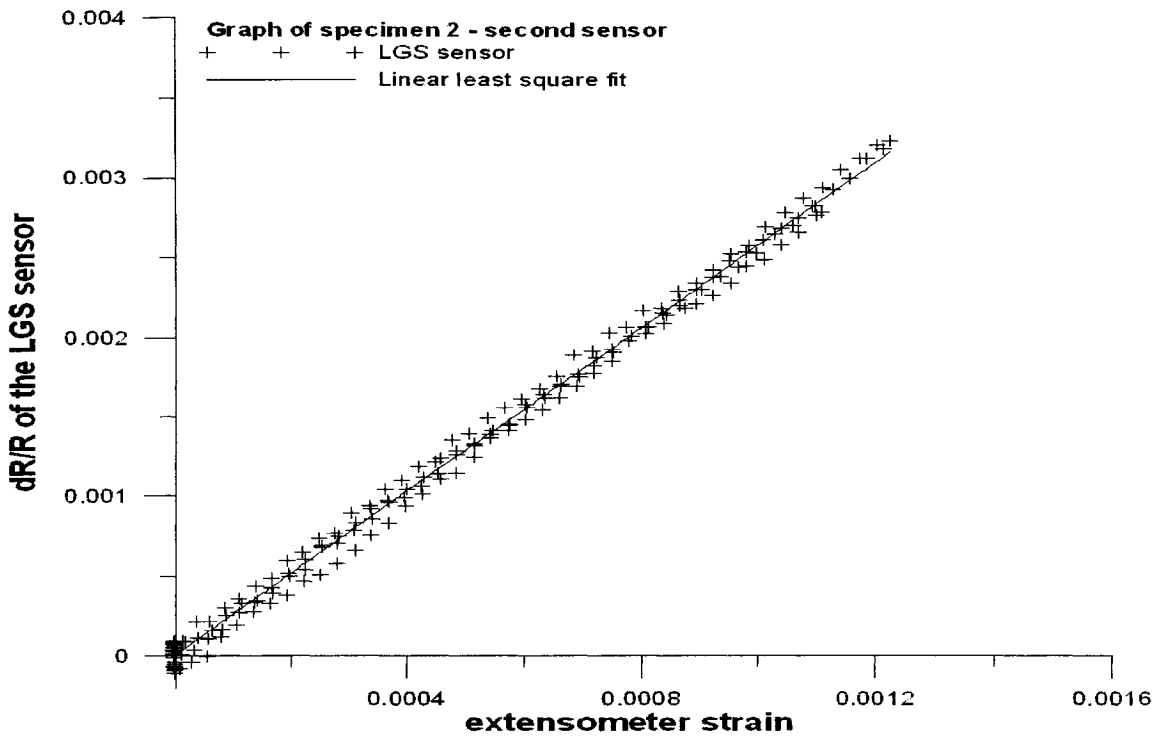

Figure 5.7: dR/R versus strain of second sensor on the second specimen.

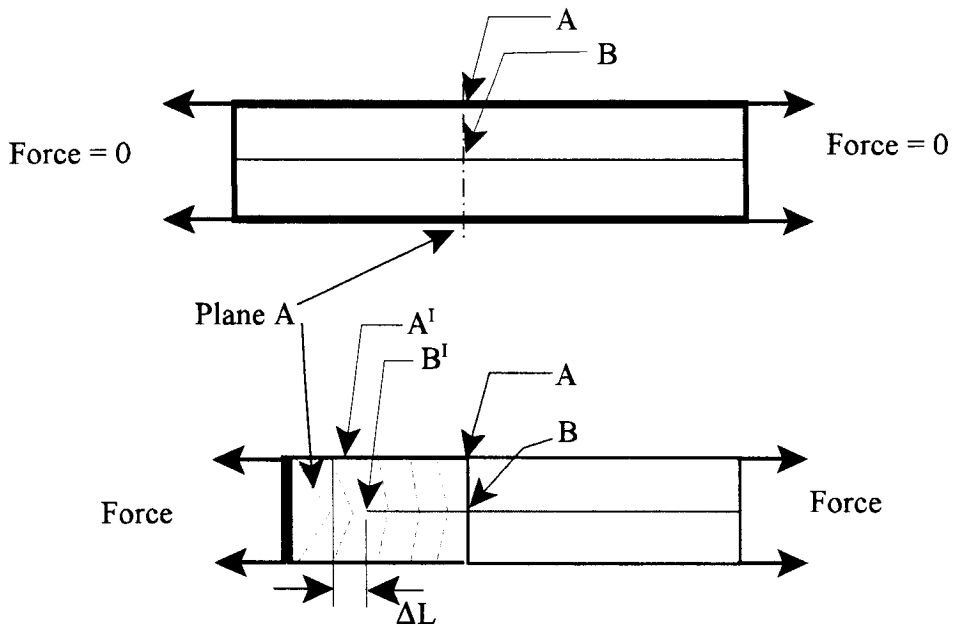

Figure 5.8: Schematic representation of the transfer process that takes place in the carrier. (a) Zero Load, (b) Loaded

The strain values of the sensors on the first specimen are presented in Figure 5.9 and Figure 5.10, respectively. The strain values of the sensors on the second specimen are presented in Figure 5.11 and Figure 5.12, respectively.

Two different sets of axes are presented in these four figures. The axis on the left shows the strain outputs of the LGS sensor and the extensometer which are plotted versus the load on the specimen. The specimens are loaded twice, these two loadings and subsequent two unloadings of the sensors are marked with arrows for clarity in Figure 5.9.

The first specimen is initially strained up to 1100$\mu\epsilon$ which is approximately half of the yield strain (2400$\mu\epsilon$) of the KA1 wire. In the second loading, the specimen is strained up to 1650$\mu\epsilon$. The loading is stopped before reaching to the plastic region of the KA1 wire, and the specimen is unloaded. Both of the sensors on this specimen shows almost identical responses.

The second specimen is initially strained approximately up to 1100$\mu\epsilon$. In the second loading, it is strained up to 1300$\mu\epsilon$. Both of the sensors on this specimen also shows identical responses.

The axis on the right presents the percent difference in strain between the LGS sensor and the extensometer. The percent differences for all four sensors are found to be within 10 % for strains above 400$\mu\epsilon$ (0.0004ϵ). This is shown in these four figures with green dotted lines. Yielding of most rebars take place at approximately 2300$\mu\epsilon$. As a result of the tests it is seen that the proposed LGS sensor is suitable for measuring strains that are greater than 400$\mu\epsilon$. This does not limit the use of the LGS sensor, because structural designers are interested in strains that can cause failure of structures as a result of yielding of reinforcements.

The larger differences between the ESG and the LGS sensors at small strains are believed to be the result of high noise to signal ratio at these small strains. The extensometer used in the tests has an ESG strain gage with an initial resistance of almost 6 times that of the LGS sensor. This results in an increase of the signal to noise ratio and provides reliable results with the extensometer even at small strains.

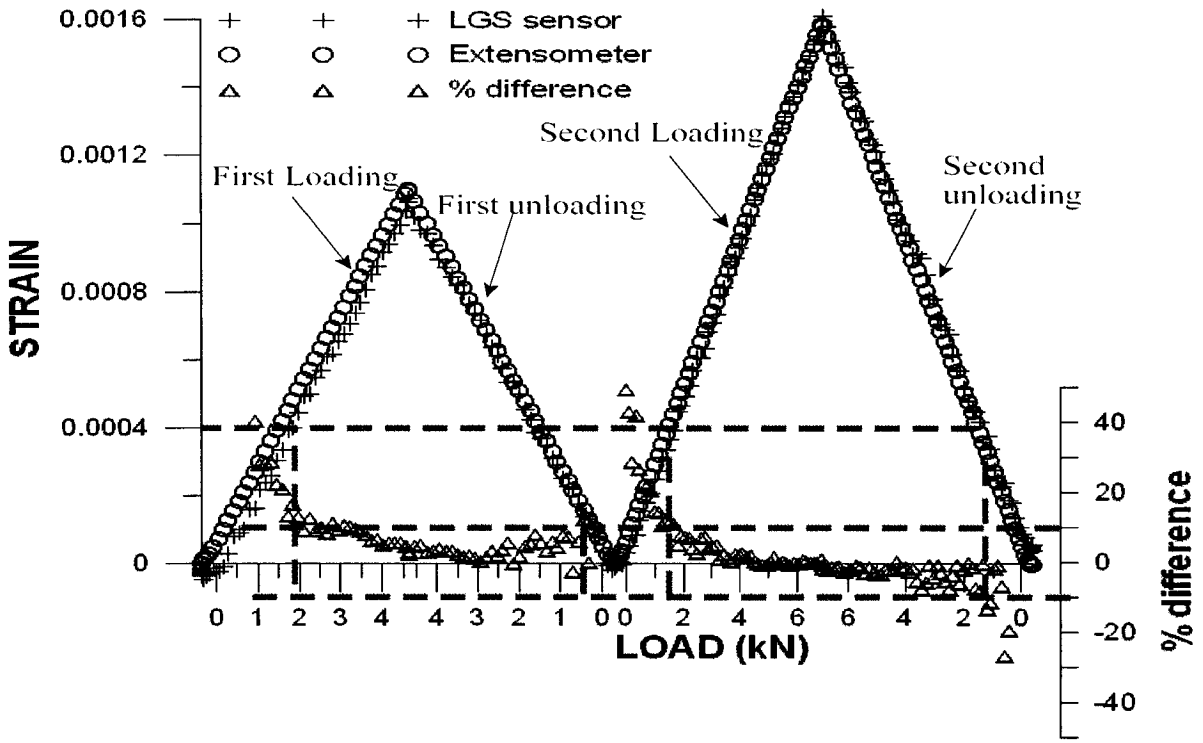

Figure 5.9: Strain of first sensor on the first specimen.

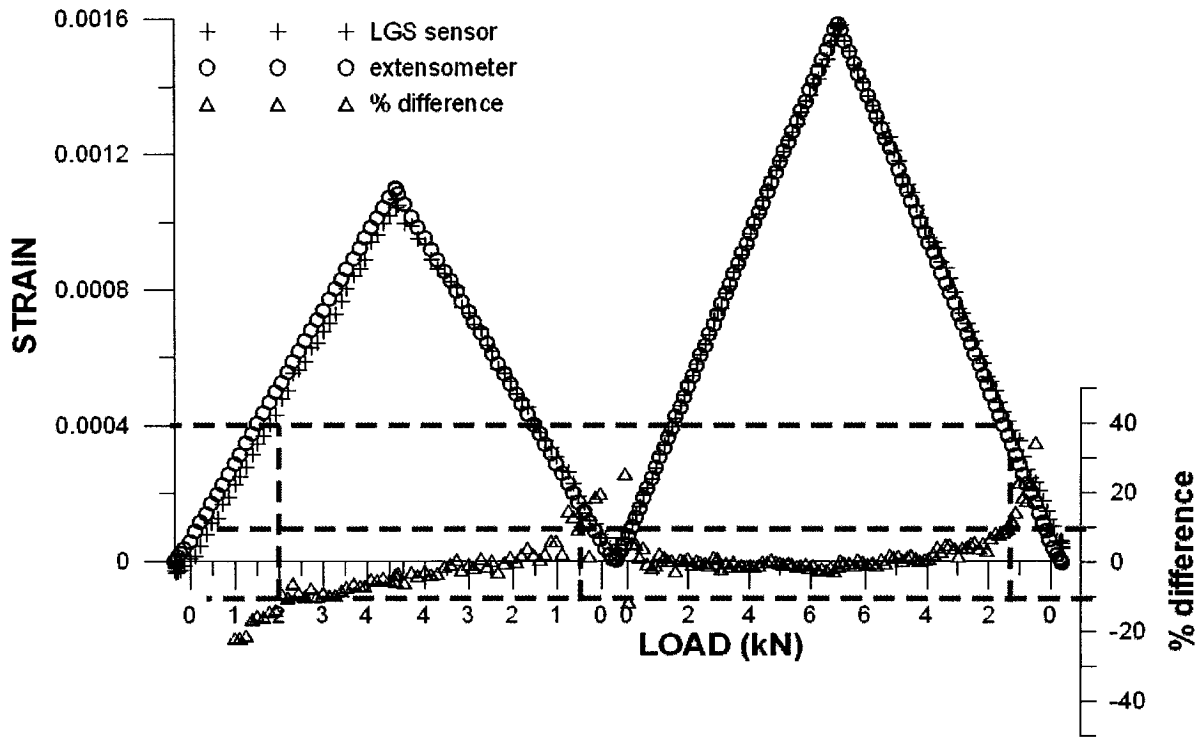

Figure 5.10: Strain of second sensor on the first specimen.

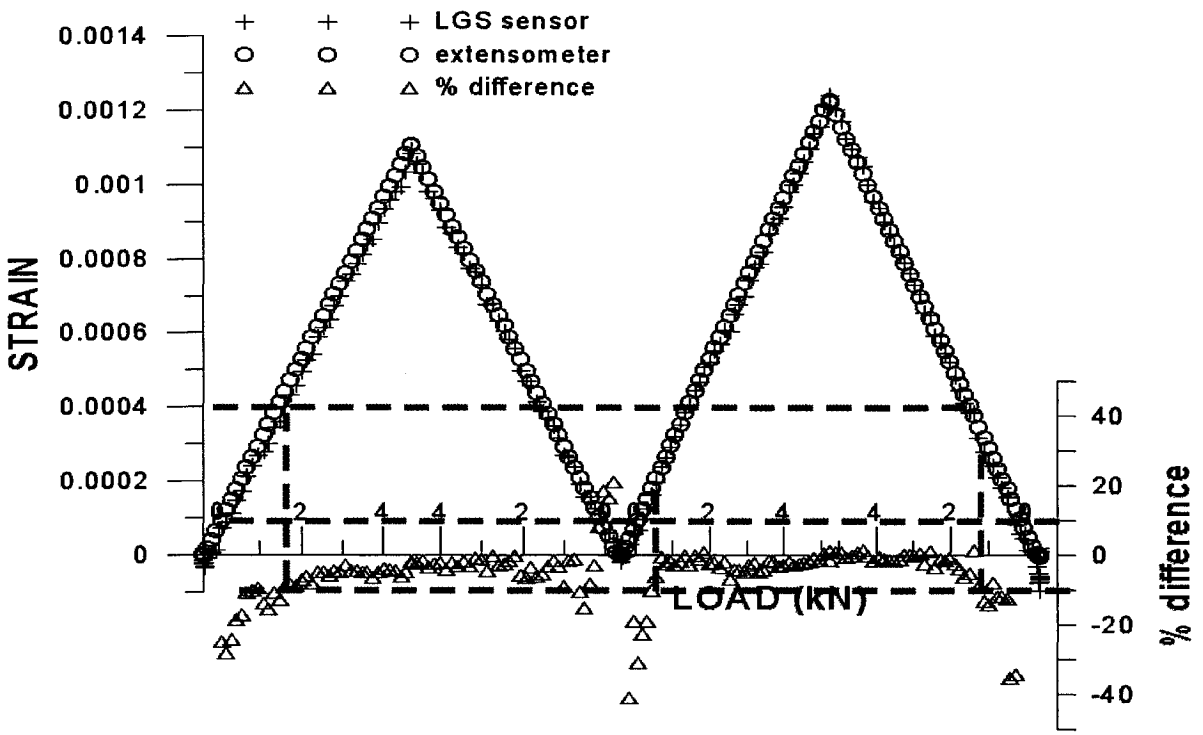

Figure 5.11: Strain of first sensor on the second specimen.

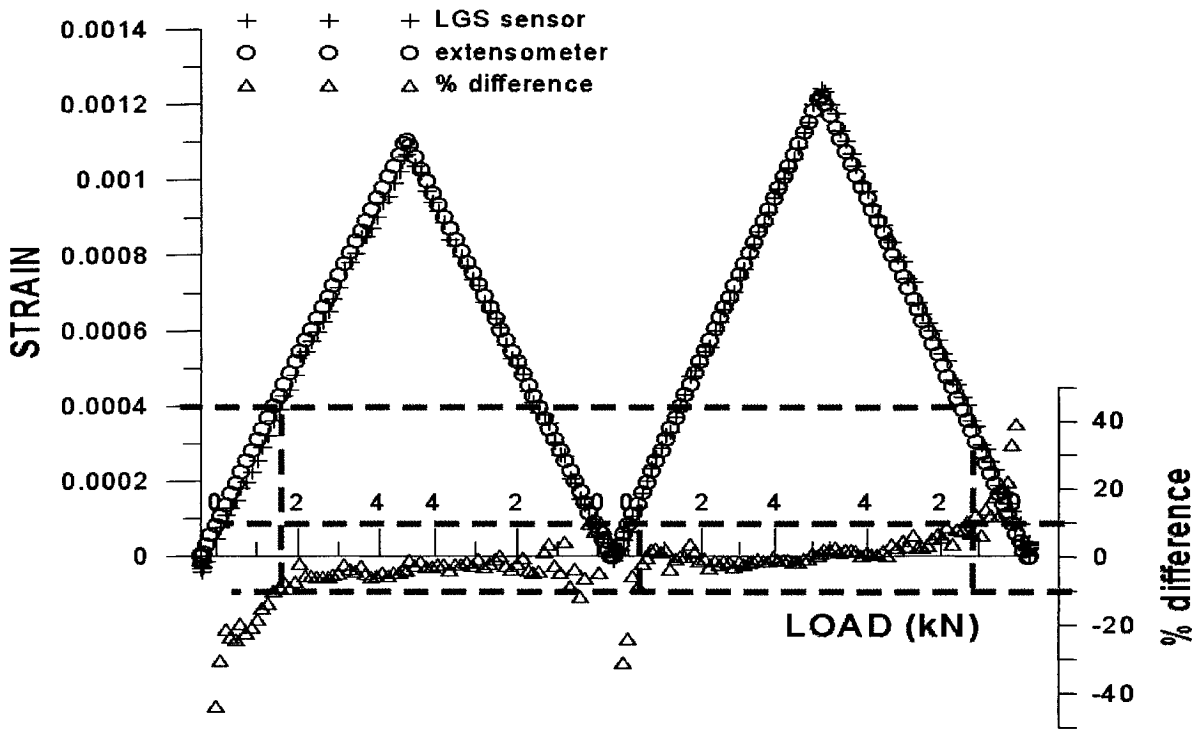

Figure 5.12: Strain of second sensor on the second specimen.

The strain data collected during the tests are presented in a different manner in the following four figures. The strain output of the extensometer is plotted against the strain output of the first and the second sensors on the first specimen in Figure 5.13 and Figure 5.14, respectively. The strain output of the extensometer is plotted against the strain output of the first and the second sensors on the second specimen in Figure 5.15 and Figure 5.16, respectively. In theory, the extensometer and the LGS sensor measure the same strain; therefore, linear graphs with unit slopes (i.e. having 45° angles with the x-axis) are expected. The results are tabulated in Table 5.2 along with their correlation coefficient (R^2) values. All four of these slopes are very close to unity. This proves the accuracy of the sensors. In all four graphs, as strain increases, less scatter of data points is observed. This is again attributed to the fact that the proposed LGS sensor has a high noise to signal ration at low strain levels.

Table 5.2: Slopes of the four sensors for strain versus strain graphs.

	Sensor	**Slope**	**R^2**	
Specimen #1	1	1.008	0.994	Figure 5.13
Specimen #1	2	0.985	0.995	Figure 5.14
Specimen #2	1	1.006	0.997	Figure 5.15
Specimen #2	2	0.992	0.995	Figure 5.16

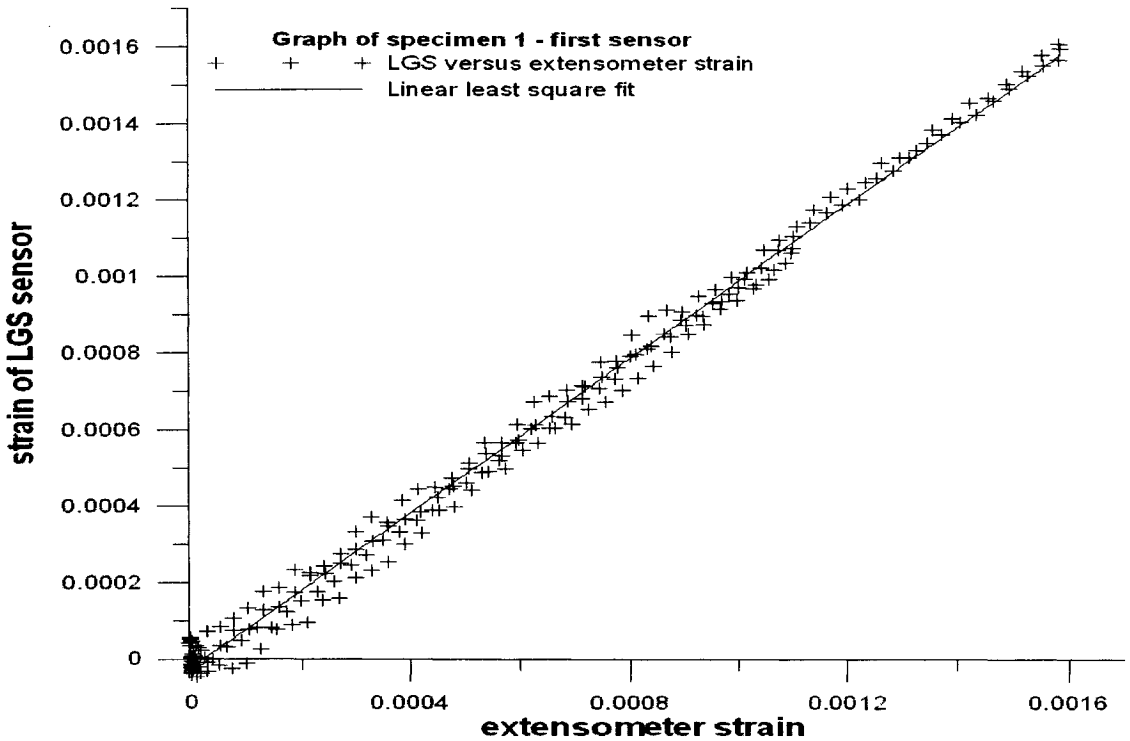

Figure 5.13: Strain versus strain graph for sensor 1-specimen 1.

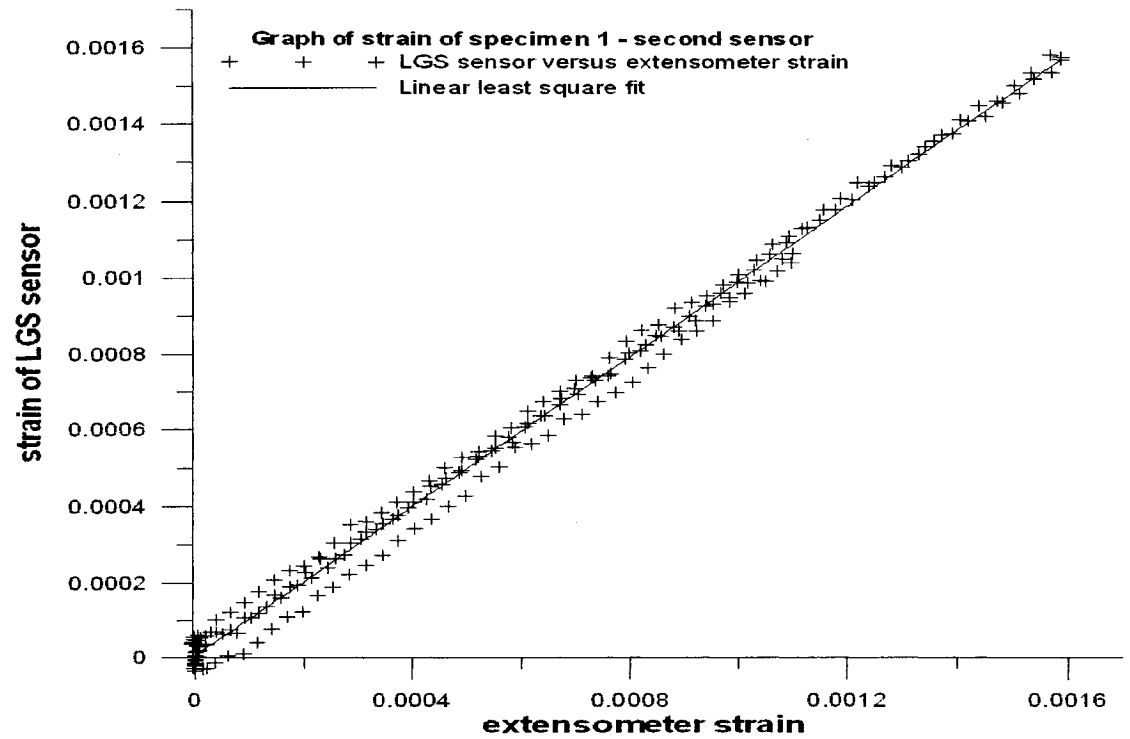

Figure 5.14: Strain versus strain graph for sensor 2- specimen 1.

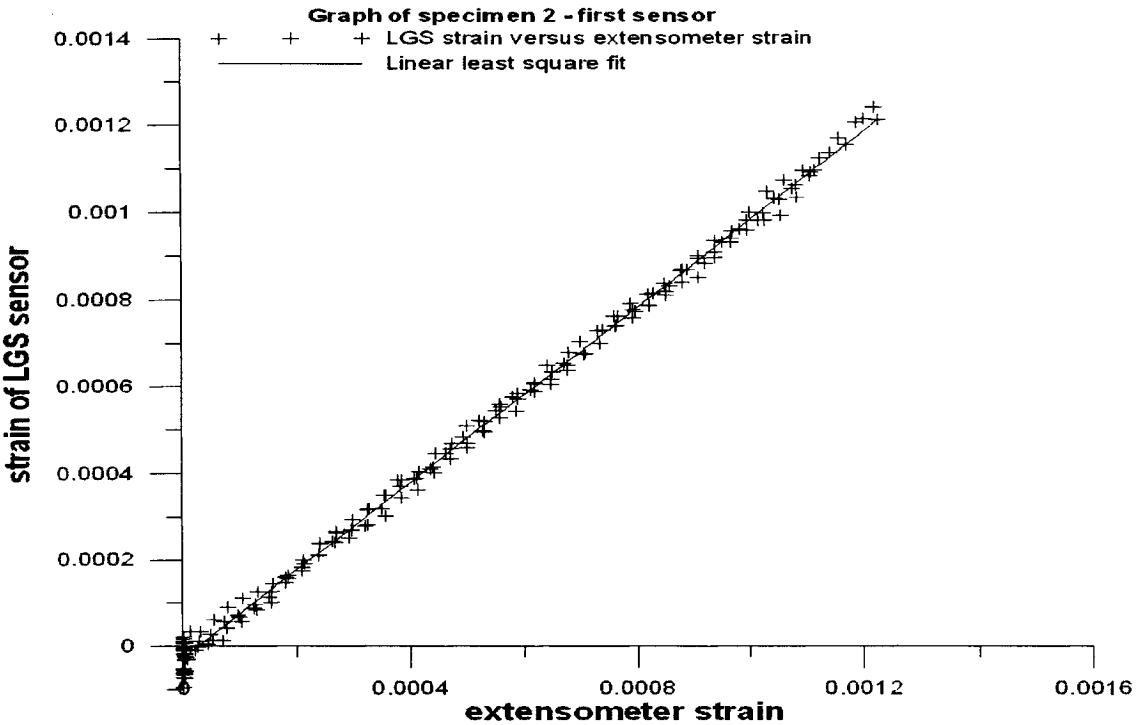

Figure 5.15: Strain versus strain graph for sensor 1- specimen 2.

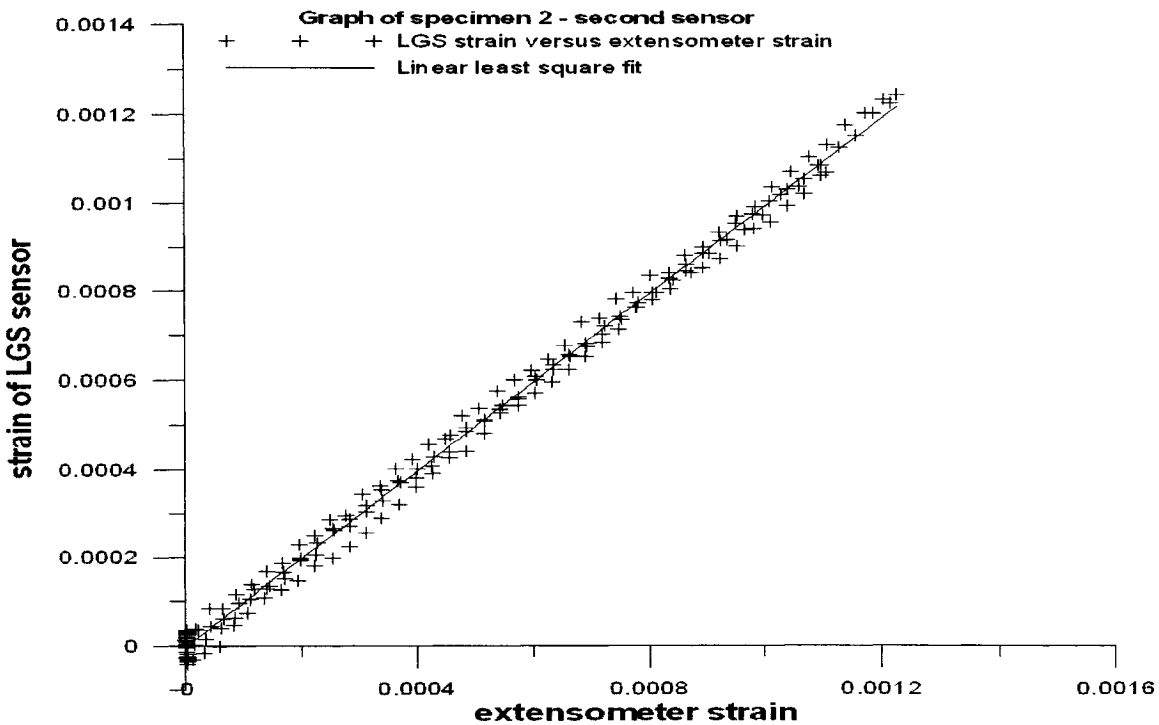

Figure 5.16: Strain versus strain graph for sensor 2- specimen 2.

5.3.1.b Tensile Test beyond the Elastic Range:

Figures 5.17 to 5.20 show the results of testing the specimens beyond the elastic range of the KA1 wire. In the graphs, results of the LGS sensors are plotted along with the results of the extensometer attached to the specimens.

Figure 5.17 and 5.18 show the results for the first and second sensors on the first specimen, respectively, while Figure 5.19 and 5.20 show the results for the second specimen.

At the beginning of the tests the specimens are loaded up to 600$\mu\epsilon$ and then unloaded twice. This is followed by an application of load corresponding to approximately 5500$\mu\epsilon$. At approximately 2400$\mu\epsilon$, a shift between the outputs of the LGS sensors and the extensometer is observed. This is a result of a decrease in the gage factor of the LGS sensors after the elastic region of the KA1 wire. The gage factors of the sensors in the plastic region are presented in Table 5.3. The average gage factor of the four specimens is found to be 1.9. The gage factor varies between 1.8 and 2.0.

The strain readings of the sensors after the elastic region are corrected using the calculated plastic region gage factor, and these results are also shown in the four figures as "modified LGS sensor". The results of the extensometer and the LGS sensors have less than 5% difference.

Table 5.3: Gage factors of the four sensors in the plastic region of the KA1 wire.

	Sensor Number	**Gage Factor(G)**	**R^2**	
Specimen #1	1	2.035	0.999	Figure 5.17
Specimen #1	2	1.838	0.999	Figure 5.18
Specimen #2	1	1.904	0.995	Figure 5.19
Specimen #2	2	1.927	0.993	Figure 5.20

Further increase in the applied load caused a failure of the shear epoxy in the pipe-grips at approximately 6300$\mu\epsilon$, and the test was stopped. The LGS sensors on the specimens are considered work-hardened as a result of the third loading. Calibration tests of the LGS sensors with work hardened KA1 wire can be conducted to determine the effect of work hardening on

the gage factor of the sensors. The first specimen was loaded for the fourth time as an initial step to this study. The change in gage factor is observed to take place approximately at 3500$\mu\epsilon$. A work hardened wire is considered permanently deformed. With reference to Figure 5.21, when such a wire is re-loaded, it has the same elastic modulus and follows a parallel path to the initial loading path, however the increased dislocation density in the material causes its gage factor to change. It is necessary to further the study for the work hardened sensor.

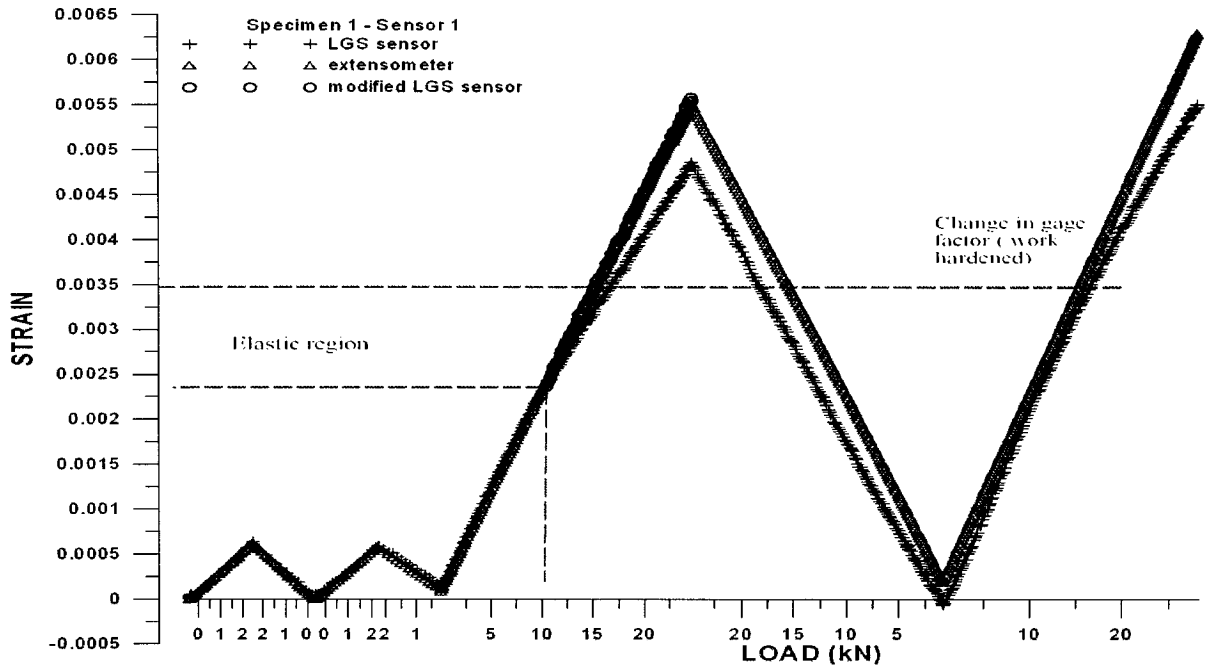

Figure 5.17: strain versus load graph of specimen 1 - sensor 1 in elastic and plastic regions.

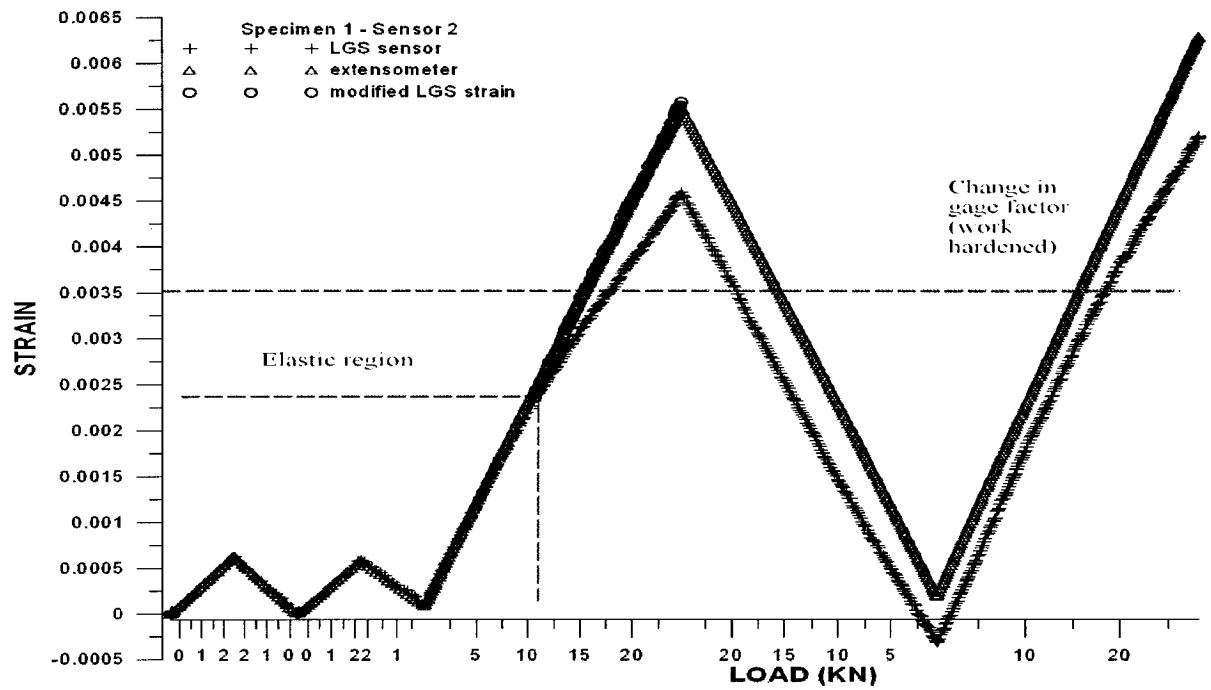

Figure 5.18: strain versus load graph of specimen 1 - sensor 2 in elastic and plastic regions.

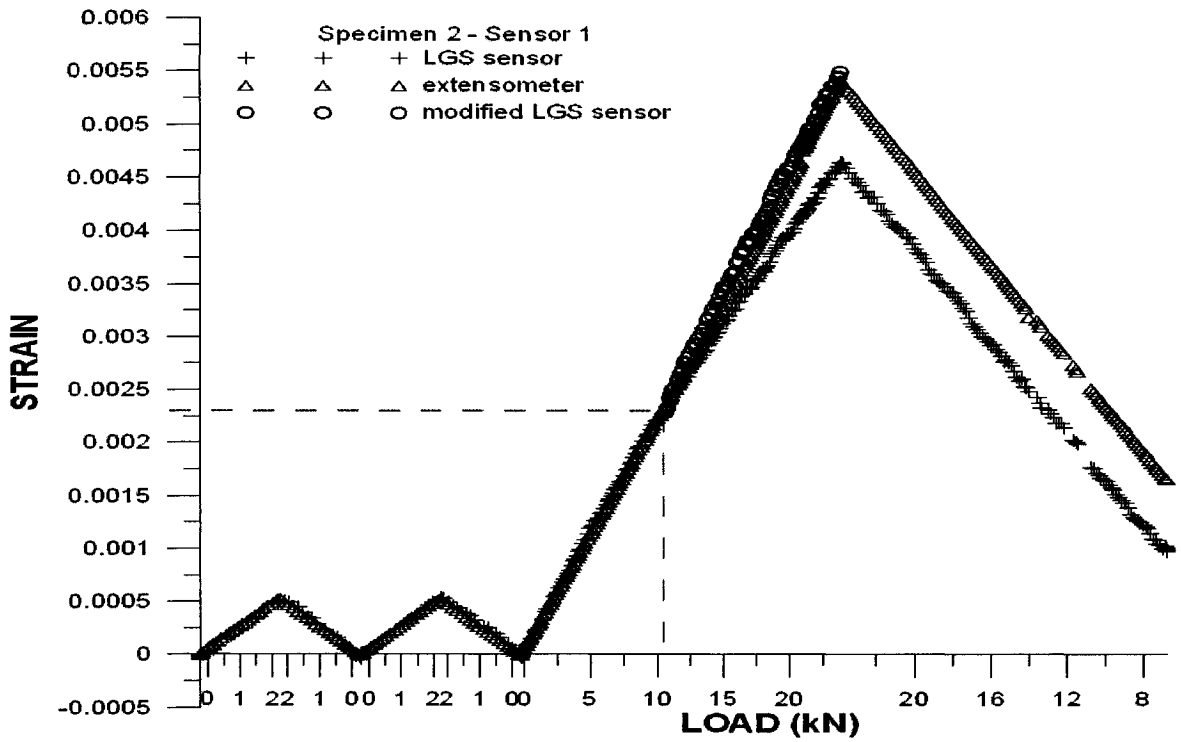

Figure 5.19: Strain versus load graph of specimen 2 - sensor 1 in elastic and plastic region.

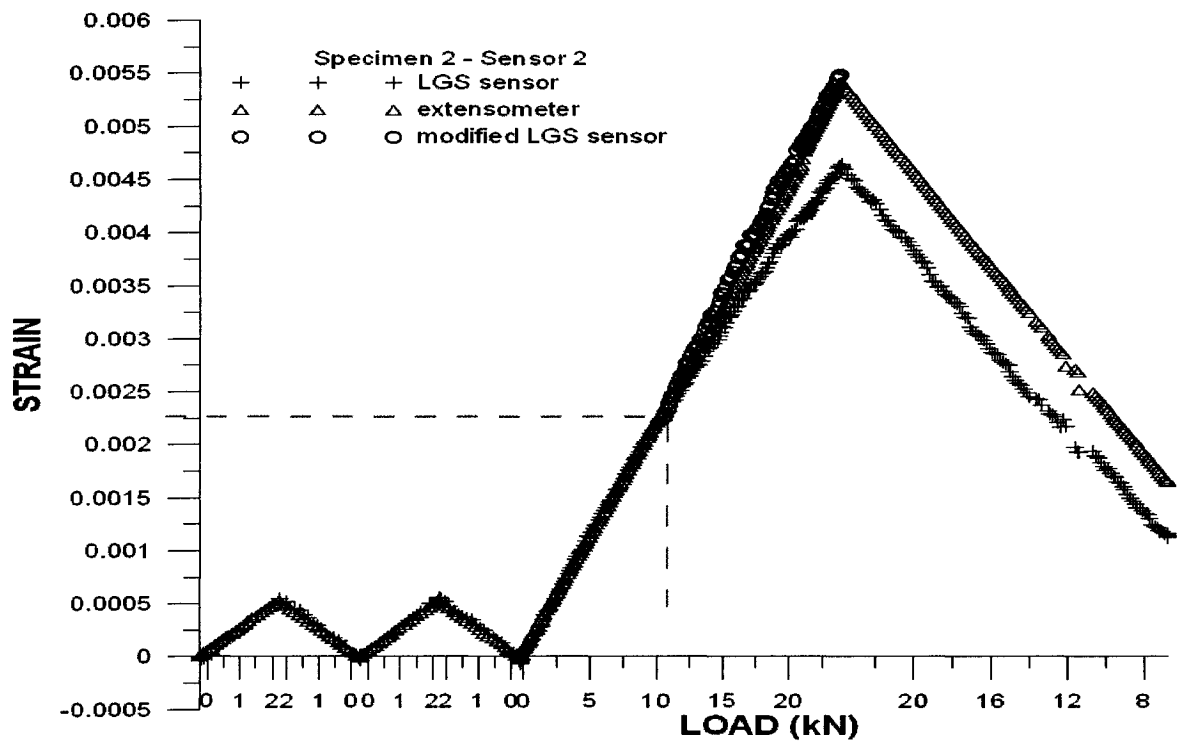

Figure 5.20: Strain versus load graph of specimen 2 - sensor 2 in elastic and plastic regions.

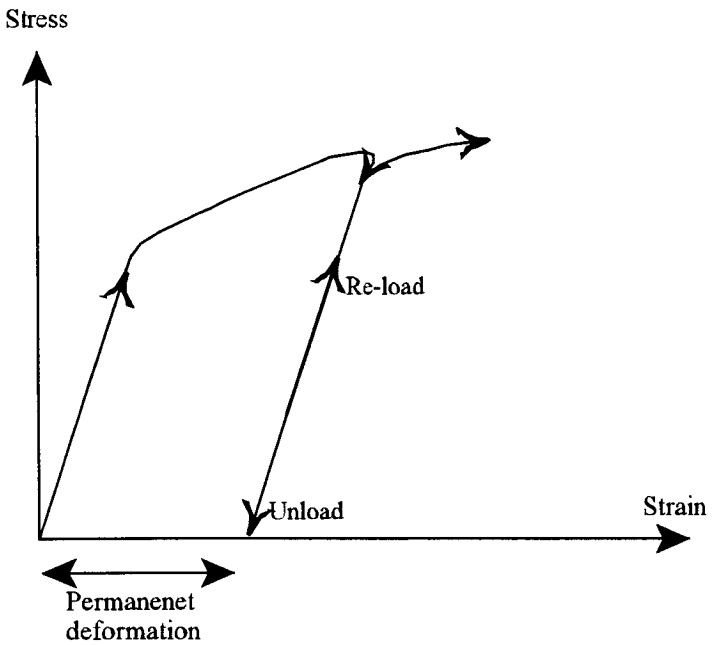

Figure 5.21: Schematic diagram of a loading after work-hardening.

5.3.2 Compression Specimen:

The specimen prepared for the compression test is loaded and unloaded twice with loads corresponding to approximately 610$\mu\epsilon$. This low load was used to avoid buckling of the specimen as the specimen is 30 cm long.

The plot of dR/R versus strain is shown in Figure 5.22. The slope of the cyclic loading plot gives a gage factor of 2.521 with a R^2 of 0.995.

The strain versus the load graph and the percent difference between the LGS sensor and the extensometer of the test are presented in Figure 5.23. The strain results of the LGS sensor follow the same shape as the extensometer strain, however the difference between the plots is more than that of the tensile test specimens. This is suspected to be due to the lack of lateral support during the experiment. In a concrete structure, the rebars are prevented from buckling by the surrounding concrete. It is believed that further experiments with lateral supports to prevent buckling can be done to investigate the characteristics of the sensor under compression loading.

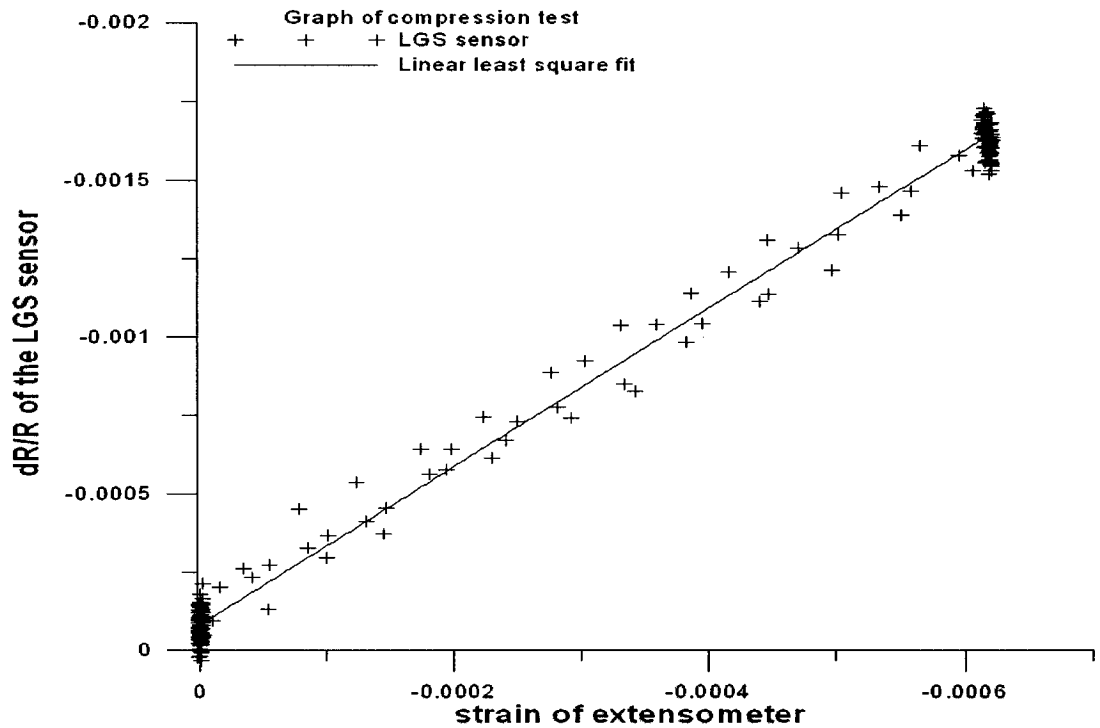

Figure 5.22: dR/R versus strain for the compression test specimen.

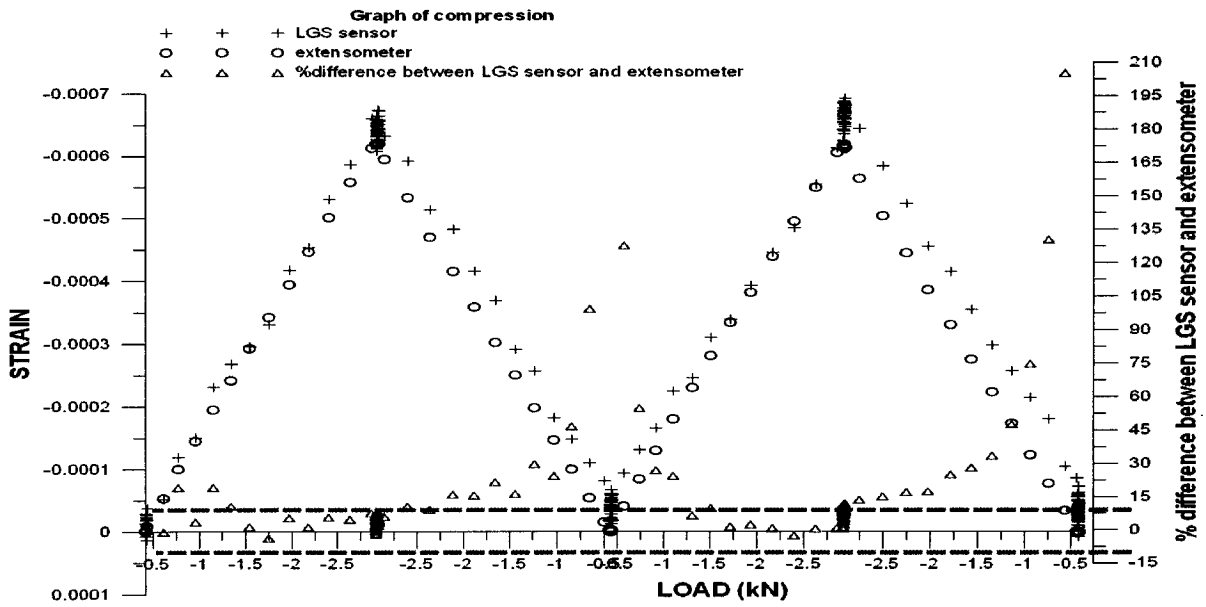

Figure 5.23: Strain versus load for compression test.

Chapter 6: Fabrication and In-Situ Concrete Test Results of the Proposed LGS Sensor

The proposed LGS sensor was mainly designed for the instrumentation of reinforced concrete structures; therefore, a concrete beam instrumented with LGS sensors was prepared and tested. The first section of the chapter presents the fabrication of the LGS sensors and the concrete beam. The second section presents the results of the test and the related discussions.

6.1 Fabrication of the Sensors and the Concrete Beam:

The LGS sensors for the in-situ concrete test were prepared following the same procedure used for the preparation of the prototypes (Chapter 5); however, unlike the calibration prototypes, the strain sensors that were prepared for the concrete test are composed of an array of six sensors on one carrier; i.e. 180 cm of carrier that has six LGS sensors with 30 cm long gage lengths.

The carrier was over-braided (one layer) with Kevlar fibers to protect the sensors from the harsh concrete environment. The fibers were Kevlar-49 (with 7000 denier), and braiding was a 45° angle braid. The over-braid was impregnated with resin. The braiding provides mechanical keying between the carrier and the concrete.

The carrier was then embedded into a 180 cm long, 13 cm wide, and 26 cm deep concrete beam (Figure 6.1a). The beam was reinforced with two steel rebars. The steel rebars were specifically chosen with the same diameter as the braided carrier to ensure that the strain sensors were at the same depth in the beam. Each rebar was instrumented with six equally spaced, commercial strain gages, ESG. A schematic diagram of the beam is shown in Figure 6.1 together with the placement of the two rebars and the fiberglass carrier inside the concrete beam. The ESG and the LGS sensors are placed facing the bottom of the beam. Every ESG sensor was located at the midpoints of each of the 30cm LGS sensors on the carrier. Since all the ESG sensors and the LGS sensors were on the same height and location, it is reasonable to expect comparable strain outputs from all three sensors that were at the same sections until the yield point of the rebars. The section number of the LGS and the ESG sensors are indicated in Figure 6.1. Throughout the discussion, the LGS sensors are designated as LGS-X, X being the section number of the sensor as indicated in Figure 6.1. The strain gages attached to the two steel rebars at these sections are indicated as ESG-Xa and ESG-Xb.

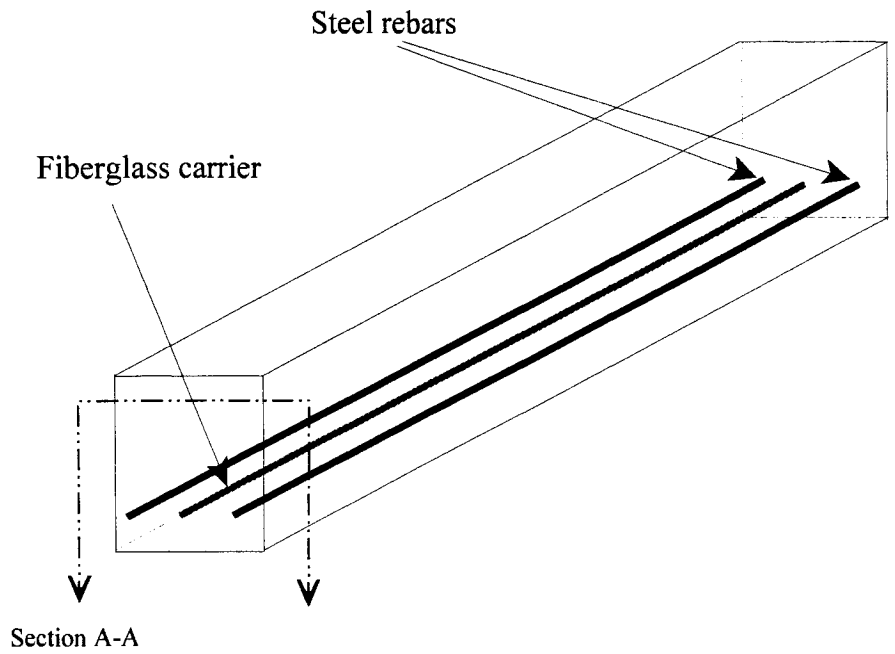

(a)

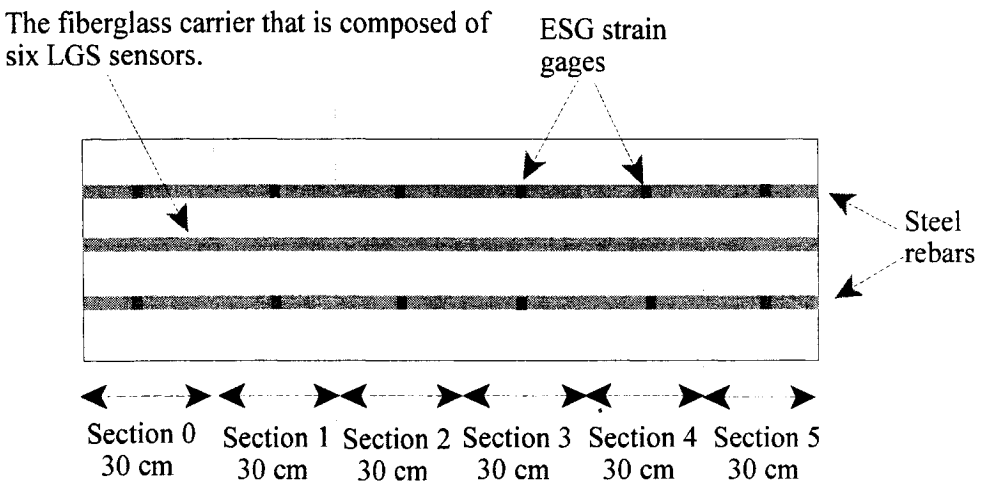

(b)

Figure 6.1: Schematic representation of the beam.
(a) Isometric view of concrete beam with steel rebars and the carrier that are located at the same height.
(b) Schematic representation of the beam.

6.2 Test Results:

Since load that was applied to the beam is transferred to the fiberglass carrier through the bond between the braiding and the carrier, a pull-out test was conducted to determine the shear bond between the fiberglass and the Kevlar braid. A fiberglass sample of the carrier was over-braided and embedded at a depth of 8cm deep into the pipe-grips filled with high shear modulus epoxy. The braid was serrated up to the fiberglass just outside the pipe. Figure 6.2 shows the results of this test. The original bond failed when the load on the specimen reached 28 kN at a strain of 0.0055ϵ. After the failure of the bond, the load that is carried by the specimen decreased to 2.8 kN and the fiberglass started to pull-out. The value of 2.8 kN is very low compared to 28 kN, and it applies a negligible amount of shear force between the fiberglass and the braid.

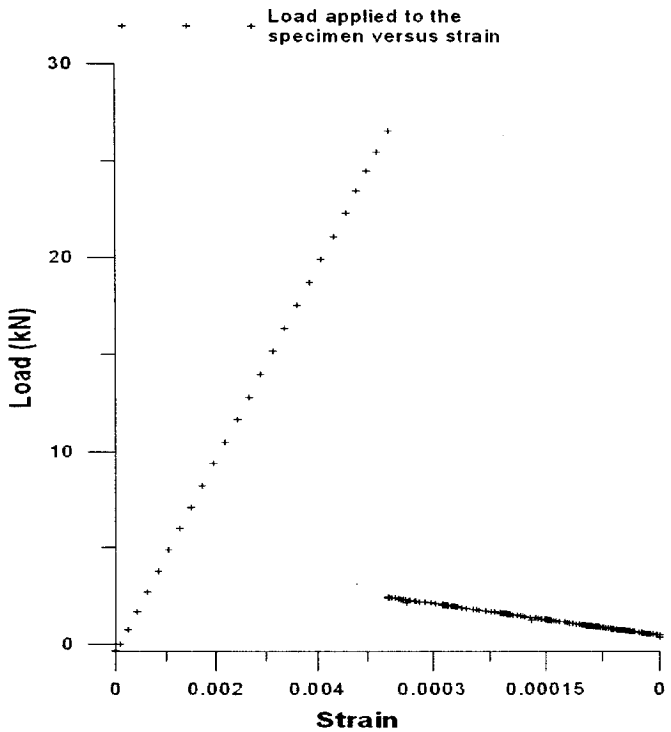

Figure 6.2: Load versus strain graph to determine the bond strength of fiberglass and braiding.

The concrete beam was tested using a three-point bend test (also known as simply supported beam with single midpoint loading). Under this type of loading, Section 2 and 3 are expected to experience higher strains than Section 1 and 4, and Section 0 and 5 are expected to experience the least strains.

In this experiment the strains were recorded automatically, while the load applied to the beam was recorded manually. As the applied load on the mid-point of the beam increases, the strain on the rebars and the carrier increase.

Figure 6.3 and 6.4 show the results for Sections 2 and 3, respectively. In both of these graphs, the ESG and the LGS sensors show similar results until the yield point of the rebars. At approximately 2300$\mu\epsilon$ (i.e. 0.0023 ϵ), the ESG sensors show a rapid increase in their values. These increases are not observed in the results of the LGS sensors. This increase occurs at the approximate yield point of the steel rebars. Figure 6.5 shows a schematic diagram of the stress-strain behavior of common reinforcement steels and the fiberglass carrier. With reference to this figure, rebars are expected to have a yield plato between approximately 0.002ϵ and 0.01ϵ. Hence, the ESG sensors that are attached to the steel rebars show the expected strain behavior in the yield region of the rebars. The yielding of the rebars continue until approximately 9500$\mu\epsilon$. With the increase of applied load on the beam, load carrying contribution of rebars decreases dramatically in the yielding plateau, and the rebars experience large strains with very small increases in the load carrying capacity. In this region, it is expected that the load that is applied to the beam is transferred to the fiberglass carrier of the LGS sensors, and the carrier acts as a reinforcement in the beam that is retarding the yielding of the steel rebars.

Figure 6.3 also shows the theoretical strain on the rebars. This is calculated using the load that is applied onto the beam. The theoretical strain is shown up to the yield point of the rebars to give the reader confidence about the strain results of both the ESG sensors and the LGS sensors.

The ESG sensors that are located at the exact same location on the two steel rebars are theoretically expected to give the same strain readings, however they show differences in the graphs. The figures also show the percent differences of strain data between the sensors until the yield point of the steel rebars. These three graphs show differences on the same section between

ESG-Xa and ESG-Xb, ESG-Xa and LGS-X, and ESG-Xb and LGS-X, respectively. Strains that are below 400$\mu\epsilon$ are ignored in these additional graphs for the reasons previously explained in Chapter 5.

Figure 6.3 and 6.4 show that the ESG-2a and ESG-2b sensors show 10% difference at all times, while the difference between ESG-3a and ESG-3b approaches zero as the load increases. The difference in the ESG sensors at Section 2 might be attributed to misalignment of sensors during pouring and curing of concrete. The differences between the ESG sensors and the LGS sensors are almost always 10% in both figures.

After the yield point of the rebars, LGS-2 and LGS-3 sensors show smaller strain results compared to that of ESG-2 and ESG-3 sensors, respectively. The LGS sensors measure global strains, and the ESG sensors measure local strains over their gage lengths. The strain differences that were observed between the two types of sensors are expected to be the result of this difference in their characteristics, and the bonding between the braiding and the carrier.

The expected reasons that cause the strain differences in the ESG and the LGS sensors are explained by using the sample calculations for Section 3. The ESG sensors on Section 3 show 0.0023ϵ when they indicate that the yielding of the rebars has started. At this strain the load that is applied onto the beam is 93.4 kN. This load creates a total tensile load of 152 kN on the reinforcements at the middle point of Section 3 (This is calculated from the moment created by 93.4 kN). The fiberglass carrier theoretically carries 11 kN at 0.0023ϵ. The remaining of the load is carried by the rebars, i.e. 141 kN. Since the rebars are yielding, they will not resist any additional load until the end of the yielding plateau.

When the load on the beam was increased to 101 kN, the tensile loads on the reinforcements were calculated as 128 kN, 166 kN, and 205 kN for the right end, middle, and left end of Section 3. Approximately 7 kN of the 128 kN is carried by the fiberglass carrier. Since the rebars will account for only 141 kN of the tensile load, the fiberglass theoretically carries 25 kN (166 kN - 141 kN = 25 kN), and 64 kN at the middle and right end of Section 3, respectively. Hence, when 101 kN load is applied onto the beam, the fiberglass carrier theoretically experiences 0.0132ϵ, 0.0051ϵ, and 0.0015ϵ at the right end, middle and left end of Section 3, respectively.

The average of these three strain values is 0.0066ϵ. Since LGS-3 sensor was measuring a global strain, the average of these three data can be accepted as the average strain on Section 3. The strain on the ESG sensors when the 101 kN is applied onto the beam is recorded as 0.0064ϵ. The small discrepancy between the two values (0.0066ϵ and 0.0064ϵ) confirms the validity of the above elaborated reasoning.

Since the bond between the carrier and the braiding is found to be lost at approximately 0.0055ϵ (with reference to Figure 6.2), the bonding between the left end and the middle point of the section is considered to fail at this loading (i.e. no load is transferred to the carrier). Hence, the strain measured by the LGS-3 is the strain that is between the middle and the right end of this section. The average of this section is theoretically calculated as 0.0042ϵ. The experimental measurement of LGS-3 at this load is found as 0.0027ϵ from the graph. The length of braid-fiberglass bonding that has not failed can be slightly different in the experiment than it is calculated theoretically, and the difference in the experimental and theoretical strain results can be a result of this.

In the calibration tests, the prototypes were tested up to 5500$\mu\epsilon$ (Chapter 5). The results of the LGS sensors that were used in the beam test includes strain results that is above 5500$\mu\epsilon$. Although the data that is above this strain value is not confirmed experimentally, it is important to present here, because it shows that the LGS sensors survived the test and they did not fail.

The beam experienced an under-reinforced failure, because the rebars yielded before the crushing of concrete. The loading of the concrete beam was stopped at 143 kN. After unloading the beam, it was loaded again. The second loading is discussed later in this chapter.

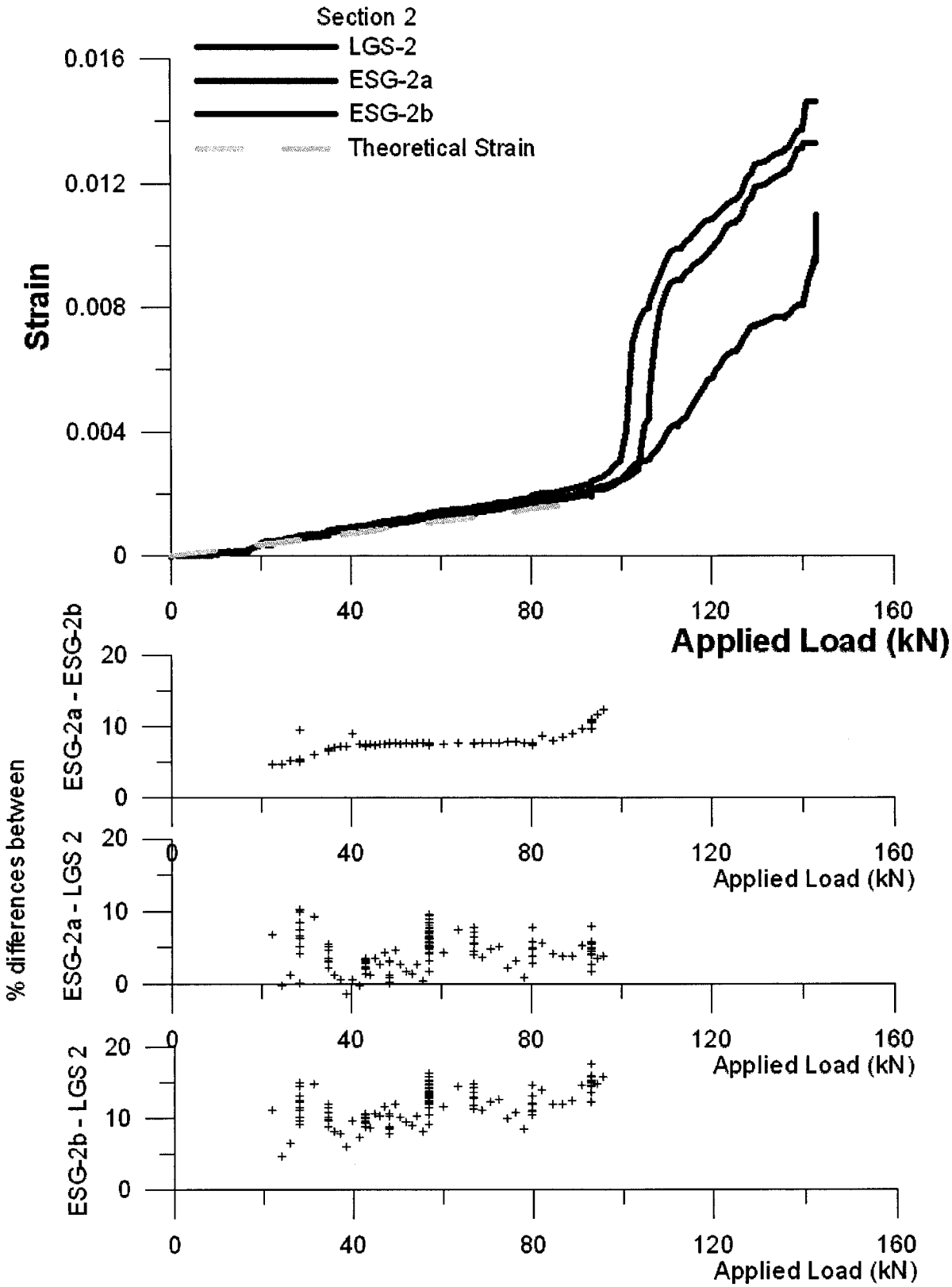

Figure 6.3: Load versus strain for Section 2.

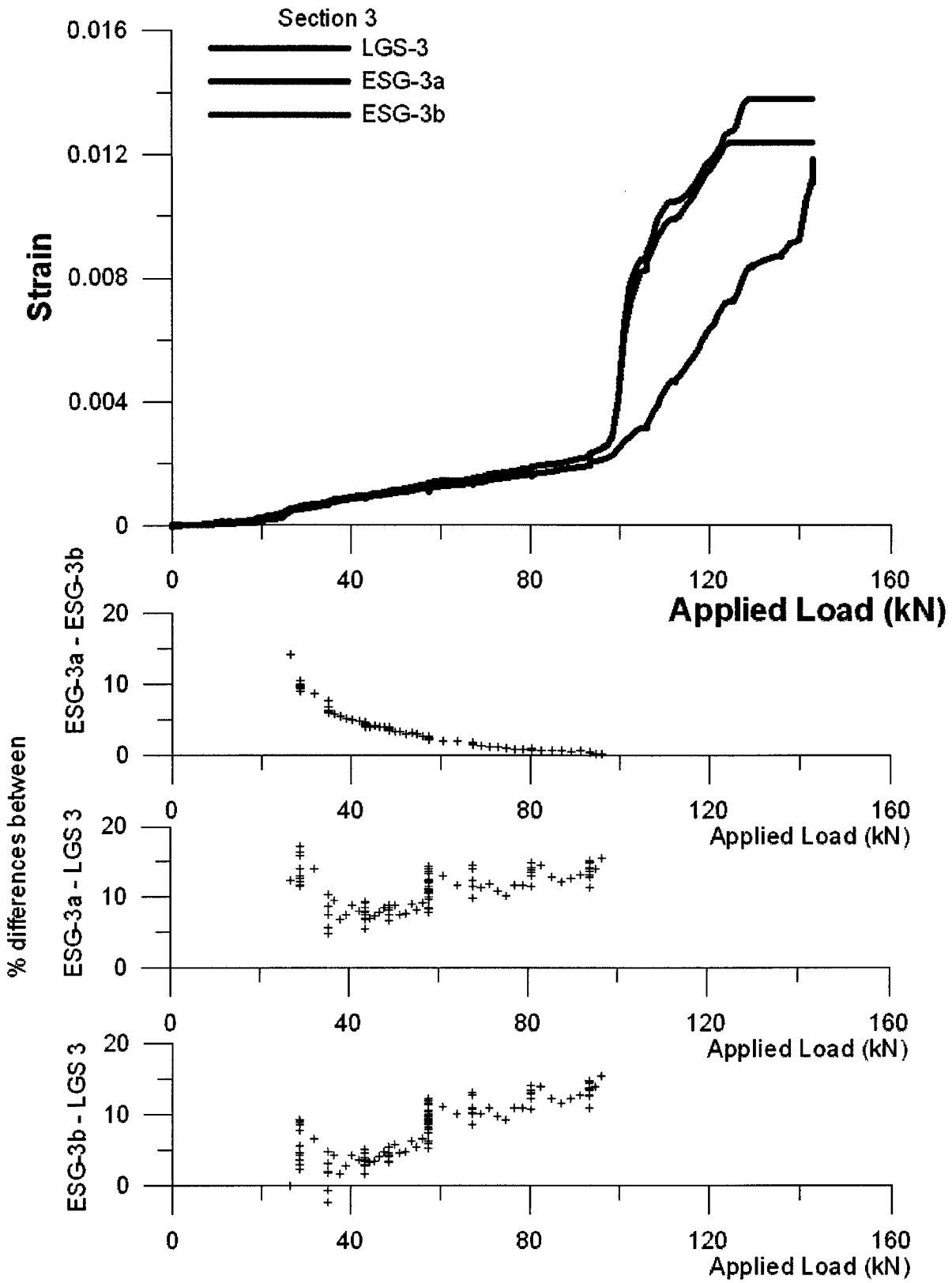

Figure 6.4: Load versus strain for Section 3.

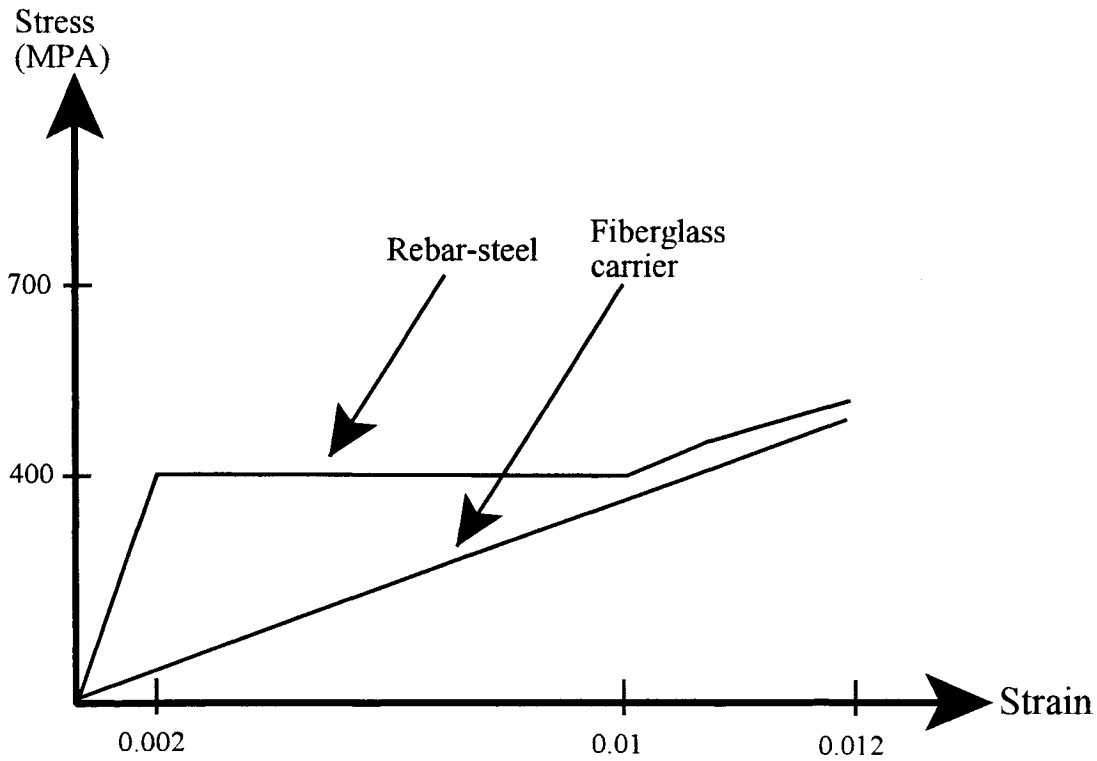

Figure 6.5: Theoretical stress-strain curve for the rebar-steel and the fiberglass. (Up to 0.012 strain)

Figure 6.6 and 6.7 show the results for Section 1 and Section 4, respectively. The results confirmed the initial expectations for the first and the fourth sections, i.e. smaller strain magnitudes are observed in the ESG and the LGS sensors compared to the second and the third sections.

LGS-1 and LGS-4 sensors show higher strain results compared to the ESG sensors after 125 kN load on the beam. This behavior is expected to be the result of the gage length differences of the LGS and the ESG sensors.

Section 1 is used for the explanation of this phenomena. When the load on the beam is 125 kN, the tensile loads on the reinforcements are 72 kN, 115 kN, and 162 kN on the left end, middle, and right end, respectively. The fiberglass carrier supports 5 kN of 72 kN, 8 kN of 115 kN and 21 kN of 162 kN at these locations. As a result of these calculations, at these points the fiberglass carrier theoretically experiences 0.00108ϵ, 0.00172ϵ, and 0.00435ϵ, respectively.

The average of the strains at these three points is 0.0024ϵ, as compared 0.0021ϵ found experimentally. The ESG sensors measure approximately 0.0018ϵ at this section. The difference seen as a result of this calculation (0.0024ϵ versus 0.0018ϵ) is believed to be the reason for smaller strains measured by the ESG sensors compared to the LGS sensors.

The percent differences of the ESG sensors in both of the figures are found to be approximately 10%. In most of the cases the differences between the ESG sensor and the LGS sensors are found to be low until the start of yielding of the rebars at 93 kN. After this load, the beam experiences excessive deformation due to yielding of the steel rebars.

Figure 6.8 and 6.9 show the results of Section 0 and 5, respectively. Due to their locations, these gages experience the least strains. Strains below 400$\mu\epsilon$ are ignored due to the high noise to signal ratio. Although the ESG and the LGS results are similar, less agreement is observed. Figure 6.8 shows that LGS-0 results match with those of ESG-0a results. Figure 6.9 shows that LGS-5 results are similar to those of ESG-5a and ESG-5b results.

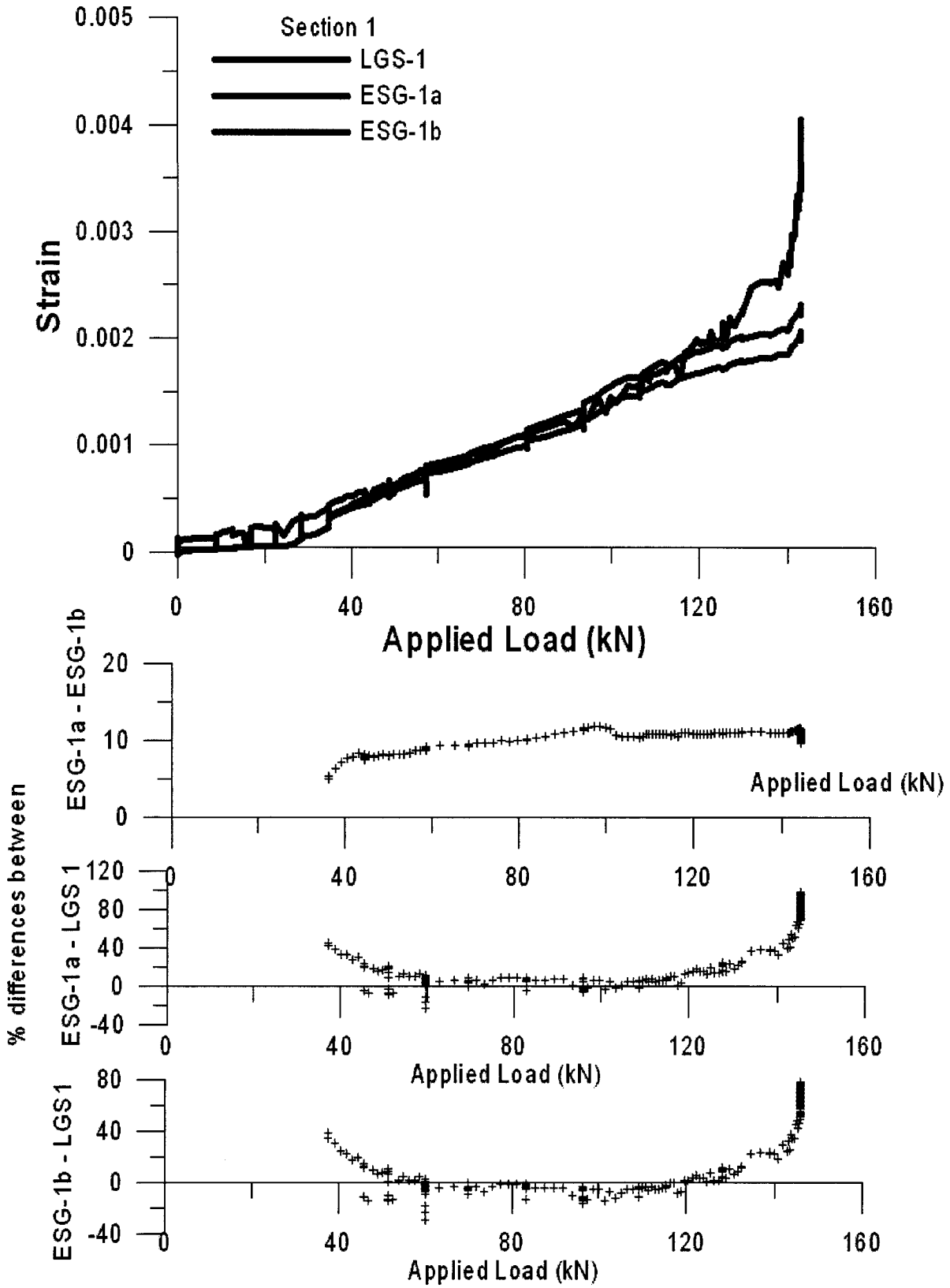

Figure 6.6: Load versus strain for Section 1.

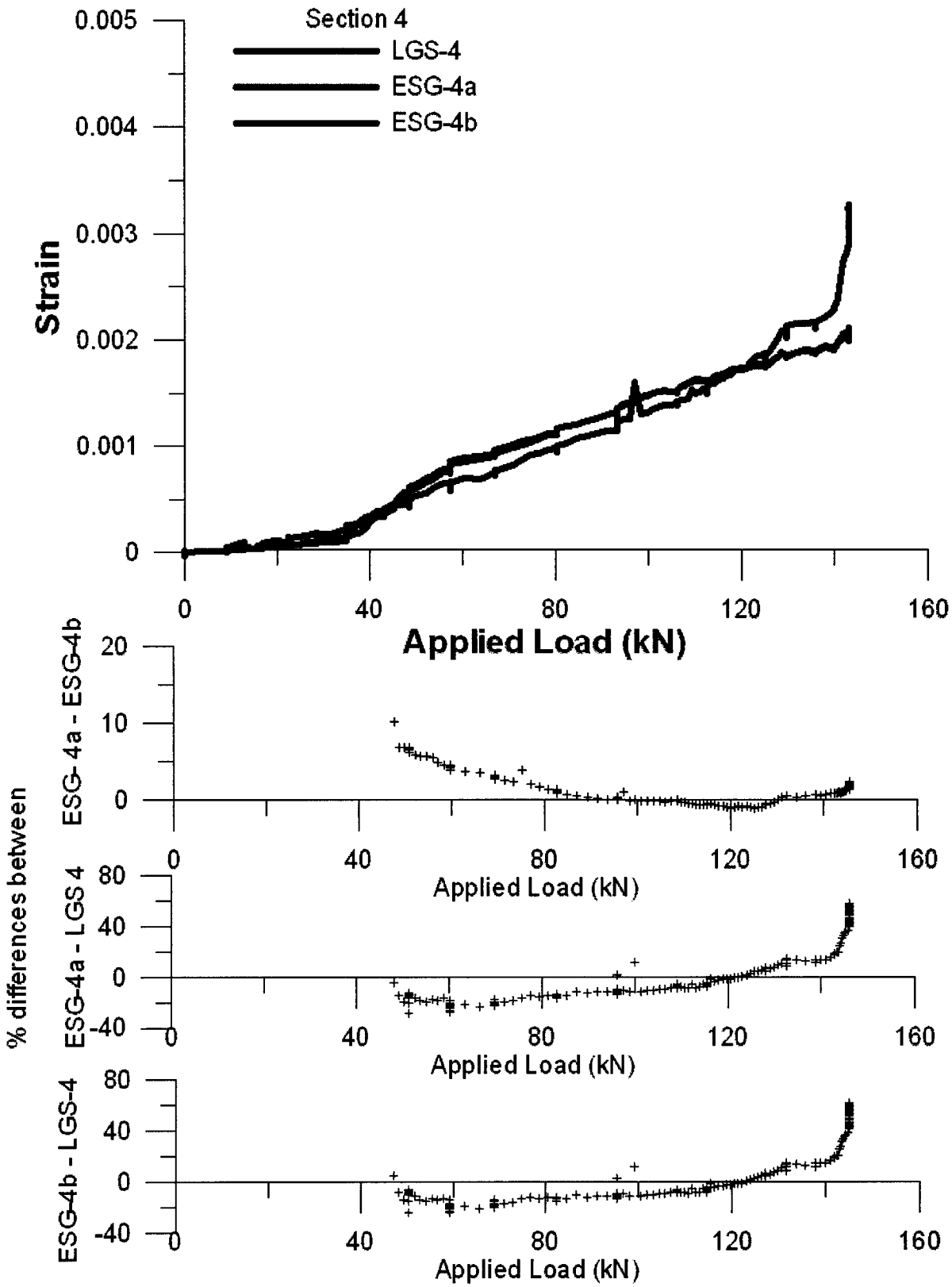

Figure 6.7: Load versus strain for Section 4.

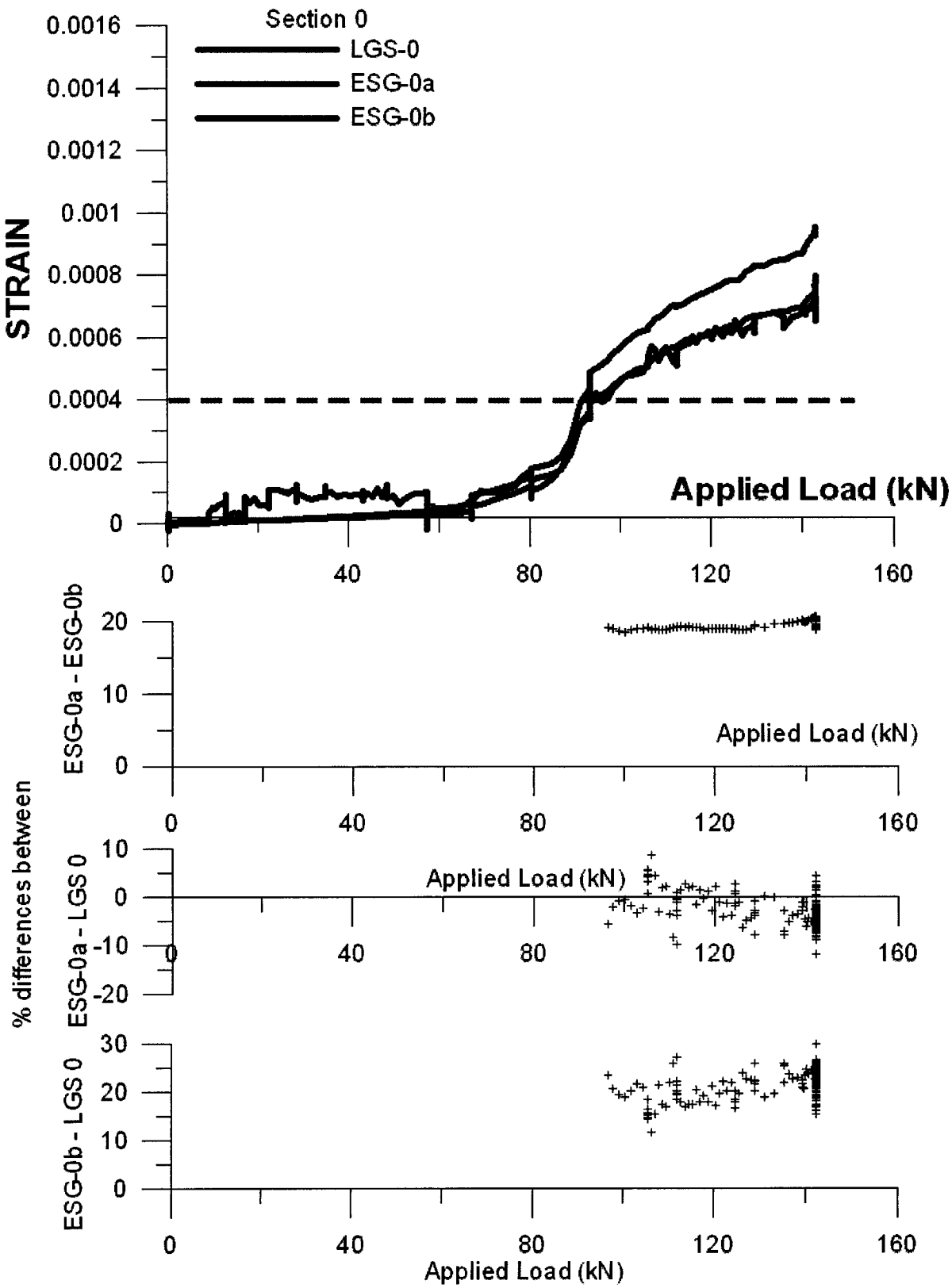

Figure 6.8: Load versus strain for Section 0.

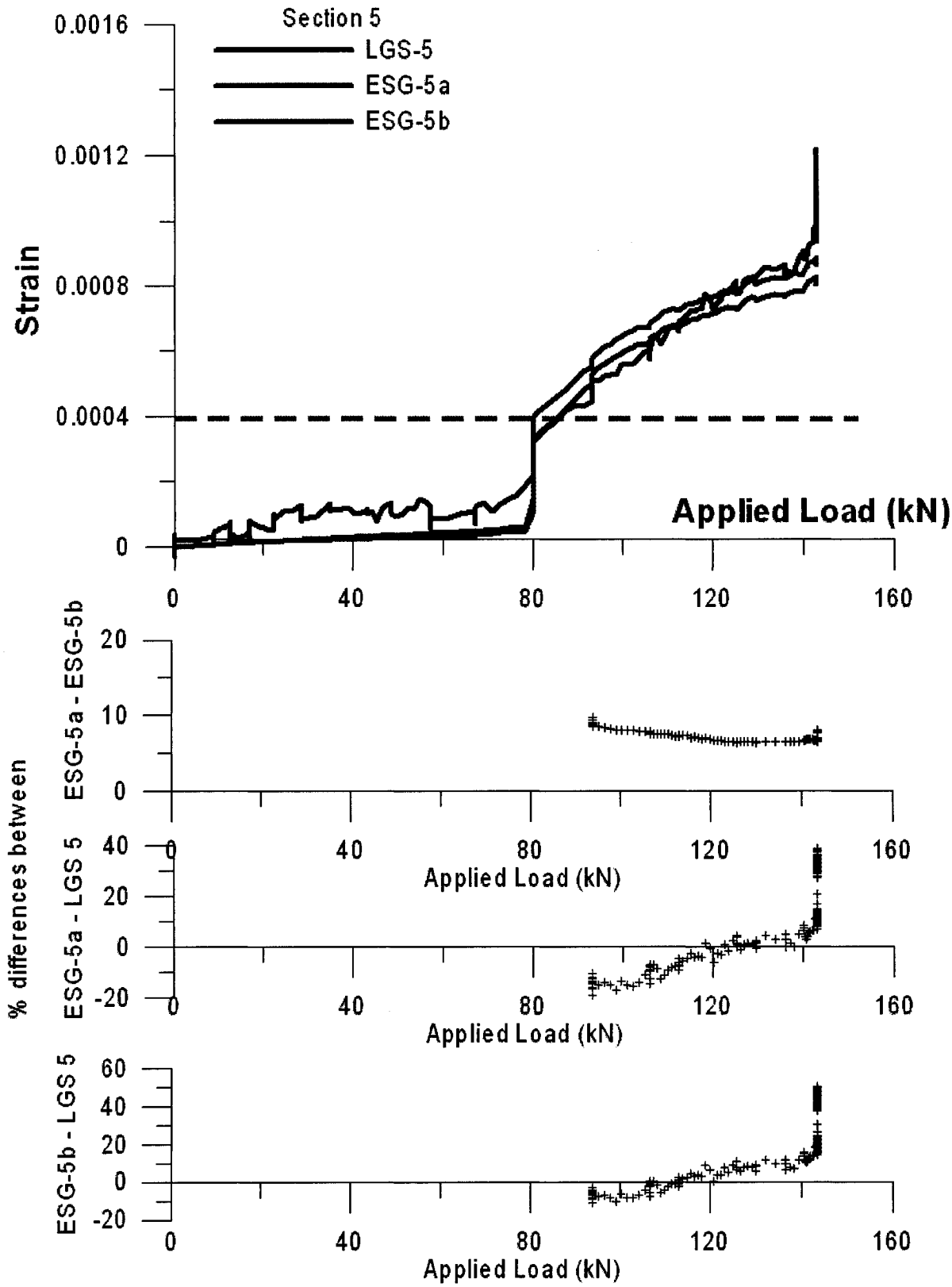

Figure 6.9: Load versus strain for Section 5.

Tables 6.1 to 6.5 shows the theoretical strain calculations as well as experimental findings of the LGS and the ESG sensors at Sections 3, 4, and 5 for five different loadings on the concrete beam. The theoretical strain of the LGS sensors are calculated as the average of the points of the left end, middle, and right end of a section. In almost all of the cases, experimental strain findings of the LGS and ESG, and theoretical strain findings of the LGS and ESG sensors are similar. The differences that are observed between the theoretical and experimental findings of both types of sensors may be attributed to the approximations used in the concrete beam calculations. One of these is the Rectangular Stress Block approximation that assumes a constant stress contribution of concrete in the compression zone of the beam, where in reality that contribution has a parabolic shape. Hence, it has a direct effect on the amount of tensile force transferred to the reinforcements in a concrete beam. The differences can also be attributed to the concrete strength, and elastic modulus of rebar steel that have effect on the calculations. Also non-perfect bonding between reinforcements (steel rebar and the braided fiberglass carrier) and concrete may contribute to the differences between the theoretical and experimental strain findings.

Table 6.1: Section strains when the beam loading is 48550 N.

		LOAD 48550N				
		LGS	LGS	LGS	ESG	ESG
		Point strain	Average strain	Experimental strain result	Calculated strain	Experimental strain result
Section 3	right end	0.00068				
	middle	0.00087	0.00088	0.00102	0.00087	0.00108
	left end	0.00108				
Section 4	right end	0.00031				
	middle	0.00050	0.00049	0.00050	0.00050	0.00056
	left end	0.00068				
Section 5	right end	0.00000				
	middle	0.00012	0.00014	N/A (lower than 400$\mu\epsilon$)	0.00012	0.00004
	left end	0.00031				

Table 6.2: Section strains when the beam loading is 67110 N.

		LOAD 67110N				
		LGS	LGS	LGS	ESG	ESG
		Point strain	Average strain	Experimental strain result	Calculated strain	Experimental strain result
Section 3	right end	0.00095				
	middle	0.00120	0.00122	0.00139	0.00120	0.00152
	left end	0.00150				
Section 4	right end	0.00042				
	middle	0.00068	0.00068	0.00076	0.00068	0.00091
	left end	0.00095				
Section 5	right end	0.00000				
	middle	0.00017	0.00020	N/A (lower than 400με)	0.00017	0.00005
	left end	0.00042				

Table 6.3: Section strains when the beam loading is 80340 N.

		LOAD 80340N				
		LGS	LGS	LGS	ESG	ESG
		Point strain	Average strain	Experimental strain result	Calculated strain	Experimental strain result
Section 3	right end	0.00114				
	middle	0.00147	0.00216	0.00168	0.00147	0.00194
	left end	0.00388				
Section 4	right end	0.00051				
	middle	0.00083	0.00083	0.00101	0.00083	0.00117
	left end	0.00114				
Section 5	right end	0.00000				
	middle	0.00020	0.00024	N/A (lower than 400με)	0.00020	0.00024
	left end	0.00051				

Table 6.4: Section strains when the beam loading is 93400 N.

		LOAD 93400N				
		LGS	LGS	LGS	ESG	ESG
		Point strain	Average strain	Experimental strain result	Calculated strain	Experimental strain result
Section 3	right end	0.00134				
	middle	0.00172	0.00280	0.00205	0.00172	0.00234
	left end	0.00974				
Section 4	right end	0.00059				
	middle	0.00096	0.00096	0.00123	0.00100	0.00131
	left end	0.00134				
Section 5	right end	0.00000				
	middle	0.00024	0.00028	0.00049	0.00024	0.00051
	left end	0.00059				

Table 6.5: Section strains when the beam loading is 101000 N.

		LOAD 101000N				
		LGS	LGS	LGS	ESG	ESG
		Point strain	Average strain	Experimental strain result	Calculated strain	Experimental strain result
Section 3	right end	0.00145				
	middle	0.00510	0.00422	0.00273	0.00658	0.00640
	left end	0.01320				
Section 4	right end	0.00063				
	middle	0.00102	0.00103	0.00135	0.00102	0.00151
	left end	0.00145				
Section 5	right end	0.00000				
	middle	0.00025	0.00029	0.00056	0.00025	0.00061
	left end	0.00063				

After the beam was unloaded it was reloaded. The second loading was done to observe the behavior of the proposed sensors on damaged structures, such as in the case of an earthquake.

The ESG and the LGS values of the second and the third sections are shown in Figure 6.10 and 6.11, respectively. Good agreements of the results between the ESG and the LGS sensors are observed. After approximately 100kN the ESG data remained unchanged as seen in Figure 6.10, or produced no signal as seen in Figure 6.11 (possibly due to failure of the ESG sensors); however, as the loading of the beam increased the proposed LGS sensors continued to provide data. The test was stopped when crushing of concrete was observed.

Figure 6.12 and 6.13 present the ESG and the LGS outputs from the first and the fourth sections. The results from both types of sensors at Section 4 are similar. In Section 1, although the ESG and the LGS sensors follow the same trend, LGS-1 sensor show lower strain values compared to ESG-1a and ESG-1b.

Figure 6.14 and 6.15 show the strain data collected from the ESG and the LGS sensors at Section 0 and 5, respectively. The strain results at this section remained below 400$\mu\epsilon$. Further investigation for such small strain levels for in-situ concrete applications is required.

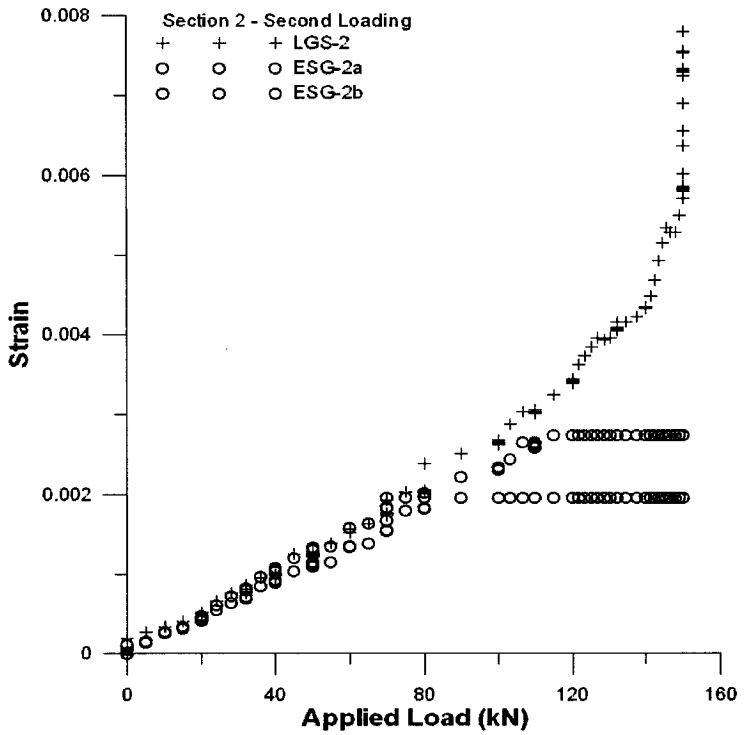

Figure 6.10: Load versus strain for second loading of Section 2.

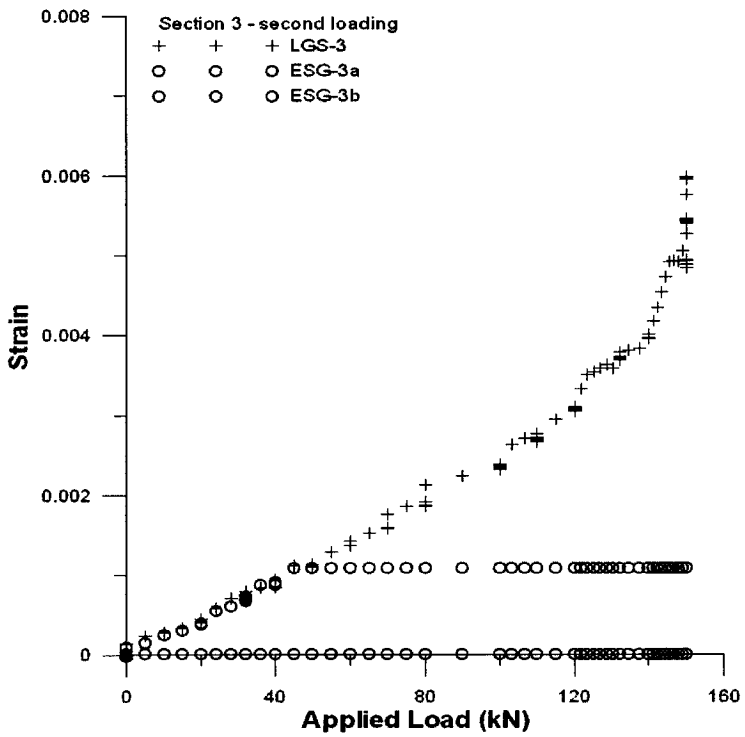

Figure 6.11: Load versus strain for second loading of Section 3.

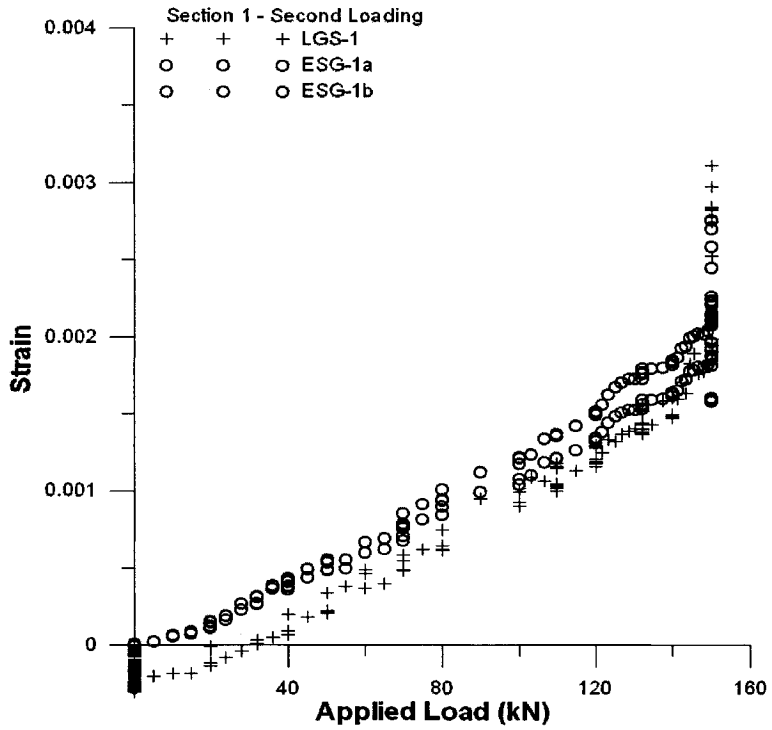

Figure 6.12: Load versus strain for second loading of Section 1.

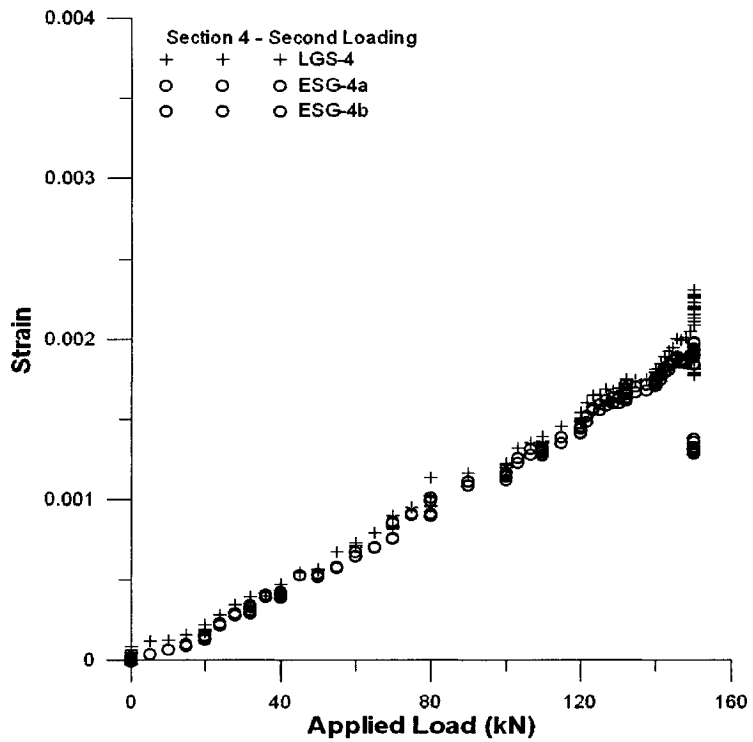

Figure 6.13: Load versus strain for second loading of Section 4.

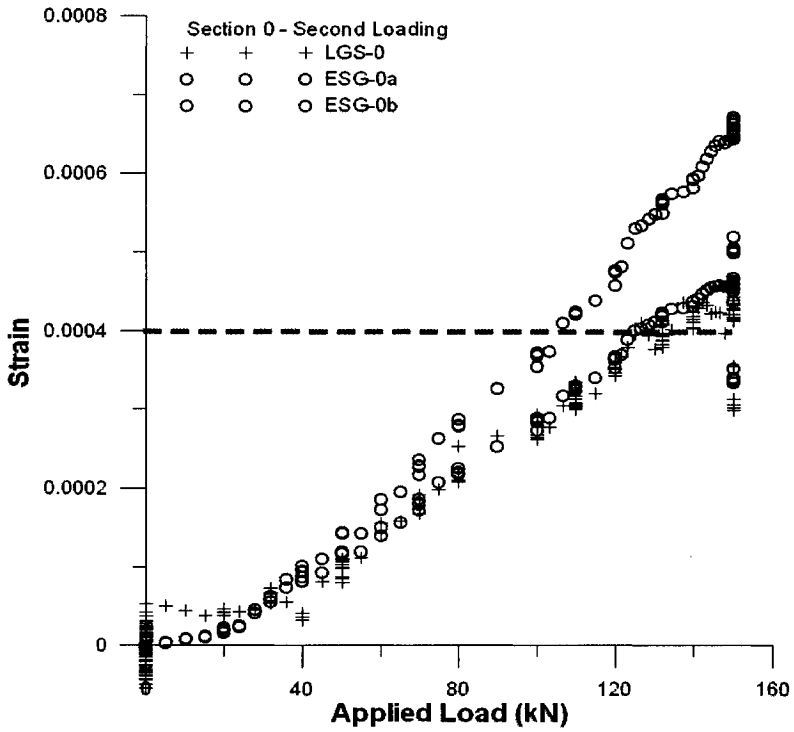

Figure 6.14: Load versus strain for second loading of Section 0.

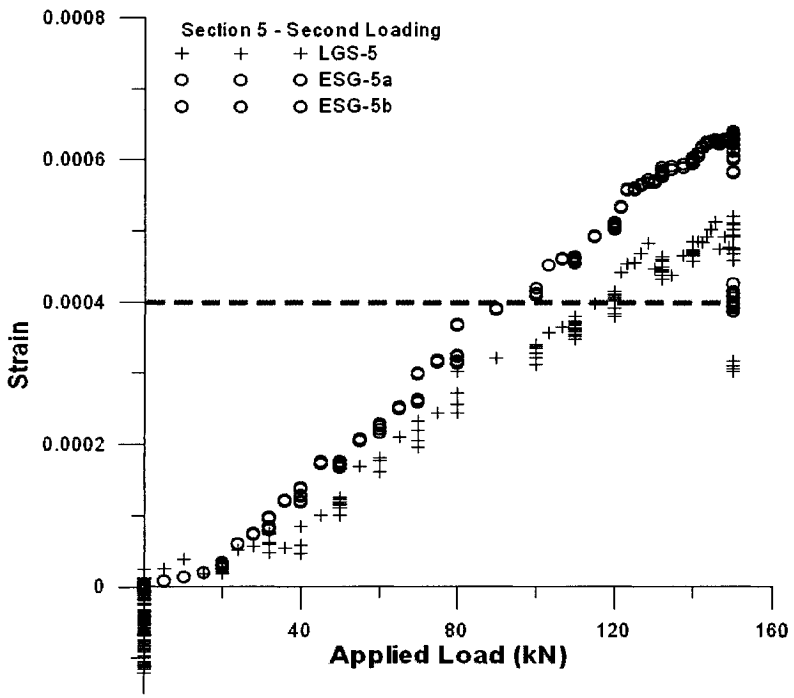

Figure 6.15: Load versus strain for second loading of Section 5.

Chapter 7: Conclusions and Recommendations for Future Work

A strain sensor that is an alternative to the ones that are available for reinforced concrete structures is designed and tested in this thesis. The new sensor is inexpensive, has long gage length, and has the ability to monitor the integrity of elements of structures. The following conclusions arise from the thesis.

The new sensor uses the commonly known phenomena of the increase of resistance of a wire as it stretches to measure the strain. The initial resistance of the strain sensing wire used for the sensor must be maximized in order to minimize the noise to signal ratio in the experiments. The resistance of a wire is a function of its resistivity, length and cross sectional area. For this development stage, KA1 wire with 0.18 mm diameter is chosen as the strain sensing wire due to its high resistivity. The gage factor of bare KA1 wire is found experimentally as 2.9.

A length of the KA1 wire is segmented into multiple sensors by soldering thin copper wire taps at distances from each other. The copper wires are pre-insulated along its length with varnish. Measuring the change in resistance between the taps gives an indication of the strain experienced by each segment of the strain sensing wire.

Prototypes of the LGS sensors are fabricated by embedding the prepared wire into a carrier for protection and electrical insulation purposes. These prototypes are then tested under tensile loadings. As a result of these tests, gage factors of the LGS sensors within the elastic region and the plastic region of the strain sensing KA1 wire are found as 2.6 and 1.9 respectively.

The load that is applied to the sensors in the tensile tests are transferred to the strain sensing wire through the carrier. Hence, the gage factor of the bare KA1 wire and the LGS sensor are different (2.9 versus 2.6) because of the differences between the elastic modulus of the carrier and the strain sensing wire.

The gage factor is a function of geometrical changes as well as electrical changes in the atomic level for the elastic region of the KA1 wire, but when the wire enters the plastic region the electrical changes become negligible as a result of increasing dislocation density, and the geometrical changes dominate. Hence, this explains the differences between the gage factors in the elastic and plastic region (2.6 versus 1.9).

Results from the LGS sensors are compared to that of an extensometer that was attached to the prototypes during the tests. The LGS sensors that are tested under tension were able to measure strains above 400$\mu\epsilon$ with less than 10% difference compared to the extensometer strain.

LGS sensor that is tested under compression did not provided reliable results, but they had similar trends to those from the extensometer. This is expected to be the result of lack of lateral support in the compression specimen. In actual usage, such lateral support is naturally provided by the surrounding concrete.

An array of six LGS sensors on a single carrier is prepared, and over-braided with Kevlar fibers to create mechanical keying to the concrete. This array of LGS sensors are used to instrument a concrete beam that is reinforced with two steel rebars. The steel rebars are also instrumented with commercial electrical strain gage (ESG) sensors. This is done to compare the strain readings of the two different types of sensors. The rebars and the LGS sensors are embedded at the same depth in the beam.

The beam was tested under three point bend test (also known as the simply supported single-midpoint loading). The in-situ concrete test results of the LGS sensors showed that the sensors worked well until the yield point of the steel rebars in the beam, i.e. the LGS sensors and ESG sensor show similar strain results. After the yielding of the rebars, the LGS sensors showed smaller strain results compared to the ESG sensors. It is concluded that the carrier of the LGS sensors lost shear bonding with its braided shield after the yielding of the steel rebars.

The beam experienced tensile failure (i.e. under-reinforced type failure). After unloading the beam, it is reloaded to observe the behavior of the LGS sensors in damaged structures, such as in the case of an earthquake. In the second loading the LGS sensors provided data whereas some of the ESG sensors failed.

While this work has provided the basis for the development of the LGS sensors, further studies ought to be carried. Some of these extensions of the work follow.

Higher initial resistance values can be used to measure strains that are below 400$\mu\epsilon$ by increasing the signal to noise ratio. One approach is to use a smaller diameter KA1 wire for this purpose, and the other approach is to use a wire that has higher resistivity value.

The effect of work-hardening of the wire on the gage factor should be further investigated to understand the strain behavior of a specimen that is already deformed. This data would be used to re-calibrate sensors embedded in structures that sustained damage.

Further tests should be conducted on the LGS sensors under compression loading. The design of such tests should ensure that no buckling occur.

Effect of time and temperature on the LGS sensors should be determined with experimental study.

Method of fabrication of the LGS sensor can be changed. The KA1 wire can be embedded into the center of the carrier, and this can be achieved by feeding the KA1 wire into a pultruding fiberglass composite during the manufacturing process.

Carrier characteristics can be further studied to improve the bonding between the carrier and the braiding. This can be achieved by using a carrier with rougher outer surface, or using a epoxy with higher shear strength.

The copper wires used to segment the strain sensing wire can be replaced by a wireless system that can monitor the strain on the sensor remotely.

References

1. Callister, W.D. Jr., "Materials Science and Engineering, an Introduction" Fifth Edition, John Wiley and Sons, Inc. Printed in the USA (1999), pp 112-134.
2. MacGregor, J.G., "Reinforced Concrete Mechanics and Design" Third Edition, Prentice Hall, Upper Saddle River, New Jersey (1997), pp 98-110.
3. Hassoun, M.N., "Structural Concrete Theory and Design" Second Edition. Prentice Hall, Upper Saddle River, NJ (2002), pp 42-56.
4. Meyer, C., "Design of Concrete Structures". Prentice Hall, Upper Saddle River, New Jersey (1996), pp 130-141.
5. Dr. N. John Gardner, Professor in the Civil Engineering Department of the University of Ottawa. Personal communication.
6. Kalamkarov, A.L., Georgiades, A.V., MacDonald, D.O., and Fitzgerald, S.B., "Pultruded fibre reinforced polymer reinforcements with embedded fibre optic sensors." Canadian Journal of Civil Engineering Volume 27 Issue 5 (2000), pp 972-984.
7. Fraden, J. "Handbook of Modern Sensors, Physics, Designs, and Applications" Second Edition. American Institute of Physics (AIP) Press, Woodburry, New York, (1997), pp 63, 242-244, 324-325, 356-364.
8. Dally, J.W., Riley, W.F., and McConnell, K.G. "Instrumentation for Engineering Measurements" Second Edition. John Wiley and Sons, Inc. New York (1993), pp 126-135, 170-171, 232-234.
9. Padmanabhan, T.R., "Industrial instrumentation Principles and Design" Springer-Verlag London Limited, Printed in Great Britain (2000), pp 388-392.
10. Ravisankar, K., Parivallal, S., Narayanan, T., Kesavan, K., and Narayanan, R. "Vibrating wire strain gauges for long-term monitoring of structures" The Indian Concrete Journal v.75 issue 8 (2001): 535-541.
11. Neil, S. A., Williams, M. S., and McFadden, P. D., "Measurement of Low-Amplitude Hysteresis Behaviour of Concrete by High-Precision Vibrating Wire Strain Gauges." Key Engineering Materials, Vols.245-246 (2003): 315-322

12. http://www.gage-technique.demon.co.uk. Accessed 19-September-2004.

13. http://encardio.com/prod_vwstraingage.html.

14. Tennyson, R.C., Coroy, T., Duck, G., Manuelpillai, G., Mulvihill, P., Cooper, D.J.F., Smith, P.W.E., Mufti, A.A., Jalali, S.J. "Fibre optic sensors in civil engineering structures." Canadian Journal of Civil Engineering Volume 27 Issue 5 (2000): 880-889.

15. Tjin, S.C., Wang, Y., Sun, X., Moyo, P., and Brownjohn, J.M.W., "Application of quasi-distributed fibre Bragg grating sensors in reinforced concrete structures." Measurement Science and Technology Volume 13 Issue 4 (2002): 583-589.

16. Schulz, W.L., Conte, J.P., and Eric, U. "Long Gage Fiber Optic Bragg Grating Strain Sensors to Monitor Civil Structures." Proceedings of SPIE - The International Society for Optical Engineering Volume 4330, 2001, Pages 56-65.

17. Lau, K., Chan, C., Zhou, L., Jin, W. "Strain monitoring in composite-strengthened concrete structures using optical fibre sensors." Composites Part B: Engineering Volume 32 Issue 1 (2001): 33-45.

18. Tennyson, R.C., Mufti, A.A., Rizkalla, S., Tadros, G., and Benmokrane, B. "Structural health monitoring of innovative bridges in Canada with fiber optic sensors ." Smart Materials and Structures Volume 10 Issue 3 (2001): 560-573.

19. Zhao, Y., and Ansari, F., "Embedded fiber optic sensor for characterization of interface strains in FRP composite." Sensors and Actuators A: Physical Volume 100 Issue 2-3 (2002): 247-251.

20. DeMerchant, M., Brown, A., Smith, J., Bao, X., and Bremner, T. "Distributed strain sensing for structural monitoring applications." Canadian Journal of Civil Engineering Volume 27 Issue 5 (2000): 873-879.

21. DeMerchant, M.D., Brown, A.W., Bao, X., and Bremner, T.W. "Brillouin scattering based strain sensing." Proceedings of SPIE - The International Society for Optical Engineering Volume 3670, 1999, Pages 352-358

22. Horiguchi, Tsuneo, Toshio Kurashima, and Mitsuhiro Tateda. "Tensile Strain Dependence of Brillouin Frequency Shift in Slica Optical Fibers." IEEE Photonics Technology Letters Volume 1 No.5 (1989): 107-108.

23. Zeng, X., Bao, X., Chhoa, C.Y., Bremner, T.W., Brown, A.W., DeMerchant, M.D., Ferrier, G., Kalamkarov, A.L., Georgiades, A.V., "Strain measurement in a concrete beam by use of the Brillouin-scattering-based distributed fiber sensor with single-mode fibers embedded in glass fiber reinforced polymer rods and bonded to steel reinforcing bars" Applied Optics, Volume 41, Issue 24 (2002), pages 5105-5114.

24. Kupke, M.,Schulte, K., and Schuler R. "Non-destructive testing of FRP by d.c. and a.c. electrical methods" Composites Science and Technology Volume 61, Issue 6 (2001), 837-847.

25. Bakis, C. E., Nanni, A., Terosky, J.A., and Koehler, S.W. "Self-monitoring, pseudo-ductile, hybrid FRP reinforcement rods for concrete applications" Composites Science and Technology Volume 61 Issue 6 (2001), 815-823.

26. Biter, W.J., Hess, S.M., Oh, S., Geshury, A., Heider, D. "Magnetic Wire for Monitoring Strain in Composites" Sensors (Peterborough, NH) Volume 18, Issue 6, June 2001, pp 110-114

27. Avallone, E.A.(Editor), Baumeister III, T. (Editor) "Marks' Standard Handbook for Mechanical Engineers" Tenth Edition. McGraw-Hill, USA (1996), pp 15-2, 15-25.

28. Jackson, H.W., "Introduction to Electric Circuits" Sixth Edition. Prentice Hall, Englewood Cliffs, New Jersey (1986), pp 68-75.

29. Kosow, I.L., "Circuit Analysis" John Wiley and Sons Inc., Printed in the USA (1988), pp 25-31.

30. Radin, S.H., and Folk, R.T. "Physics for Scientists and Engineers" Prentice-Hall, Inc., Englewood Cliffs, New Jersey (1982). pp 513-521.

31. http://www.vishay.com/brands/measurements_group/guide/ta/sgms/sgt20.htm. Accessed 21-11-2004, pp 59-89.

32. Cogdell, J.R., "Foundations of Electronics", Prentice Hall Inc., Upper Saddle River, New Jersey (1999) pp 280-284.

33. MATWEB: http://www.matweb.com/search/SpecificMaterial.asp?bassnum=NCALZ37

Appendix-I

Derivation of the equations presented in Chapter 3:

$$R = \rho \times \frac{L}{A} \quad \text{.....(3.1)}$$

where ρ, L, and A are the resistivity, length, and cross sectional area, respectively.

Differentiating Equation 3.1 gives:

$$dR = \frac{\rho}{A} dL - \rho \frac{L}{A^2} dA + \frac{L}{A} d\rho$$

dividing the result by R gives Equation 3.3:

$$\frac{dR}{R} = \left[\frac{dL}{L} + \frac{d\rho}{\rho} - \frac{dA}{A} \right] \quad \text{.....(3.3)}$$

when $A=(\pi)r^2$, and $dA=2(\pi)(r)dr$ is substituted into Equation 3.3:

$$\frac{dR}{R} = \left[\frac{dL}{L} - 2\frac{dr}{r} \right] + \frac{d\rho}{\rho}$$

it is known that radial strain and axial strain is related by the formula:

$$\varepsilon_r = \frac{dr}{r} = -\nu\frac{dL}{L} = -\nu\varepsilon_L$$

when this relationship is substituted into the previous equation, the following is found:

$$\frac{dR}{R} = \left(\varepsilon_L - \varepsilon_r\right) + \frac{d\rho}{\rho}$$

and this last equation can be simplified to:

$$\frac{dR}{R} = \frac{d\rho}{\rho} + \left[\varepsilon_L(1+2\nu)\right]$$

which would form Equation 3.4:

$$\frac{dR}{R} = \frac{d\rho}{\rho} + \frac{dL}{L}(1+2\nu) \quad \text{.....(3.4)}$$

The equation 3.4 is divided by axial strain to get the gage factor, G;

$$G = \frac{\frac{dR}{R}}{\varepsilon} = \frac{d\rho/\rho}{\varepsilon} + (1+2\nu) \quad \text{.....(3.5)}$$

Poisson's ratio in Equation 3.5 cancels with the following resistivity formula,

$$\rho = \frac{2 \times m \times v_0}{n \times e^2 \times \lambda}$$

This formula can be simplified to Equation 3.2 if n is replaced by the total number of conduction electrons, N_0, in a conductor which has a length L and a cross sectional area A:

$$\rho = \frac{2 \times m \times v_0 \times A \times L}{N_0 \times e^2 \times \lambda} \quad \text{.....(3.2)}$$

In Equation 3.2, electron mass (m) and charge (e) are assumed constant, and electrical currents are conducted through metals by means of free electrons.

Taking the derivative of Equation 3.2 gives:

$$\frac{d\rho}{\rho} = \frac{dv_0}{v_0} - \frac{d\lambda}{\lambda} - \frac{dN_0}{N_0} + \left[\frac{dL}{L} + \frac{dA}{A}\right]$$

When this equation is substituted into equation 3.3, following is found:

$$\frac{dR}{R} = 2\frac{dL}{L} + \frac{dv_0}{v_0} - \frac{d\lambda}{\lambda} - \frac{dN_0}{N_0}$$

Substituting dR/R into Equation 3.5 gives Equation 3.7;

$$G = \frac{dR/R}{dL/L} = \frac{\frac{dR}{R}}{\varepsilon_L} = 2 + \frac{\frac{d\nu_0}{\nu_0} - \frac{d\lambda}{\lambda} - \frac{dN_0}{N_0}}{\varepsilon_L} \quad \text{.....(3.7)}$$

Derivation of Equation 3.6:

With reference to Figure 3.3,

The voltage output of the bridge can be found by treating the top and the bottom parts of the bridge as individual voltage dividers.

$$Vs = (R1 + R2) \times i$$

$$V_{AB} = R1 \times i$$

$$Vs = (R1 + R2)\frac{V_{AB}}{R1}$$

$$\therefore V_{AB} = \frac{R1}{R1 + R2} \times Vs$$

$$V_{AD} = \frac{R4}{R3 + R4} \times Vs$$

$$Vo = V_{BD} = V_{AB} - V_{AD}$$

$$\therefore Vo = \frac{R1R3 - R2R4}{(R1 + R2)(R3 + R4)} \times Vs$$

this last form is Equation 3.6.

In the case of the bridge designed for this study, all three stable arms of the bridge are constant (R2=R3=R4=R). Only the resistance of the wire is changing (R_{wire}). If this information is substituted to Equation 3.6:

$$Vo = \frac{(R_{wire} \times R) - R^2}{(R_{wire} + R)(2R)} Vs = \frac{R_{wire} - R}{R_{wire} + R} \times \frac{Vs}{2}$$

$$2\frac{Vo}{Vs} = \frac{R_{wire} - R}{R_{wire} + R}$$

$$R_{wire}\frac{2Vo}{Vs} + R\frac{2Vo}{Vs} = R_{wire} - R$$

$$R\frac{2Vo}{Vs} + R = R_{wire} - R_{wire}\frac{2Vo}{Vs}$$

$$\frac{2Vo}{Vs}R + R = R_{wire}\left[1 - \frac{2Vo}{Vs}\right]$$

$$R_{wire} = \frac{[(2Vo/Vs) \times R] + R}{1 - (2Vo/Vs)}$$

this last form is Equation 3.8.

Appendix-II

These calculations are done to show the effect of elastic modulus of the carrier on the strain measurements. Consider an embedded KA1 wire pulling on the carrier (Figure 1). This action create shear force on the carrier (Figure 2).

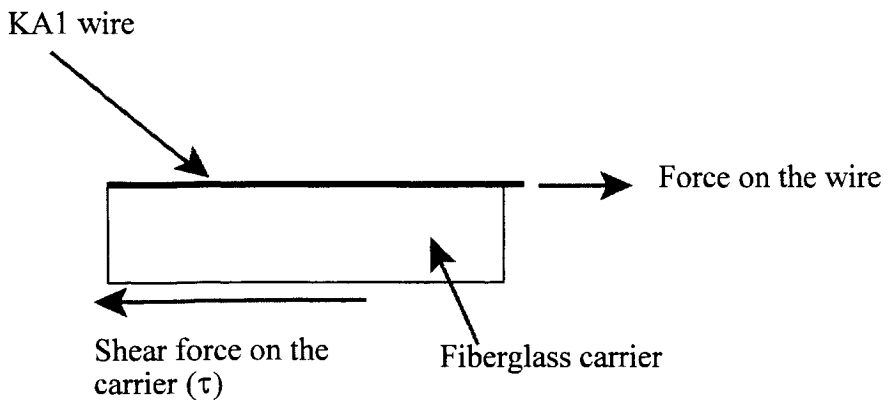

Figure 1: Schematic representation of the acting forces.

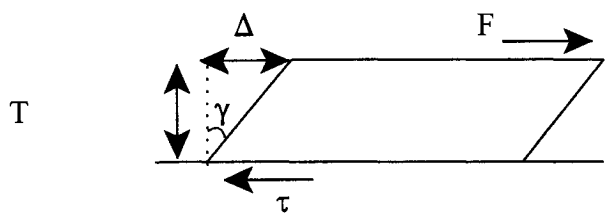

Figure 2: Schematic representation of the shear deformation.

$$\tau = G \times \gamma = G\frac{\Delta}{t} = \frac{E}{2 \times (1+\nu)}\frac{\Delta}{t}$$

The tensile force that is applied to the carrier is balanced by the shear force.

$$TensileForce = ShearForce$$

$$F_{wire} = \tau \times ShearArea$$

$$F_{wire} = \frac{E}{2 \times (1+\nu)} \times \frac{\Delta}{t} \times ShearArea$$

$$\Delta = \frac{F_{wire} \times 2 \times (1+\nu) \times t}{E \times ShearArea}$$

If numbers of common glass rod (38GPa elastic modulus, Poisson's Ratio of 2) and nylon rod (3GPa elastic modulus, Poisson's Ratio of 4) are substituted into the formula for Δ; (rod diameter is taken as 0.0127m, gage length is taken as 30 cm, and the force on the wire is found to be 14 N for yield point of a 0.18 mm diameter KA1 wire)

$\Delta_{nylon} = 4.98 \times 10^{-8}$ m (corresponds to a strain of 0.16 $\mu\epsilon$ for 30 cm gage length)

$\Delta_{glass} = 2.34 \times 10^{-9}$ m (corresponds to a strain of 0.008 $\mu\epsilon$ for 30 cm gage length)

As a result of this calculation, it is found that higher elastic modulus gives less shear deformation in the carrier.